

University of Nevada, Reno

**DIRECTIONAL SOLIDIFICATION OF PB-SB  
ALLOY ASSISTED BY PRESSURE PULSES**

A THESIS SUBMITTED IN PARTIAL FULFILLMENT OF THE  
REQUIREMENTS FOR THE DEGREE OF MASTER OF SCIENCE

IN

MATERIALS SCIENCE AND ENGINEERING

BY

JOAO PAULO PINTO BRAZ

Dr. JEFFREY C. LACOMBE / Thesis Advisor

DECEMBER 2010



University of Nevada, Reno  
Statewide • Worldwide

THE GRADUATE SCHOOL

We recommend that the thesis  
prepared under our supervision by

**JOAO PAULO PINTO BRAZ**

entitled

**Directional Solidification of Pb-Sb Alloy Assisted by Pressure Pulses**

be accepted in partial fulfillment of the  
requirements for the degree of

**MASTER OF SCIENCE**

Jeffrey C. LaCombe, Ph.D., Advisor

Dhanesh Chandra, Ph.D., Committee Member

Eric Wang, Ph.D., Graduate School Representative

Marsha H. Read, Ph. D., Associate Dean, Graduate School

December, 2010

## ABSTRACT

Directional solidification processes assisted with pressure pulses were performed with the goal of producing a novel process capable of introducing changes in dendritic microstructure morphologies. The alloy used in these experiments was a Pb-7wt% Sb, with a liquidus temperature of approximately 280°C. Various melt pressure profiles were investigated with maximum pressures of -266.3 to -1452.8psi and oscillation frequencies ranging from 0 (constant force) to 7.4Hz. It was found that application of pressure decreased the secondary dendrite arms spacing ( $\lambda_2$ ) when compared with the no pressure experiments and cyclic pressure oscillations cause a resonance effect in the  $\lambda_2$  values when the pressure pulse frequency matches the arms' natural frequency of formation. It is not yet clear if this resonance behavior is strong enough or reliable enough to be of potential interest for industrial applications seeking to employ novel approaches to controlling microstructural length scales during directional or equiaxed dendritic solidification processes.

## ACKNOWLEDGMENTS

First of all, I would like to acknowledge my family, which has been giving me all the support necessary to all the achievements I have made this far. In special, I would like to acknowledge my mother Nilce Saraiva Pinto and my father Paulo Roberto de Carvalho Braz, human-beings that serve as models for my daily attitudes.

I also would like to acknowledge my advisor Dr. Jeffrey C. LaCombe for all the support and knowledge transmitted.

Thanks to Dr. Dhanesh Chandra and Dr. Eric Wang for being part of my thesis' defense committee and to Dr. Olivia Graeve, the person that basically "started" this whole process.

And finally, but not least, all my friends that contributed to this accomplishment.

## TABLE OF CONTENTS

1) INTRODUCTION.....	01
2) BACKGROUND.....	03
2.1) Solidification.....	03
2.2) Dendrites.....	04
2.3) Casting.....	15
2.4) Material Properties vs. Dendritic Arm Spacing (DAS).....	17
2.5) Clapeyron Effect.....	23
2.6) Goals of this Study.....	27
3) MATERIALS AND METHODS.....	28
3.1) Sample Preparation.....	29
3.2) Mold.....	31
3.2.1) Ceramic Heater.....	35
3.3) Cooling System.....	38
3.4) Data Acquisition system.....	40
3.5) Temperature Controllers.....	42
3.6) Inside Mold Temperature Calibration Measurements.....	44
3.7) Calculation of the Liquidus velocity for each Position.....	46
3.8) Pressurization Using the MTS Machine.....	46
3.9) Pressure Applied Experiments.....	48
3.10) Metallographic Steps.....	50
3.10.1) Sectioning.....	50

3.10.2) Mounting.....	52
3.10.3) Grinding and Polishing.....	53
3.10.4) Etching.....	56
3.11) Microscope Analysis.....	57
3.12) Secondary Arm Spacing Measurements.....	57
4) RESULTS AND DISCUSSION.....	61
4.1) Local Solidification Time.....	61
4.2) Liquidus Velocity (Solid-Liquid Interface Velocity).....	64
4.3) Secondary Dendritic Arm Spacing – SDAS ( $\lambda_2$ ).....	66
4.4) Pressure Applied Solidification Experiments.....	75
4.5) Secondary Dendrite Arm Spacing ( $\lambda_2$ ) Analysis.....	80
5) CONCLUSIONS.....	102
6) FUTURE WORK.....	103
7) REFERENCES.....	106
8) APPENDIX.....	109

## LIST OF TABLES

Table 1 – Cast LM25 alloy properties <sup>[7]</sup> .....	18
Table 2 – $\Delta H$ and $\Delta V$ tabulated and calculated values for Pb and Sb pure elements and alloy.....	26
Table 3 – Changes in the melting temperature caused by application of pressure.....	26
Table 4 – Force and Frequency values used for the pressure-assisted solidification processes.....	50
Table 5 - Grinding process parameters .....	55
Table 6 – Polishing process parameters.....	55
Table 7 – Solidification time (time to cool to liquidus temperature) for each inside mold position example setup.....	62
Table 8 – Measured values of $\lambda_2$ (mean) and their standard deviation ( $\sigma$ ) for samples 01 and 02 (no pressure) for all positions.....	68
Table 9 – $\lambda_2$ formation frequency values at different positions obtained for samples 01 and 02.....	75

## LIST OF FIGURES

Figure 1 – Micrograph of directional solidified dendrites. $\lambda_1$ refers to the distance between the primary arms and $\lambda_2$ is the distance between the secondary arms – primary arms branches. <sup>[17]</sup> .....	05
Figure 2 – Pb-Sb phase diagram <sup>[18]</sup> .....	06
Figure 3 – Pb-Sb simplified phase diagram <sup>[19]</sup> .....	07
Figure 4 – Composition as a function of position for a hypoeutectic alloy where I is the solid-liquid interface <sup>[19]</sup> .....	08
Figure 5 – Concentration profile showing the change due to the solute rejection <sup>[19]</sup> .....	09
Figure 6 – Scheme showing the liquidus temperature as a function of position <sup>[5]</sup> .....	10
Figure 7 – Perturbation originated from the constitutional supercooling <sup>[19]</sup> .....	12
Figure 8 – Scheme showing several perturbations <sup>[19]</sup> .....	12
Figure 9 – Scheme showing the solute concentration around the tip of a perturbation <sup>[5]</sup> .....	14
Figure 10 - Bronze age stone mold <sup>[20]</sup> .....	16
Figure 11 – Bronze Age sword replicate made using a bivalve mold done by Dr. Peter Northover, Oxford <sup>[20]</sup> .....	16
Figure 12 – a) Graph showing how the UTS varies as a function of the DAS; b) Graph showing the variation of the elongation as the DAS values decrease <sup>[7]</sup> ...	18

Figure 13 – UTS variation as the secondary DAS values increase for both Aluminum alloys containing 5 and 9wt% of Si <sup>[8]</sup> .....	19
Figure 14 – Changes in the Ultimate tensile and Yield Strength as the secondary DAS values increase for a Zinc alloy containing 27wt% of Aluminum <sup>[9]</sup> .....	19
Figure 15 – Dendritic cell size as a function of Pressure applied during the solidification process <sup>[10]</sup> .....	20
Figure 16 – Solidification time curves for casting of Al-5.4wt%Cu under no pressure (gravity) and pressures of 0.5, 1.0 and 1.7 GPa <sup>[10]</sup> .....	21
Figure 17 – Solidification time curves for AM50A samples cast under pressures of 30, 60 and 90MPa <sup>[11]</sup> .....	21
Figure 18 – Dendrite shape when an external flow is present. U in this case is the flow velocity which was equal to 15 $\mu$ m/s <sup>[12]</sup> .....	23
Figure 19 – Different Liquidus temperature for an AM50A alloy for different applied pressure during the solidification process <sup>[11]</sup> .....	25
Figure 20 – a) Lead and; b) Antimony materials used to compose the sample. c) Balance used in the process and; d) crucible where the material was placed into.....	30
Figure 21 – NEYTECH Qex vacuum furnace.....	31
Figure 22 – Ladle inside the Barnstead Thermolyne 48000 furnace prepared to be heated.....	31
Figure 23 – a) Mold apparatus completely assembled; b) Picture of the die part showing the utilized O-ring and its groove; c) Bottom part of the mold together	

with the chill plate and; d) Picture showing the water pipes pointing straight to the chill plate and the O-ring placed on the water reservoir.....	32
Figure 24 – Mold Schematic created using SolidWorks 2007®; a) solid piston; b) small piston with holes; c) top part of the mold; d) chill plate and; e) bottom reservoir.....	33
Figure 25 – Pipe and hose connections responsible for the water flow.....	34
Figure 26 – Anti-seize lubricant used to ease the sample removal from the mold.....	34
Figure 27 – Ceramic heater showing the heater coils end.....	36
Figure 28 – a) Schematic of the inside part of the mold; b) and c) polymeric mold and plug for casting the ceramic heater cartridge.....	36
Figure 29 – a) Inside part of the (split in two) ceramic heater showing the metal coil grooves and; b) NIC60 coils used on this task.....	37
Figure 30 – a) Die-Casting mold together with the ceramic heater and; b) Interior of the heater cartridge, showing the mica sheet used as an electrical insulator..	38
Figure 31 – Scheme of the water flow apparatus.....	39
Figure 32 – Temperature controlled cooling system; a) Fluid circulator used to keep the water at the desired temperature and; b) some of the open and close valves utilized to redirect the water flow as necessary.....	40
Figure 33 – a) Controllers and data acquisition board used in the experiment and; b) Controllers magnified view.....	41

Figure 34 – a) Image of the interface of the program that controls the heaters and; b) Image of the interface of the program that does the thermocouples readings data acquisition.....	42
Figure 35 – a) Image of the VARIACs and; b) Alligator clips connected to the heater coils.....	43
Figure 36 – Fan used as an exhaustion system for the lubricant fumes.....	44
Figure 37 – Perforated stainless steel small piston.....	45
Figure 38 – Thermocouple bundle (six) used to measure the inside mold temperature profile.....	46
Figure 39 – a) MTS machine and b) MTS Flex Test SE controller used together with the monitor screens showing the computer interface.....	47
Figure 40 – a) Piston holder and; b) Piston with silicone O-rings.....	48
Figure 41 – Graph showing the force variation as a function of the time (controller screen).....	48
Figure 42 – MTS machine applying pressure on the molten metal during a performance test.....	49
Figure 43 – a) Cutting machine used to section the samples and; b) Cutting fluid.....	51
Figure 44 – Scheme of each section dimension within the sample. Notice that the 3 <sup>rd</sup> piece is actually 10mm long.....	52
Figure 45 – Sample ready to be mounted.....	52

Figure 46 – a) Epoxy and Hardener used to produce the mounting mixture; b) Samples inside the mounting cups ready to be filled with the epoxy and; c) Mold releaser used to facilitate the sample removal from the cups.....	53
Figure 47 – a) Grinding and polishing machine apparatus and; b) Several grits used on the grinding process.....	54
Figure 48 – Acetic Acid and Hydrogen Peroxide used for etching.....	56
Figure 49 – Calibration Standard and the samples marked on the middle.....	57
Figure 50 – DAS measurements lines draw using the Scentis software showing the marked arms.....	59
Figure 51 – Graph showing the solidification time (time for the temperature to cool to the liquidus temperature) for the 10mm position.....	61
Figure 52 – Graph of the solid-liquid interface position as a function of time. The time values were shifted to the origin.....	63
Figure 53 – Graph of the position as a function of the square root of time. The expected linear form was observed.....	64
Figure 54 – Micrographs taken from sample 01 a) 05mm position at 40x magnification; b) 10mm position at 40x magnification; c) 15mm position at 20x magnification; d) 20mm position at 20x magnification; e) 25mm position at 20x magnification and; 30mm position at 20x magnification.....	67
Figure 55 – $\lambda_2$ as a function of position showing a small difference between the samples values.....	70
Figure 56 – Standard deviation ( $\sigma$ ) as a function of position. The values also agree with each other.....	71

Figure 57 – $\lambda_2$ as a function of the Liquidus velocity. As $V_L$ values increase, $\lambda_2$ values decrease.....	72
Figure 58 – $\lambda_2$ values as a function of $V_L$ for Pb-Sb alloys with varying concentrations. Notice how $\lambda_2$ decreases as $V_L$ increases for all curves despite the amount of Sb. <sup>[16]</sup> .....	73
Figure 59 – Frequency of formation of $\lambda_2$ as a function of position. Note how the natural formation frequency decreases as the position increases.....	74
Figure 60 – Graph showing the applied force as a function of time for the whole experiment duration of the -110lbf maximum load.....	76
Figure 61 – Graph showing a section of the graph on Figure 59 correspondent to one second.....	77
Figure 62 – Graph showing the applied force as a function of time for the whole experiment duration of the -310lbf maximum load.....	78
Figure 63 – Graph showing a section of the graph on Figure 62 correspondent to one second.....	79
Figure 64 – Graph showing how the displacement varied as a function of the position.....	80
Figure 65 – Graph showing the variation of the secondary DAS as a function of position for the samples without pressure and 110 and 310lbs at 7.4Hz. $\lambda_2$ values are smaller for the samples solidified under pressure influence.....	82
Figure 66 – Graph showing the variation of the $\sigma$ values as a function of position for the samples without pressure and -110 and -310lbs at 7.4Hz. These values also decreased for the samples where pressure was applied.....	83

- Figure 67 - Graph showing the variation of  $\lambda_2$  as a function of position for the samples without pressure; -310lbf at 5.9Hz and -310lbf at 7.4Hz.....84
- Figure 68 - Graph showing the variation of  $\sigma$  as a function of position for the samples without pressure; -310lbf at 5.9Hz and -310lbf at 7.4Hz. One more time the  $\sigma$  values decreased for the pressure applied samples.....85
- Figure 69 - Graph showing the variation of  $\lambda_2$  as a function of position for the samples without pressure; -310lbf at 5.9Hz; -310lbf at 7.4Hz and -310lbf at constant pressure.....86
- Figure 70 - Graph showing the variation of  $\sigma$  as a function of position for the samples without pressure; -310lbf at 5.9Hz; -310lbf at 7.4Hz and -310lbf at constant pressure.....88
- Figure 71 – Graph showing how the liquidus position varied as a function of time for positions between 0 and 60mm. An inflection point occurs at around 140s after the alloy started solidifying.....92
- Figure 72 - Graph showing the applied force as a function of time for the whole experiment duration of the -600lbf maximum load at a 6.0Hz frequency.....93
- Figure 73 - Graph showing how the displacement varied as a function of time for the -600lbf at 6.0Hz experiment.....94
- Figure 74 - Graph showing the variation of  $\lambda_2$  as a function of position for the samples without pressure; -600lbf at 6.0Hz and -600lbf at constant pressure. Notice the *dip* around the 17.5mm position for the cyclic pressure curve.....95
- Figure 75 - Graph showing the variation of  $\sigma$  as a function of position for the samples without pressure; -600lbf at 6.0Hz and -600lbf at constant pressure. The

same <i>dip</i> around the 17.5mm position appears again for the cyclic pressure curve.....	96
Figure 76 - Graph showing the variation of $\lambda_2$ as a function of $V_L$ for the samples without pressure; -600lbf at 6.0Hz and -600lbf at constant pressure. The values for $V_L$ were extrapolated for the positions 10, 12.5, 16.25, 17.5, 18.75, 20 and 30mm position, since there was no time data for those positions (notice that no horizontal error bars are plotted for these).....	97
Figure 77 – Graph of $\lambda_2$ as a function of position showing the expected changes on the values when cyclic pressure is applied during the solidification process. The red curve represents the expected values.....	99
Figure 78 - Graph of standard deviation values ( $\sigma$ ) as a function of position showing the expected changes on the values when cyclic pressure is applied during the solidification process. The red curve represents the expected values.....	101

## 1) INTRODUCTION

Materials' mechanical properties have always been of great interest to the research and engineering communities, since materials started to be categorized and applied on our daily living activities. Nowadays, engineers are trying to find new materials that meet a variety of needs-often with novel properties and cost-effective manufacturing techniques. The present study represents one approach to addressing the issue of higher strength-to-weight ratio materials.

It is now well-known that many mechanical properties of metals and alloys are directly correlated with their microstructure. Most of these metals and alloys were (at one point in their processing history) solidified from a liquid state, with a dendritic solidification process, where the forming crystals are tree-like in form (dendrites). The details of the shapes and sizes of the dendritic crystals play a significant role in the properties of the alloy produced.

The goal of this study is to closely observe how dendritic crystals are formed and what parameters influence its formation, as well as to develop a novel technique that is capable of altering the spaces between the dendrite arms, which ultimately can increase the materials strength (and other properties). To do this, pressure assisted directional die-casting solidification experiments were carried out where different frequencies - ranging from values of 0 (constant pressure) to 7.4Hz, as well as different loads – ranging from -110 to -310lbf - were used to perform the tests. A Pb-7%wt Sb alloy was used in this project,

which has a liquidus temperature of 280°C. The directional solidification behavior was achieved having cooling water flow through a reservoir underneath the mold. The application of pressure during the directional solidification was observed to change the dendrite microstructure when compared with microstructures produced without pressure. The following sections of this document will describe each aspect of this project in full detail.

## 2) BACKGROUND

### 2.1) Solidification

The solidification process consists in changing a material's state from liquid to solid by rearranging the atoms of the liquid, which are in a certain degree of disorder, to a more ordered and well-oriented structure consisting of unit cells that are oriented according to some process factors (example: alignment of crystal structure along the temperature gradient)<sup>[1]</sup>. In terms of thermodynamics, the material's ability to change from one phase to another depends on the Gibbs free energy of the two states, (or, the chemical potential)<sup>[2]</sup>. This free energy depends most notably (for solidification) on temperature and enthalpy<sup>[2]</sup>. The favored equilibrium phase will be the one that, at a certain instant, has the lowest Gibbs free energy. It is noted that a liquid can still exist, even when the solid state's free energy is lower than the one for the liquid state. This is a meta-stable state and is referred to as supercooling<sup>[3]</sup>. In practice, liquids need to be supercooled in order to begin solidifying. The amount of supercooling needed to nucleate (begin) a solidification process depends on various factors, such as the critical nucleus radius and the surface energy<sup>[3]</sup>. The supercooling is (in a sense) an activation barrier for the solidification process. It is the supercooling that provides enough energy for the atoms to rearrange themselves into the material's solid microstructure. After the nucleation, as heat continues to be extracted from the liquid phase, more atoms adhere to the formed nucleus and make it grow. This is the crystal growth process. There is a variety of types of

crystal growth processes ranging from having a single crystal aligned along one specific direction, to having innumerable crystals with random crystallographic orientations<sup>[4]</sup>. In this work, we will be focused on an intermediate situation, where there are numerous crystals, but the ones that are aligned with the temperature gradient will preferentially grow and dominate the microstructure. This is known as the directional solidification type of dendritic solidification.

## **2.2) Dendrites**

Dendrite crystals are formed by structures that commonly occur during solidification of most metals and alloys<sup>[3]</sup>. It is a meta-stable growth process. Dendrites (derived from the Greek dendron, meaning “treelike”) have a shape which roughly looks like a tree (Figure 1). A portion of the dendritic structure still remains within the microstructure even after later materials processing (such as grain growth and heat treatment)<sup>[3]</sup>. As a result, dendritic microstructures affect many material properties through mechanisms such as the Hall-Petch grain-size strengthening mechanism<sup>[4]</sup>. This is why an improved understanding of how dendrites are formed, together with developing new mechanisms for controlling their morphology are so important for the materials community. As a result, there is a long history of such research<sup>[5-16]</sup>.

The details of dendritic solidification, more specifically, the physical and chemical phenomena responsible for the creation and growth of the secondary arms –  $\lambda_2$  (Figure 1) are beyond the scope of this thesis and will be left for the reader to research on his/her own. But how and when dendrites will be formed

during a solidification process will depend on the local liquid temperature, the local liquidus temperature and the energy balance between the free energy and the surface tension (energy), among others. A brief discussion regarding to some of these parameters during a crystal growth process will be addressed next.

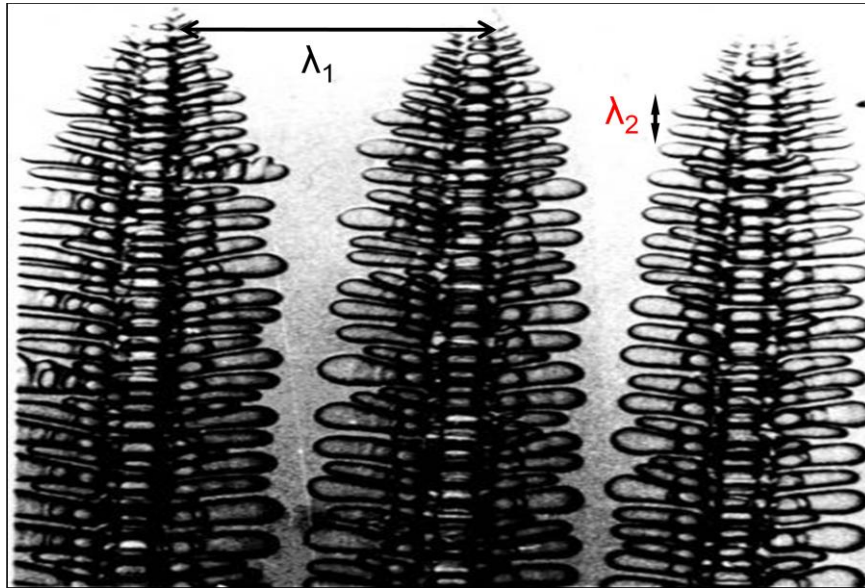


Figure 1 – Micrograph of directional solidified dendrites.  $\lambda_1$  refers to the distance between the primary arms and  $\lambda_2$  is the distance between the secondary arms – primary arms branches.<sup>[17]</sup>

One of the seminal works in the field of dendritic solidification was performed by Rutter and Chalmers<sup>[5]</sup> in which the authors used experiments to develop a model for alloy dendrite formation that is still used today – known as constitutional supercooling. This theory will now be discussed, mixed with some of this work's parameters to give a general understanding of how and why dendrites are formed.

The Pb-Sb (lead and antimony) system (phase diagram in Figure 2) will be the alloy used in this project. It represents a “typical” binary eutectic system, forms dendrites, and solidifies at a relatively low temperature (to simplify experiments).

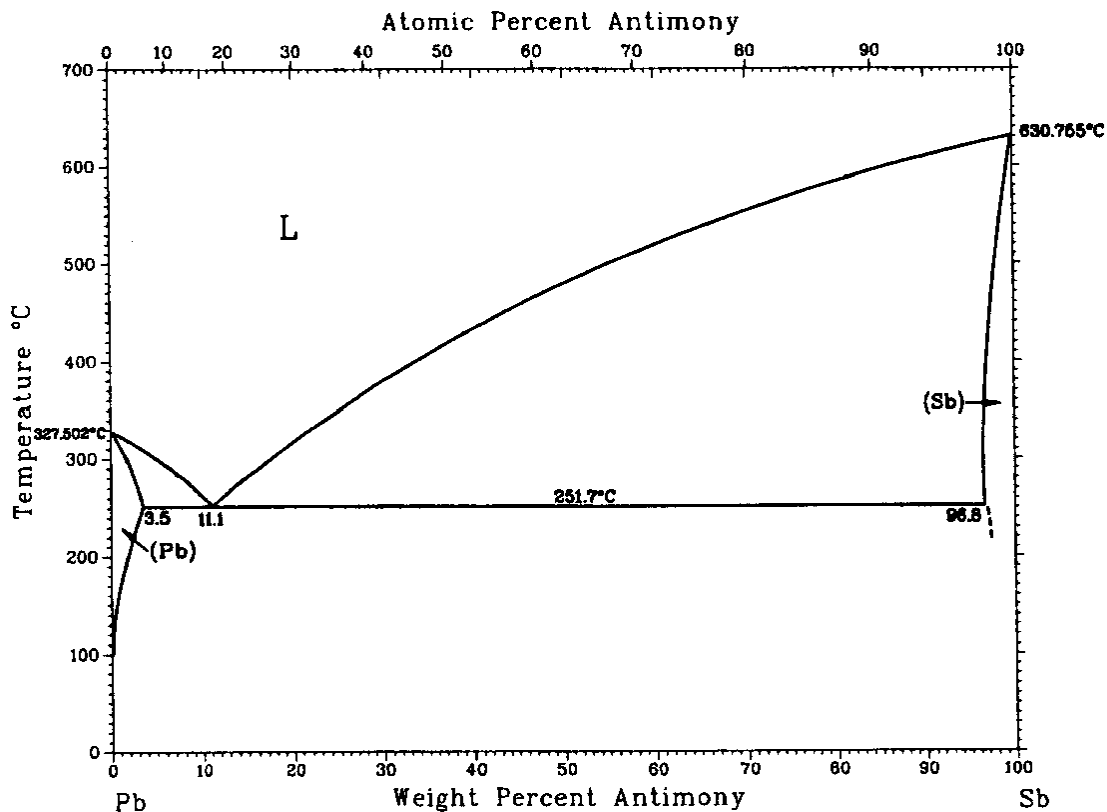


Figure 2 – Pb-Sb phase diagram <sup>[18]</sup>.

Examination of the Pb-Sn phase diagram shows that for an alloy with a composition of 7 weight percent antimony (the alloy used in this work), the liquidus temperature is around 280°C. This means that on cooling, the molten liquid *should* start solidifying at that temperature. But as discussed above, an

amount of supercooling is needed for the first nucleus to form. Once the very first nuclei are formed, the solid-liquid interface temperature is then controlled by the equilibrium liquidus temperature represented in the phase diagram, which in this case, would be close to 280°C. Now, we have a solid growing into a molten liquid. As can be seen in a simplified version of the phase diagram (Figure 3), the concentration of Sb in the just-formed solid will be different (lower, in this case) than the Sb concentration in the liquid, as determined by the equilibrium tie-line (horizontal line that crosses the two-phase region at a certain temperature). Thus, a graph of the concentration of antimony as a function of the location within the sample *should* look like the one in Figure 4 (assuming extremely low solidification rate and a perfect mixed liquid environment).

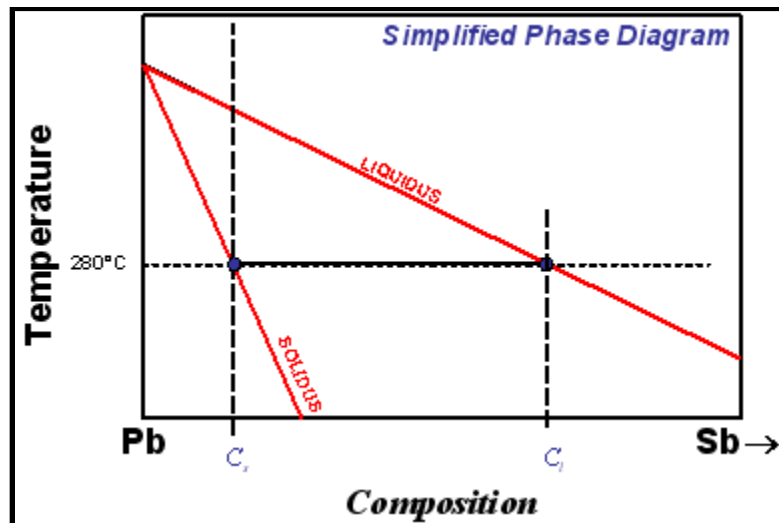


Figure 3 – Pb-Sb simplified phase diagram <sup>[19]</sup>.

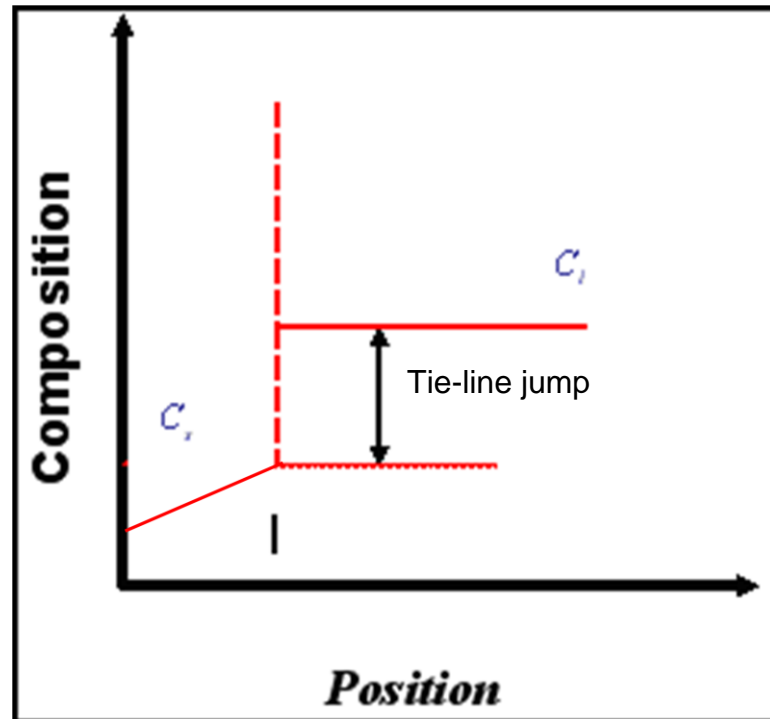


Figure 4 – Composition as a function of position for a hypoeutectic alloy where I is the solid-liquid interface <sup>[19]</sup>.

As the solidification proceeds, more liquid changes into solid, lowering the Sb concentration at a given location in the system as solidification occurs. This is dictated by the tie line jump in the equilibrium phase diagram. Thus, the excessive antimony will be rejected into the liquid immediately in front of the solid-liquid interface. As a result, the concentration profile would look more like the one on Figure 5.

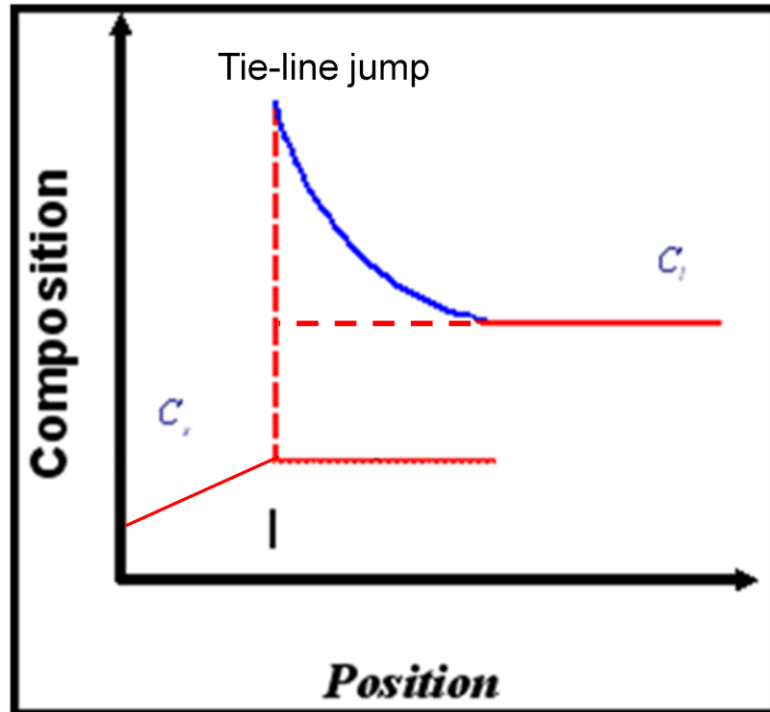


Figure 5 – Concentration profile showing the change due to the solute rejection<sup>[19]</sup>.

It can be seen from the graph that the position right in front of the solid-liquid interface has a higher concentration than the molten metal farther from that interface. From here, we can have a variety of situations, but we shall pay attention to two: the first is where the solidification front is advancing so slowly that the higher solute concentration in the liquid has enough time to diffuse into the bulk liquid, resulting in the concentration profile looking more like the one already shown on Figure 4 (i.e., concentration gradients in the liquid have enough time to diffuse or mix out). In this situation, the growth process is carried out under a relatively stable state and no dendrites are formed. Instead, a smooth planar surface is achieved and the equilibrium phase diagram is essentially followed. The second case occurs when the solidification front is

moving faster than diffusion in the liquid can occur. I.e., it is unable to “accommodate” the rejected solute from the solidification process. Let’s take a closer look on what happens in this situation.

Going back to the phase diagram, it can be realized that the liquidus temperature decreases as the amount of solute increases. So, the temperature that the liquid will solidify at will now be lower than the temperature that the system is at. Thus, the solid-liquid interface needs to decrease its temperature until reaching the corresponding liquidus temperature (reminding that thermal diffusion, in this case, is typically much faster than mass diffusion). If we now plot a graph of the liquidus temperature as a function of the solute concentration (which will be a function of position) a graph like the one in Figure 6 is obtained.

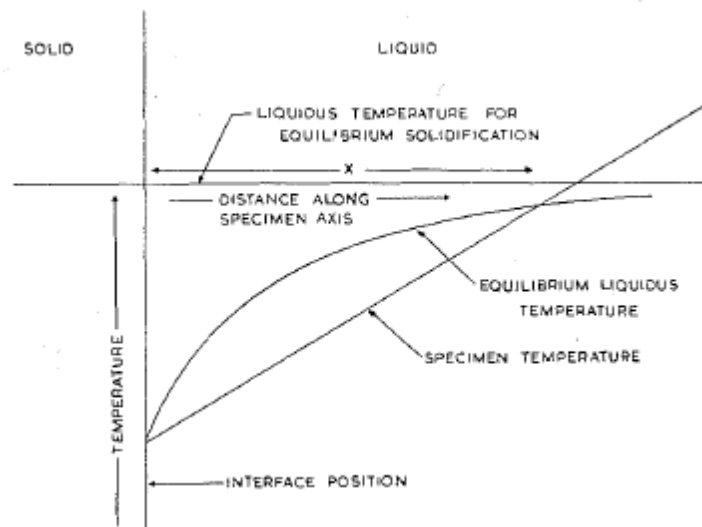


Figure 6 – Scheme showing the liquidus temperature as a function of position<sup>[5]</sup>.

The specimen temperature is the temperature gradient inside the liquid and the equilibrium liquidus temperature is the temperature at which the liquid would start to become solid. As we can see from this particular figure, there is a certain distance, within the liquid, where its temperature is below the liquidus temperature. In other words, that liquid portion is in a meta-stable state, i.e., it is supercooled. This particular type of supercooling, caused by composition changes within the solidification process, is referred to as “constitutional supercooling”<sup>[5]</sup>. I.e., the supercooling resulted not from a change in the temperature, but rather from a change in the local composition (and therefore, the local melting temperature).

In the presence of a supercooled melt ahead of the solid, it is conceivable, then, that any localized perturbation on the solidification interface (Figure 7) may extend out into a region of liquid that is supercooled and therefore cause the perturbation to grow and destabilize the otherwise smooth solid-liquid interface. Conversely, if the perturbation extends into a warm (superheated) region, it will then melt back, stabilizing the interface. Which occurs was found to depend on several process parameters and material properties including the solidification rate (dictated by the temperature gradient), solid-liquid surface tension, amount of supercooling and the solid heat-transfer coefficient.

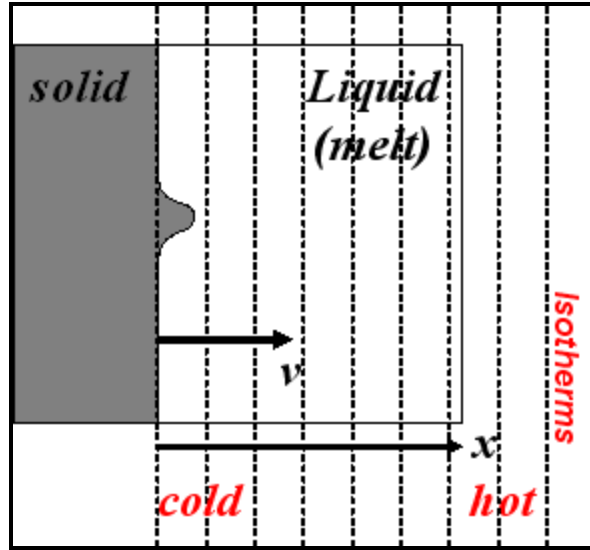


Figure 7 – Perturbation originated from the constitutional supercooling <sup>[19]</sup>.

Note that the same conditions described above apply to the whole solid-liquid interface, so, instead of just one perturbation, many other ones will be emerging into the liquid (Figure 8), and get “tested” by the local melting temperature (as dictated by the local composition).

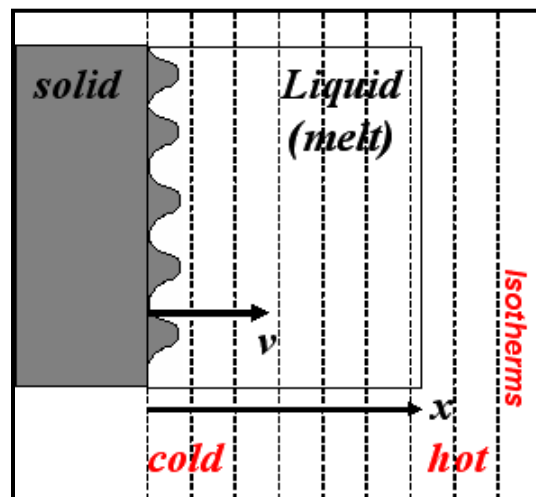


Figure 8 – Scheme showing several perturbations <sup>[19]</sup>.

Now, the processes occurring at the very tip of the perturbation will be analyzed. The same solute rejection principle applies in this case, but, different from what happened at the surface, the rejected solute can now diffuse to the sides (not merely ahead into the liquid), which are at a lower concentration (Figure 9). This mechanism, allows the tip to continue to solidify at a higher temperature than the interface. If one pays careful attention to the temperature profile of the system, they will be able to perceive that at the very moment in which the perturbation is formed, the liquid is at a lower temperature than the liquidus temperature. Thus, the latent heat released upon solidification will serve to increase the tip temperature up to the corresponding liquidus temperature for that particular concentration. Now, the tip of the perturbation is at a higher temperature than the surrounding liquid which will help on the dissipation of the latent heat generated as the tip continues to grow, to the surroundings. This mechanism also contributes to the tip's continuous growth.

These two mechanisms just described will cause a state change in the tip's surroundings and, in order to be able to understand how the solidification velocity will affect the formation of side arms and the space between them, this state change will be analyzed more carefully. As we already saw, the solute concentration surrounding the tip will increase and this will cause a decrease in the local liquidus temperature, reducing the amount of supercooling at that point. Additionally, the heat that will be conducted to the tip region will also contribute to the decrement of that supercooling, if not extinguish it. Thus, we can conclude that the area around the perturbation is less likely to have another growing arm.

That is why the dendrite structure has spaces between the arms and the size of this space is a function of the length of the area around the perturbation that is being affected by these mass and heat transport phenomena<sup>[5]</sup>.

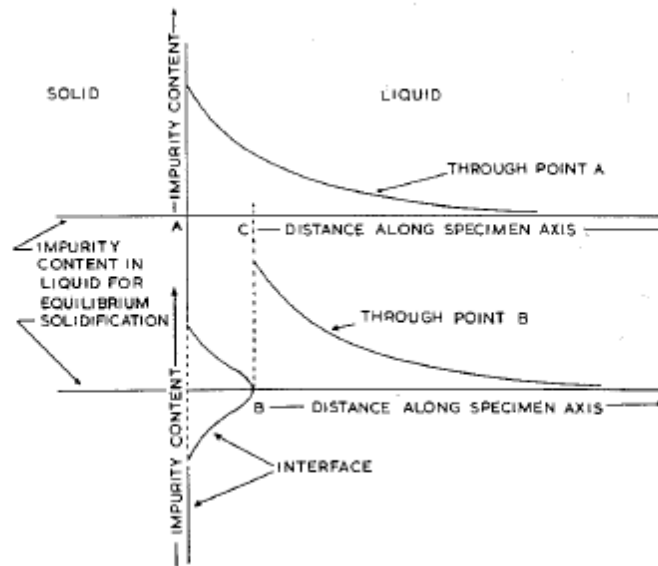


Figure 9 – Scheme showing the solute concentration around the tip of a perturbation<sup>[5]</sup>.

This inter-perturbation area size will be a function of the solidification velocity. The faster the solidification velocity is, the smaller the space between the arms needs to be. As the solidification velocity increases, less time is available for the rejected solute to diffuse to the surroundings. Furthermore, faster solidification leads to more latent heat being released through the perturbation body instead. This will diminish that already mentioned affected area, decreasing the spaces between the arms. Eventually, if the speed of growth goes beyond a certain value, the solid-liquid interface becomes once more a flat plane surface, where there is no time for solute redistribution or for

latent heat to be conducted to the surroundings. This phenomenon is quantitatively described by Mullins and Sekerka<sup>[6]</sup>. Their work shows that, as the growth velocity increases, starting from very slow velocities, there will be a transition to the interface shape from planar to dendritic and back to planar again.

The fundamentals of the model just described extend to the formation of secondary arms as well, although a more-complicated scenario would be present in this case.

### **2.3) Casting**

Casting of metals is an antique technique and the exact period that it arose is unknown. Metals started to become mastered in the Chalcolithic period, dated approximately between 5000 and 3000 B.C (prior to the Bronze Age)<sup>[20]</sup>. It is believed that casting began somewhere during that period as analysis made on artifacts from that time show chemical compositions that suggest their being cast from native copper<sup>[20]</sup>.

With the Bronze Age (~3000 B.C.) came more rapid development of casting technologies. Figure 10 shows an example of a stone mold used for casting during that period<sup>[20]</sup>. During this period, early alloys were composed of arsenic and copper. Later, the well-known bronze age emerged, when alloys of copper and tin were discovered and mastered<sup>[20]</sup>. There are records, also from that age, of the use of two parts mold, which improved the casting of bilateral symmetry objects, such as axes and swords (Figure 11)<sup>[20]</sup>.

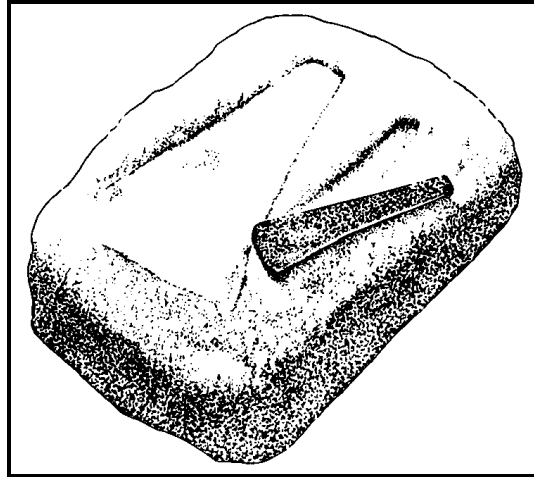


Figure 10 - Bronze age stone mold<sup>[20]</sup>.

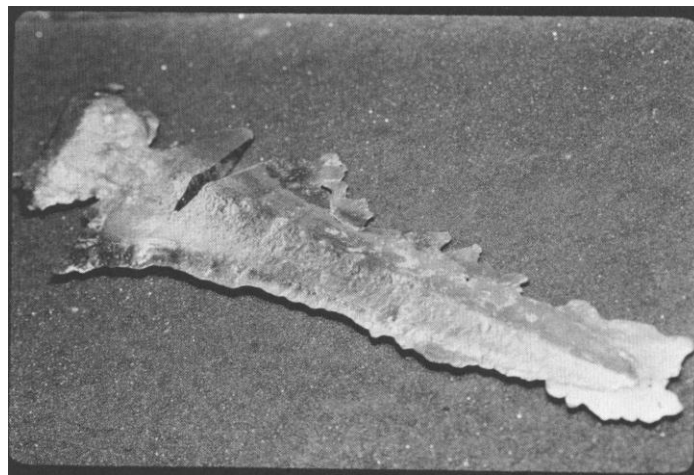


Figure 11 – Bronze Age sword replicate made using a bivalve mold done by Dr. Peter Northover, Oxford<sup>[20]</sup>.

Around 600 B.C., cast iron appeared in China. However, its appearance in Europe is dated somewhere near the 15<sup>th</sup> century A.D., almost 1600 years later<sup>[20]</sup>. And only in the 18<sup>th</sup> century did cast iron become an industrially important material with the emergence of mass production capability. This

century was also the earliest reliable record of industrial steel making, when Huntsman, made his advances in refractory crucibles, permitting him to become the first to pour steel as a liquid<sup>[20]</sup>. Over the following 100 years, steel castings started to be made. Since these early developments, many different types of casting processes have been developed, and they are a very important piece in manufacturing nowadays.

#### **2.4) Material Properties vs. Dendritic Arm Spacing (DAS)**

Much research has been done on the role of dendrites in material properties. Generally, a material's mechanical properties improve with a decrease of the dendrite secondary arm spacing ( $\lambda_2$ ). A sampling of this now-well-established connection between dendrite morphology and properties includes (for example) Lim et al.<sup>[7]</sup>, who worked with 3 different types of castings, showing how the ultimate tensile strength (UTS), elongation, reduction of area and Young's modulus all increased as the secondary DAS decreased (Table 1 and Figure 12).

Table 1 – Cast LM25 alloy properties<sup>[7]</sup>

	UTS (MPa)	Elongation (%)	Reduction of Area (%)	E (GPa)	DAS ( $\mu\text{m}$ )
Investment casting (IC)	160	5.5	5.5	69	33.31
Pressure Assisted IC	188	6	6	73	23.74
Squeeze Casting	243	7	7	78	11.43

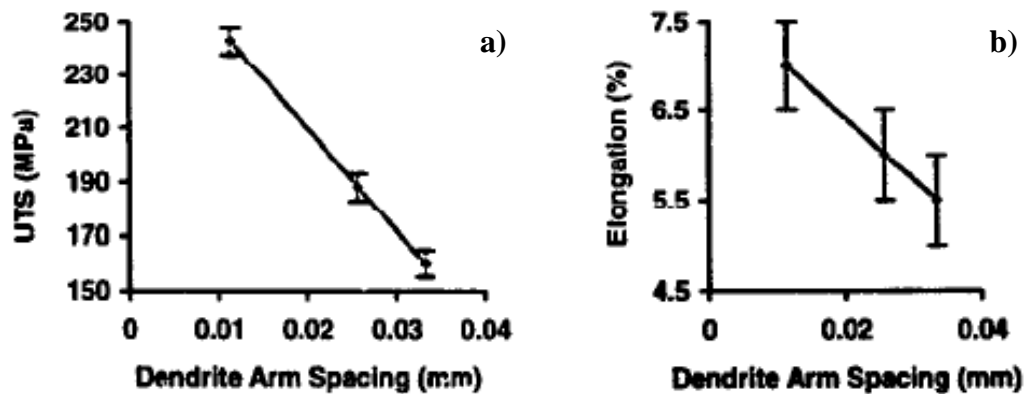


Figure 12 – a) Graph showing how the UTS varies as a function of the DAS; b) Graph showing the variation of the elongation as the DAS values decrease<sup>[7]</sup>.

To investigate how the microstructure and solidification thermal variables of Al-Si castings affect mechanical properties, Goulart et al.<sup>[8]</sup> conducted experiments and also found that the UTS increases as the DAS decreases, for either silicon concentration (5 and 9 wt.%). (Figure 13)

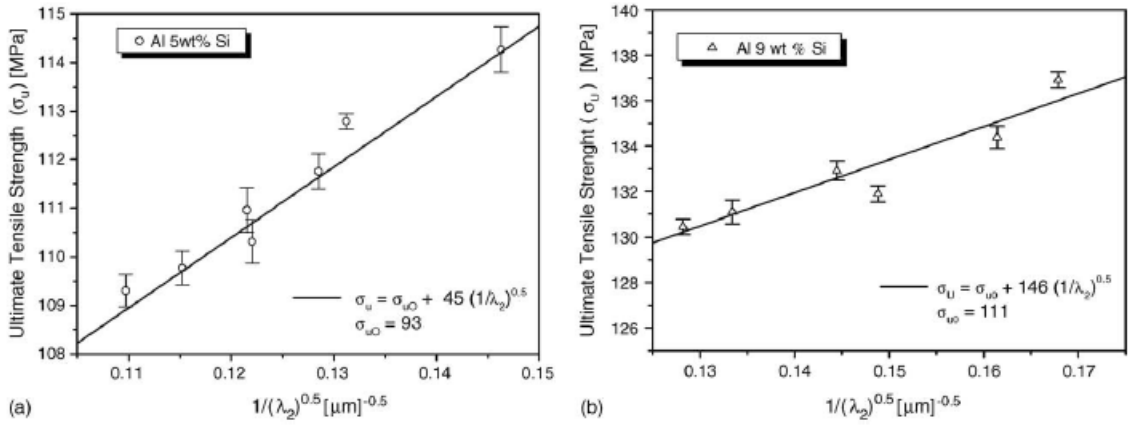


Figure 13 – UTS variation as the secondary DAS values increase for both Aluminum alloys containing 5 and 9wt% of Si<sup>[8]</sup>.

Additionally, Santos et al.<sup>[9]</sup> found that both UTS and yield strength increase as the DAS decreases for a Zn<sub>27</sub>Al alloy (Figure 14).

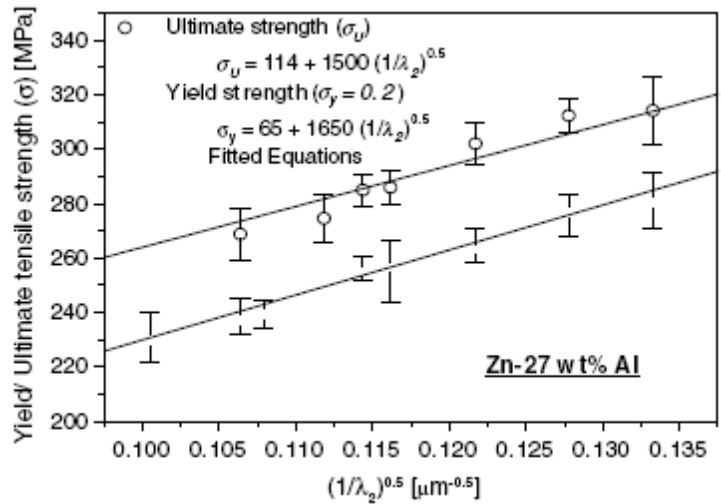


Figure 14 – Changes in the Ultimate tensile strength and Yield Strength as the secondary DAS values increase for a Zinc alloy containing 27wt% of Aluminum<sup>[9]</sup>.

Each of these studies reaffirmed the importance of the secondary DAS for the mechanical properties and why scientists and engineers seek to better understand dendrite formation mechanisms and, ultimately, find ways to control it.

Some work has been done on this regard. Han et al.<sup>[10]</sup> reported that finer hypoeutectic Al-Cu alloy microstructures could be achieved by applying pressure during the solidification process and that the dendritic cell size decreases as the applied pressure value increases (Figure 15). They attributed this behavior to the increment on the metal/mold interface heat transfer coefficient due to the pressure application, which would lead to a faster cooling rate (Figure 16) and consequently to smaller dendritic cells.

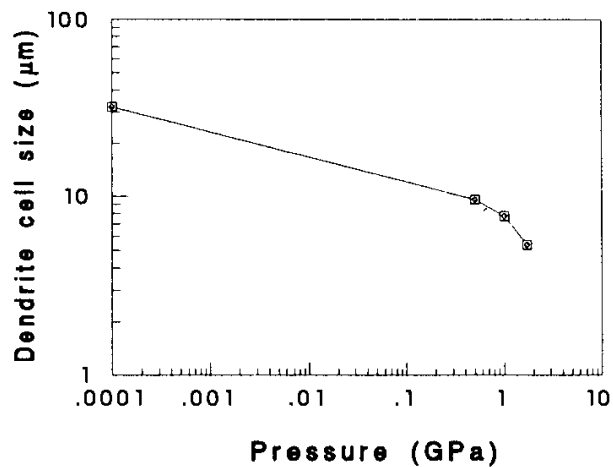


Figure 15 – Dendritic cell size as a function of Pressure applied during the solidification process<sup>[10]</sup>.

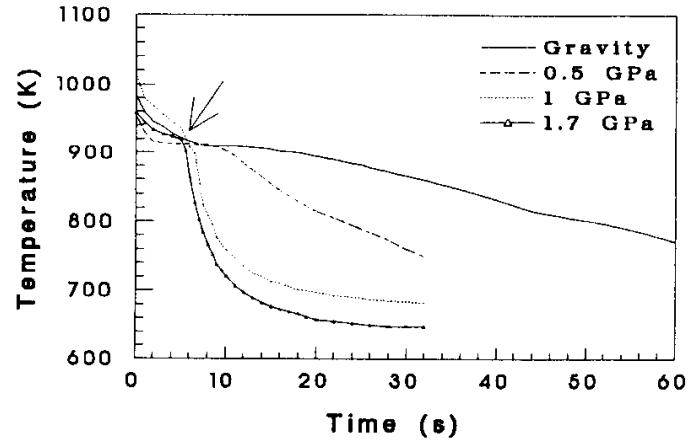


Figure 16 – Solidification time curves for casting of Al-5.4wt%Cu under no pressure (gravity) and pressures of 0.5, 1.0 and 1.7 GPa<sup>[10]</sup>.

This response (not including the decrease in the DAS values) was also noticed by Yu et al.<sup>[11]</sup> when solidifying a magnesium alloy (AM50A) using a squeeze casting process. Figure 17 shows how the application of constant pressure changed the cooling profile and the solidification time of the sample. As the pressure increased, the solidification time decreased, as expected.

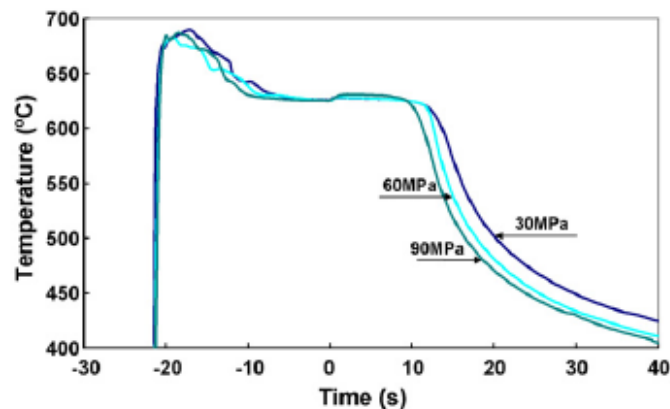


Figure 17 – Solidification time curves for AM50A samples cast under pressures of 30, 60 and 90 MPa<sup>[11]</sup>.

In contrast with these approaches to dendrite refinement (making side branch spacing smaller) an alternative approach is to influence the secondary DAS through the application of some external driving force during the solidification process. Scientists proved that those forces are capable of causing perturbations on the system and, thus, initiate side arms branches formation.<sup>[12,13,14]</sup>

Bouissou et al.<sup>[12]</sup>, interested in the influence that an external flow would cause on a dendritic crystal growth, set up an experiment where a mixture of pivalic acid and ethanol (2 to 4%) was solidified under conditions where no flow and controlled external flow were applied. They could perceive that even when external flow is applied on the growing crystal, the tip shape remains parabolic. Also, the side branches formation is asymmetric when in the presence of external flow. The side most affected by the flow had its side arm formation enhanced whereas on the other side, the formation was inhibited (Figure 18)<sup>[12]</sup>.

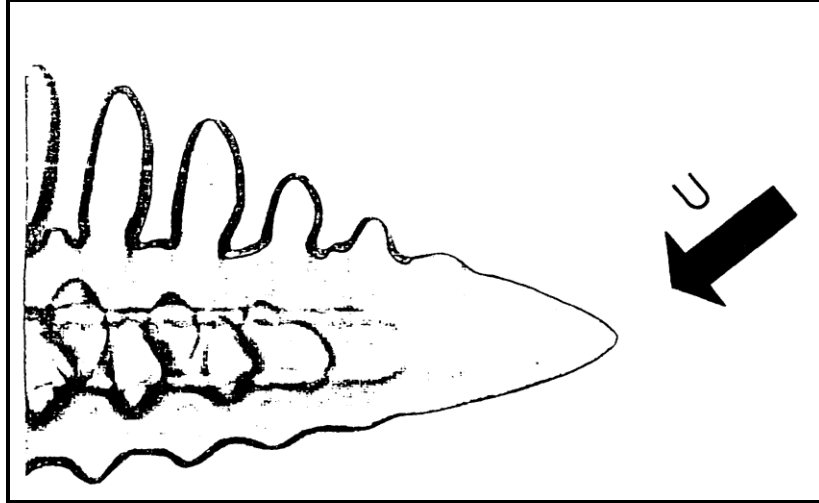


Figure 18 – Dendrite shape when an external flow is present. U in this case is the flow velocity which was equal to  $15\mu\text{m/s}$ <sup>[12]</sup>.

### 2.5) Clapeyron Effect

Despite all the already-mentioned mechanisms to reduce the primary or secondary DAS, the one that is being studied in the present research is novel in that it has potential industrial application. The concept is to use the well-known Clapeyron effect phenomenon<sup>[21]</sup> along with pressure pulses to the melt to decrease the secondary DAS of the material. The dependence of a material's melting temperature on the ambient pressure can be described mathematically by the Clausius-Clapeyron equation:

$$\frac{dT}{dP} = \frac{T_m \Delta V}{\Delta H} \quad , \quad (1)$$

where  $T_m$  is the melting temperature at a reference pressure,  $\Delta V$  is the molar volume change during solidification and  $\Delta H$  is the molar latent heat of fusion.

This equation can be written more conveniently as:

$$\Delta T_m = \left[ \frac{T_m^0 \Delta V}{\Delta H} \right] \Delta P , \quad (2)$$

or

$$\Delta T_m = C_c \Delta P . \quad (3)$$

Here  $C_c$  is called the Clapeyron Coefficient, which is a “figure of merit” for the strength of the dependence of the melting temperature on the pressure. I.e., from equation 3, one can see that a change in the melting temperature can be achieved by changing the system pressure. This was shown by Yu et al.<sup>[11]</sup> in their work. They were able to increase the melting temperature of 5.40°C when applying a pressure equal to 90MPa (Figure 19).

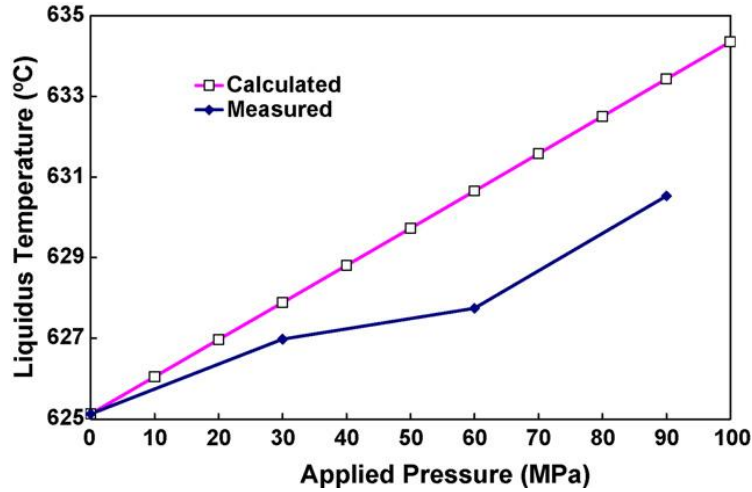


Figure 19 – Different Liquidus temperature for an AM50A alloy for different applied pressure during the solidification process <sup>[11]</sup>.

Depending on the sign and values of  $\Delta V$  and  $\Delta H$ , the melting temperature can be either increased or decreased when the pressure is changed. An estimate of the expected change in the melting temperature for the proposed experimental alloy (Pb-7wt%Sb) was calculated using the  $\Delta V$  and  $\Delta H$  values for the pure elements<sup>[22-23]</sup> being combined with their respective contribution for the alloy (equations 4 and 5). The melting temperature used was the liquidus temperature ( $\approx 280^\circ\text{C}$ ). Table 2 shows the tabulated and the calculated values used in this process.

$$\Delta H_{(Pb-7wt\%Sb)} = (0.93 * \Delta H_{(Pb)}) + (0.07 * \Delta H_{(Sb)}) \quad (4)$$

$$\Delta V_{(Pb-7wt\%Sb)} = (0.93 * \Delta V_{(Pb)}) + (0.07 * \Delta V_{(Sb)}) \quad (5)$$

Table 2 –  $\Delta H$  and  $\Delta V$  tabulated and calculated values for Pb and Sb pure elements and alloy.

	$\Delta H$ (J.g <sup>-1</sup> )	$\Delta V_{L-S}$ (cm <sup>3</sup> .g <sup>-1</sup> )	$T_m$ (K)
Pure Pb	24.7 <sup>[22]</sup>	0.005 <sup>[22]</sup>	600.45 <sup>[23]</sup>
Pure Sb	163.6 <sup>[22]</sup>	0.006 <sup>[22]</sup>	903.15 <sup>[23]</sup>
Pb-7wt%Sb	34.4	0.005	553.15

From the calculated values it is possible to obtain  $C_c$ , which was found to be 0.081K.MPa<sup>-1</sup>. Table 3 shows how the melting temperature would vary for arbitrary changes in the system pressure.

Table 3 – Changes in the melting temperature caused by application of pressure.

Applied Pressure - $\Delta P$ (MPa)	Melting temperature change - $\Delta T_m$ (K)
1	0.081
1.5 <sup>†</sup>	0.122
2	0.162
4.3 <sup>†</sup>	0.348
5	0.405
8.3 <sup>†</sup>	0.672
10	0.810
20	1.620

† – These values were the ones used during the pressure assisted experiments.

As can be seen, the melting temperature will be increased as the pressure is increased, once  $\Delta V$  and  $\Delta H$  are negative for this alloy<sup>[22]</sup>.

## **2.6) Goals of this Study**

Summarizing, the main goal of this project is to develop a new technique to control (decrease) the secondary arm spacing in directionally-solidified (cast) dendritic microstructures. This will be attempted by applying cyclic pressure to the mold apparatus containing the molten sample, which, due to the Clapeyron effect, will make the system melting temperature oscillate in time, generating pulses of enhanced supercooling to initiate interfacial perturbation formation in a periodic manner. This is postulated to create enough energy to initiate new dendrite arms and, consequently, obtain a finer periodic sidebranch microstructure. The features and details of this work will be presented more carefully in the next chapters.

### 3) MATERIALS AND METHODS

This chapter will focus on the materials and methods utilized in this project.

The performed experimental procedures are divided into 5 steps. The first step consists of melting the Pb and Sb components and combining to form the desired Pb-Sb alloy. This is then; poured into a pre-heated cylindrical mold that is inside a ceramic 2-zone heater cartridge, made with heater coils in its top and bottom parts. These heater coils are controlled by two temperature controllers, commanded by LabVIEW software. A total of 8 thermocouples (2 of them for the controllers) are used to measure the temperature profile along the mold, with readings acquired every second, by a separate LabVIEW program. These data can be recorded at any time and exported to a Microsoft Excel spreadsheet for post-experiment analysis.

The second phase of the experiment begins when, after pouring the molten metal into the piston cylinder, a solid metal piston is placed into the mold (cylinder). The piston is what will be used to transmit pressure to the melt in either a cyclic or constant manner. This pressure is applied by means of a hydraulic MTS mechanical testing machine configured as desired.

After the piston mold apparatus is under pressure, the third step takes place. The heaters are turned off and a cooling water stream, which flows underneath the mold, is then opened causing the bottom section to cool rapidly, resulting in a directional solidification process that results in aligned dendrites, growing in the direction of the applied temperature gradient.

The fourth step is the sample removal from the mold, followed by its preparation for quantitative microscopy analysis. I.e., the sample is sectioned, mounted and polished in order to allow the microstructure to be imaged and measured.

The cross-section samples are then measured in a microscope and detailed measurements of the secondary arms are obtained. Afterwards, these are correlated with their position inside the mold and plots showing how the secondary arms spacing varies according to the mold position are generated. These data, are then combined with separately-derived data correlating the local solidification rate to the local position within the mold. When combined with the microscopy results, correlations between the side branch spacing and the local solidification rate result.

A more detailed description of each experimental step will follow.

### **3.1) Sample preparation**

The alloy used in this work was a hypoeutectic Pb-Sb alloy (Pb-7wt%Sb), which has a nominal melting point (liquidus temperature) of approximately 280°C. It was prepared by weighting the corresponding amount of 99.9% purity Lead wire and 99.8 purity Antimony rod (both from Alfa Aesar) using a Ohaus 1600 series balance and putting them in a crucible (Figure 20). The total sample weight was typically 195 grams. The crucible was then placed in a NEYTECH Qex vacuum furnace in order to melt the alloy (Figure 21). The furnace was evacuated to prevent the formation of lead oxide during the melting process. The

melting point of pure lead and antimony are 327.502 and 630.755°C<sup>[15]</sup>, respectively, so, the furnace was set to 700°C, held at that temperature for 20 minutes then cooled to the 365°C pouring temperature. At the same time, the pouring ladle was also heated to the same pouring temperature in a Barnstead Thermolyne 48000 furnace (Figure 22) to keep the liquid from solidifying during the pouring process.

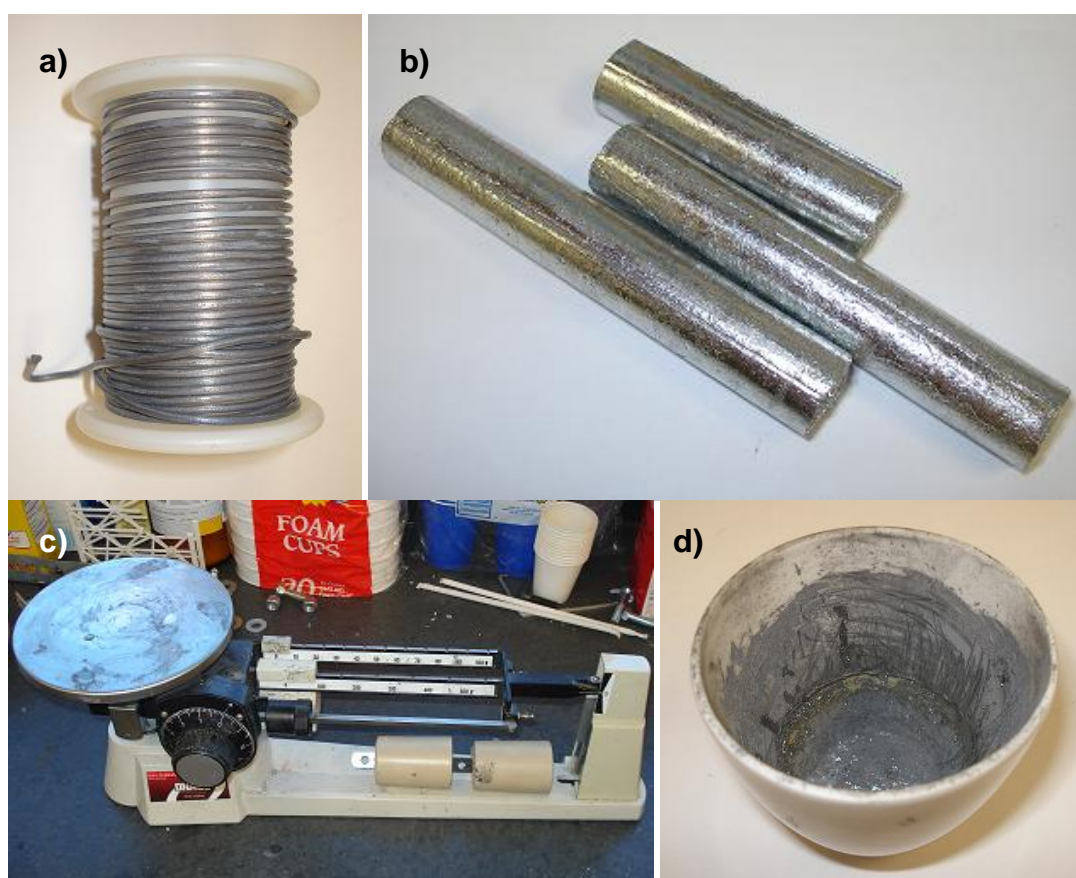


Figure 20 – a) Lead and; b) Antimony materials used to compose the sample. c) Balance used in the process and; d) crucible where the material was placed into.



Figure 21 – NEYTECH Qex vacuum furnace.



Figure 22 – Ladle inside the Barnstead Thermolyne 48000 furnace prepared to be heated.

### 3.2) Mold

Figure 23 shows the mold used to cast the sample. The whole mold comprises of 3 main parts: the die (cylinder at top), a chill plate (rectangular

plate), and a water reservoir where the cooling water flow passes through. All parts were made of stainless steel because of its favorable mechanical properties and corrosion resistance<sup>[4]</sup>.

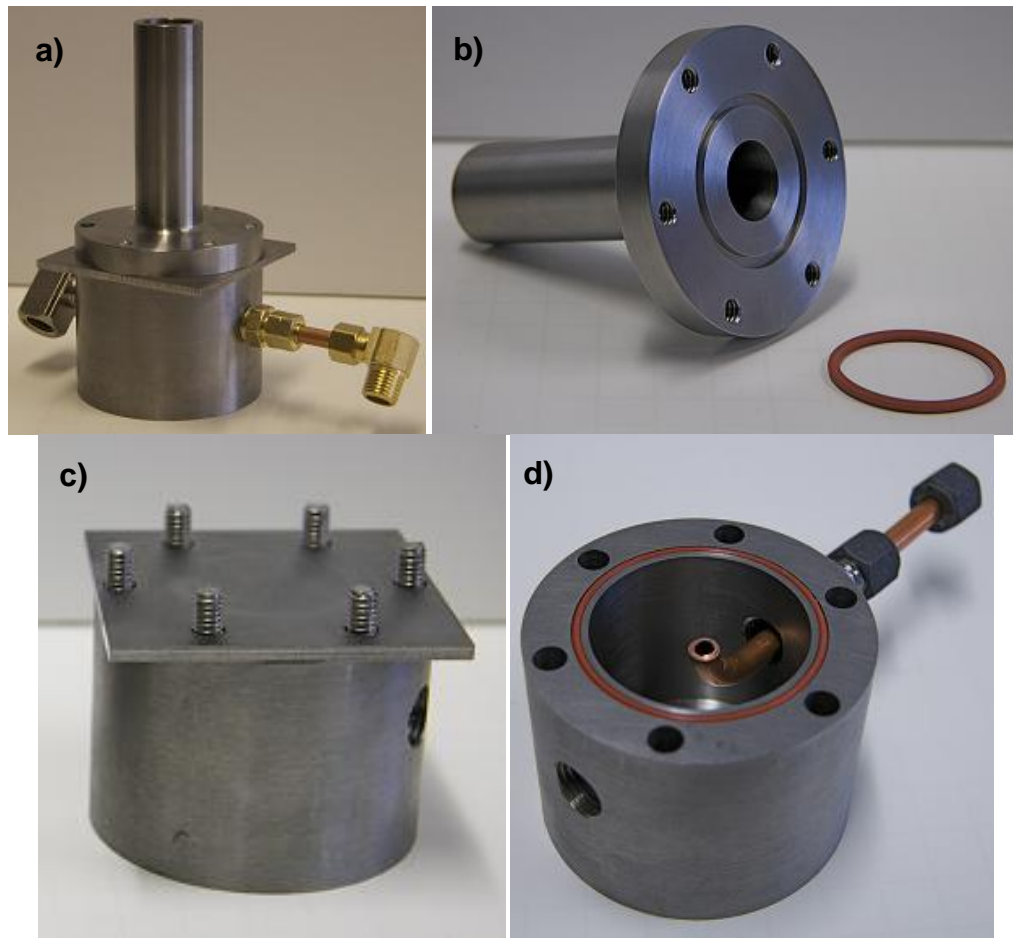


Figure 23 – a) Mold apparatus completely assembled; b) Picture of the die part showing the utilized O-ring and its groove; c) Bottom part of the mold together with the chill plate and; d) Picture showing the water pipes pointing straight to the chill plate and the O-ring placed on the water reservoir.

Figure 24 shows a schematic of the mold including some of its dimensions (refer to Appendix A for full page version of the drawings). As noted in the previous figure, both the die cylinder and the water reservoir have o-ring grooves, to constrain flow of water (on the cooling side of the chill plate) or liquid alloy (on the hot die side). Silicone o-rings were used on both sides. On the high-temperature side, high-temperature o-rings were also useable (although at dramatically higher cost than silicone).

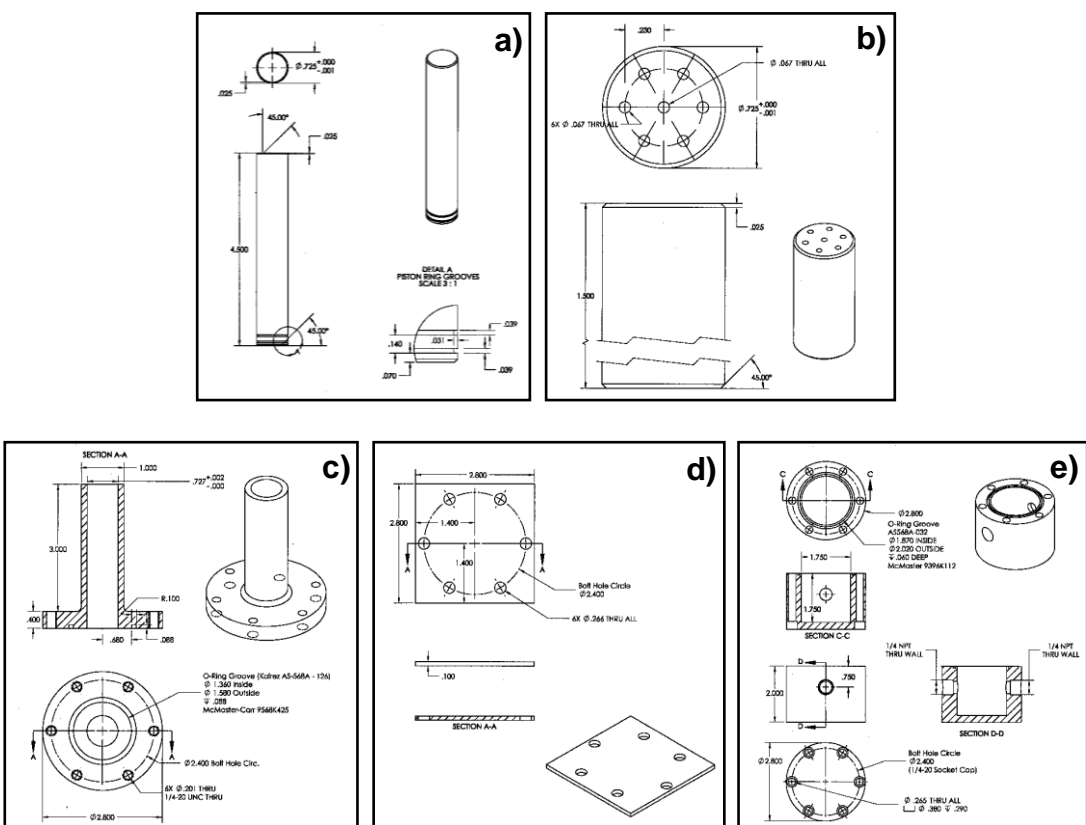


Figure 24 – Mold Schematic created using SolidWorks 2007®; a) solid piston; b) small piston with holes; c) top part of the mold; d) chill plate and; e) bottom reservoir.

The water reservoir also has two side holes where the coolant hoses are connected (Figure 25). Before assembling all the parts, the inside surface of the die is coated with a thin layer of Permatex anti-seize lubricant 133k to facilitate insertion and removal of the piston and later sample removal (Figure 26).

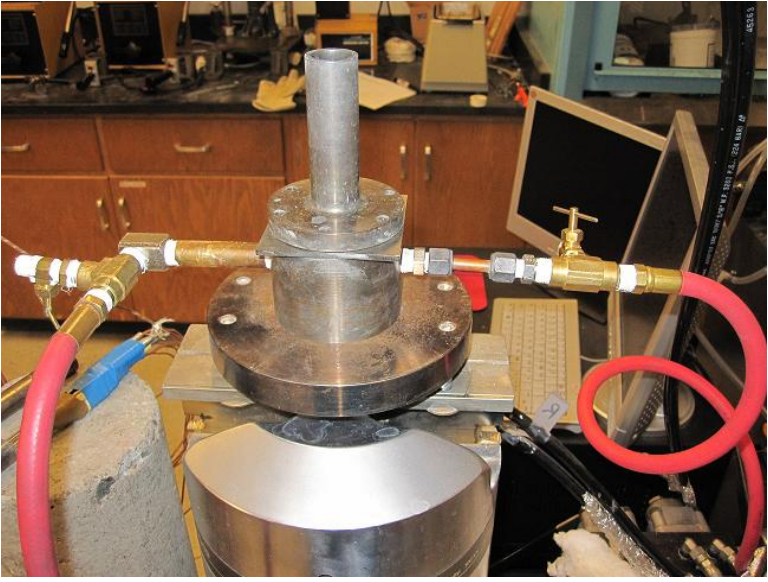


Figure 25 – Pipe and hose connections responsible for the water flow.



Figure 26 – Anti-seize lubricant used to ease the sample removal from the mold.

### **3.2.1) Ceramic Heater**

An image of the 2-zone heater cartridge is shown in Figure 27. It was made using OMEGABOND® OB-600 high temperature chemical set cement, which was poured into a sacrificial polymeric mold (Figure 28), designed using SolidWorks 2007® software and fabricated using a 3D printer. Figure 28 shows a schematic of the inside part of the heater with some of its dimensions (refer to appendix A for full page version of the drawings). As can be also seen from Figure 28, twelve wood sticks were inserted into the mold side wall, to create twelve thermocouple holes for temperature measurements (the wood burns out on first use). The ceramic slurry was then poured into the mold and left to cure for one day at ambient temperature. An oven drying process of 4 hours at 180°F followed by 4 more hours at 220°F was performed as recommended by the ceramic supplier to help prevent flaking and chipping by mainly eliminating any residual water that could still be inside the ceramic mold. Next, the polymer sacrificial mold was removed using tools (as much as possible), followed by heating the ceramic up to 800°F in order to burn out all the remaining polymeric and wood material, leaving only the ceramic form of the heater cartridge.



Figure 27 – Ceramic heater showing the heater coils end.

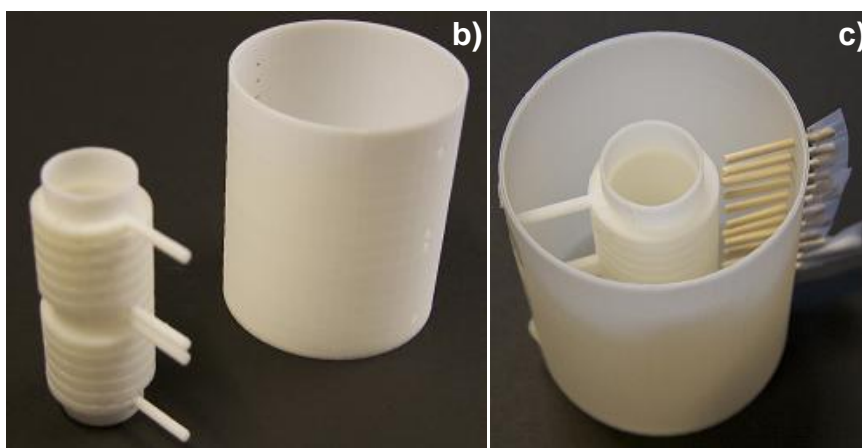
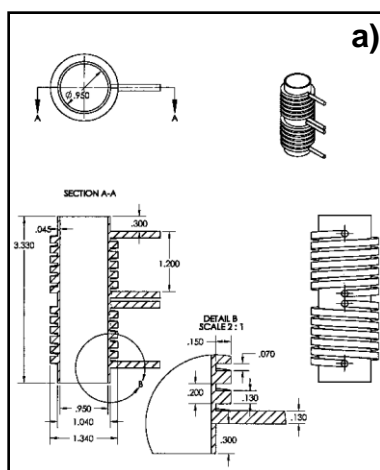


Figure 28 – a) Schematic of the inside part of the mold; b) and c) polymeric mold and plug for casting the ceramic heater cartridge.

The ceramic mold was now ready to receive the heater coil. The coil used in this task was the NIC60 heater coil made by Omega with a composition of 60% Ni, 16% Cr and 24% Fe, and a compacted diameter of 3.2mm (Figure 29). The coil was extended by four times their initial length. (According to the manufacturers, these coils should not be used without extending them at least three times their compacted length). The coils were then inserted into the mold grooves (Figure 29) as tightly and as careful as possible, leaving a small coil piece heading out the mold, which would be connected to the heater power supply controllers. Finally, the ceramic heater is placed over the steel mold to complete the mold apparatus (Figure 30). A 0.1mm thick sheet of Mica (Figure 30) is placed between the inside diameter of the heater and the outside diameter of the die cylinder to prevent the coils from (electrically) contacting the outside of the mold surface to avoid electrical grounding of the coils.



Figure 29 – a) Inside part of the (split in two) ceramic heater showing the metal coil grooves and; b) NIC60 coils used on this task.

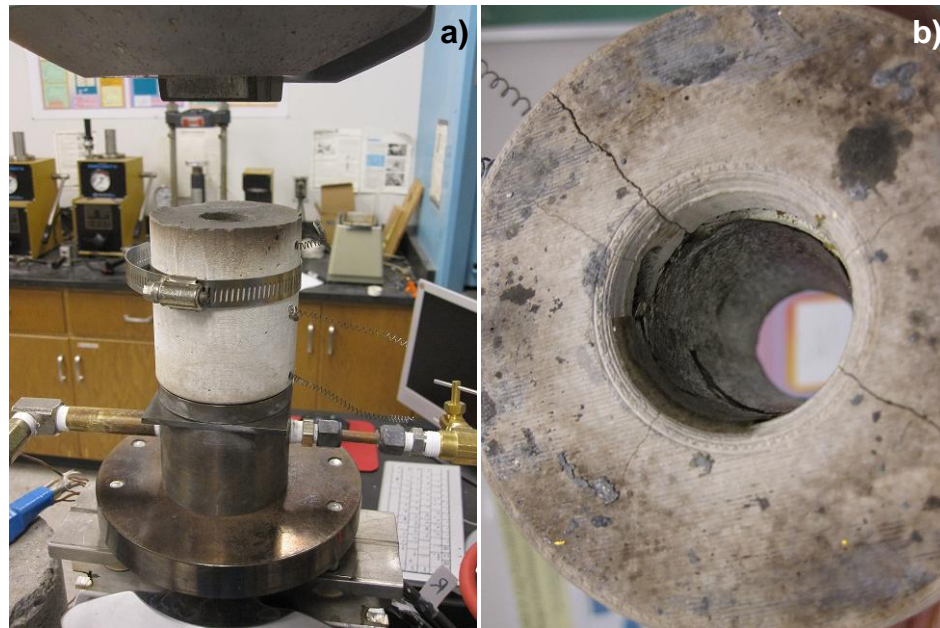


Figure 30 – a) Die-Casting mold together with the ceramic heater and; b) Interior of the heater cartridge, showing the mica sheet used as an electrical insulator.

### 3.3) Cooling System

The cooling system is comprised of a pressure gauge and flow meter used to measure the water flow rate in gallons per minute (GPM), a thermocouple to measure the water temperature, water supply hoses, and fittings. Figure 31 shows the system setup used in the experiment. Initially, the cooling water used was directly obtained from a tap. This tap was connected to the pressure gauge, which is followed by the thermocouple. 1.3GPM was the initial flow rate used for the experiments. Later, it was found that a slower solidification rate was needed. To accomplish this, a fluid heater/circulator – Neslab RTE-111 - (Figure 32) was filled with water that had its temperature kept at around 50°C. The flow rate was also decreased to 0.05GPM to help slow the solidification process to the desired

level. Similarly, a more rapid solidification process could be explored with this apparatus using chilled water at a higher flow rate. A hose conducts the water to the inlet of the mold that directs the water to splash directly onto the chill plate's bottom surface (Figure 23). The cooling water flow keeps moving through the outlet, and is guided by hoses and fittings to the sink to be disposed. A bypass line was incorporated into the cooling water system to provide further control over the water temperature, allowing it to be increased without running water through the pipes (Figure 32). Finally, each side of the mold piping also contains a bypass valve (Figure 25) that allows emptying the reservoir without having to disassemble the tubing connections.

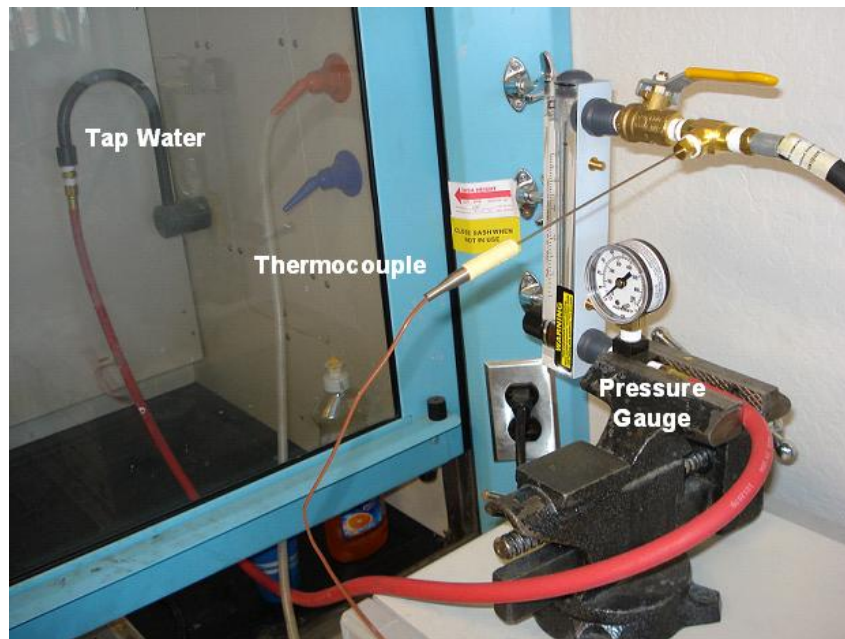


Figure 31 – Scheme of the water flow apparatus.

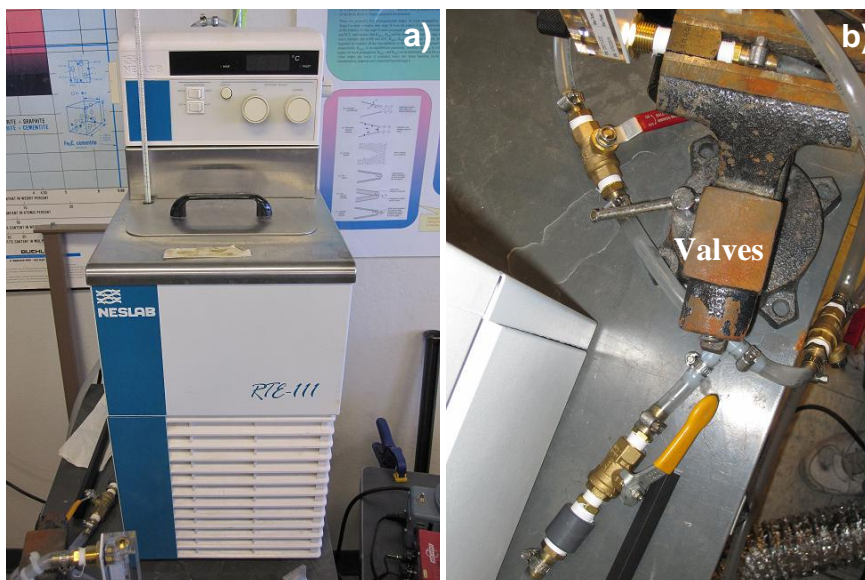


Figure 32 – Temperature controlled cooling system; a) Fluid circulator used to keep the water at the desired temperature and; b) some of the open and close valves utilized to redirect the water flow as necessary.

### 3.4) Data Acquisition System

The LabVIEW programming environment was used to create the custom programs that would either acquire data from the experiment or communicate with the temperature controllers (Figure 33). In order to obtain the temperature signals, a data acquisition board (Figure 33) was used together with eight K-type SCC-TC02 thermocouple input modules allowing the temperature acquisition program to acquire and save, whenever necessary, all eight temperature channels simultaneously. Two more K-type thermocouples completed the temperature measurement set, which were connected to the heater controllers giving the necessary feedback to maintain the desired temperature. These signals could also be acquired by the LabVIEW program used to communicate

with the controllers. An overview of the display of each program is shown in Figure 34, showing the main features of each program, such as turning on and off the controllers, changing their set point, showing a real-time plot of the temperature as a function of time for each single thermocouple, and more.

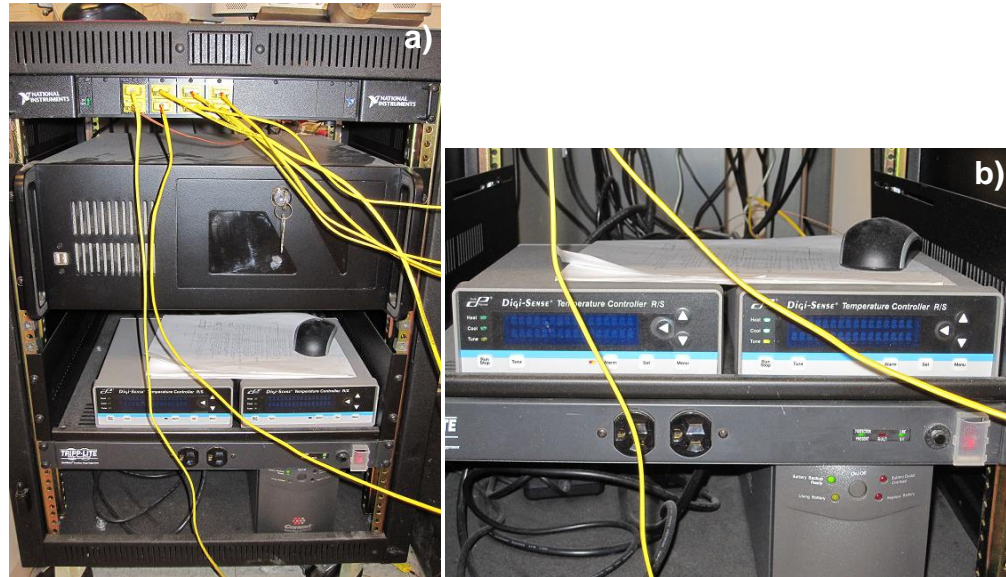


Figure 33 – a) Controllers and data acquisition board used in the experiment and; b) Controllers magnified view.

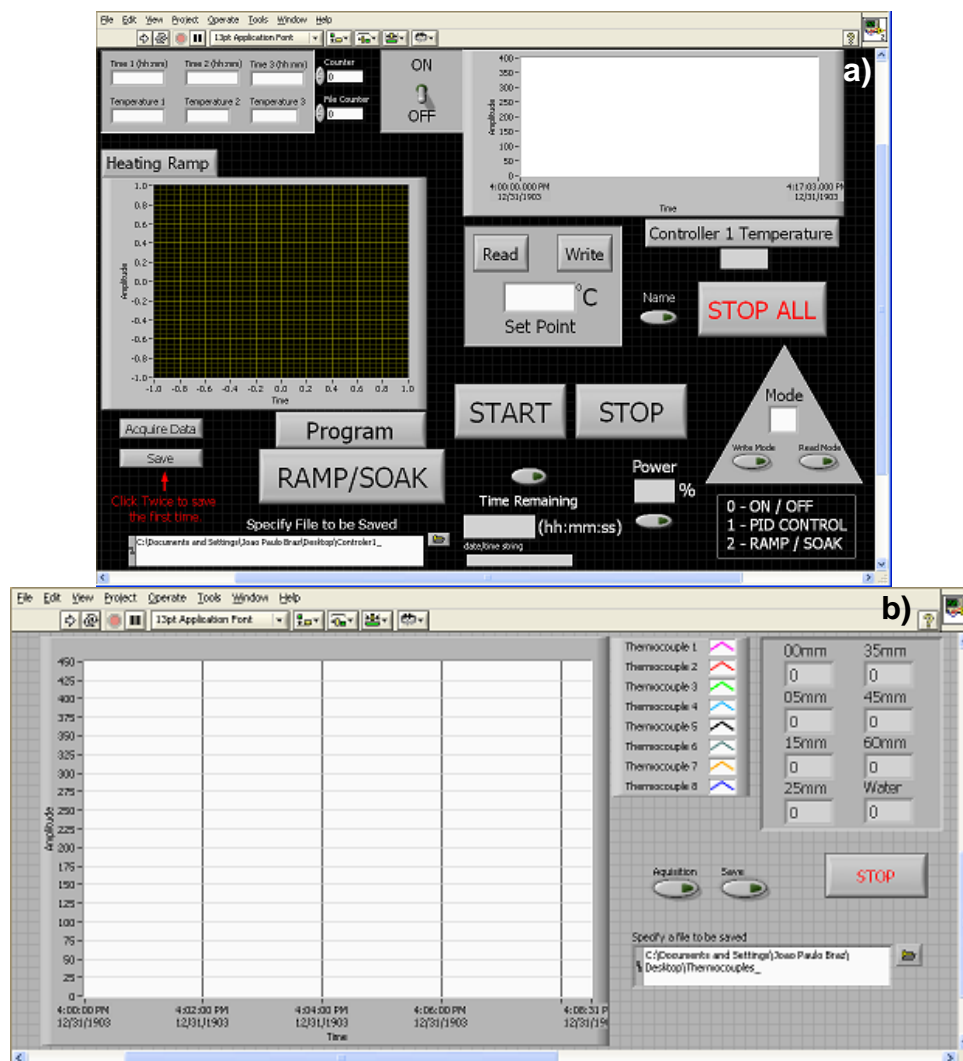


Figure 34 – a) Image of the interface of the program that controls the heaters and; b) Image of the interface of the program that does the thermocouples readings data acquisition.

### 3.5) Temperature controllers

Two Cole-Parmer temperature controllers model 89000-15 (Figure 33) were used in this experiment (one for each heater zone). As their name suggest, they were responsible for providing power to the heater coils in a controlled manner. A VARIAC (Figure 35) was connected to the output of each controller to further

proportionate a way to control the amount of AC voltage applied to the coils, preventing them from melting. Regular electrical cables ended with alligator clips were plugged into the VARIACs output, while the alligators were clipped at the coils sticking out the mold to close the circuit (Figure 35). The voltage was regulated until a point where the coils started to become orange colored, which would normally occur at approximately 80 Volts AC.

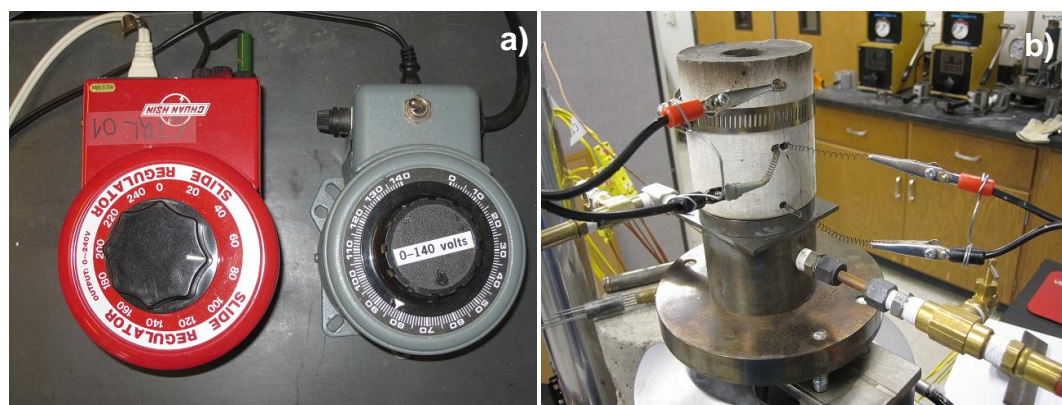


Figure 35 – a) Image of the VARIACs and; b) Alligator clips connected to the heater coils.

After assembling all the mold parts and the cooling and data acquisition systems, the heaters are then turned on, starting the mold heating process. In the situation where a new sample is being prepared, an exhaust fan (Figure 36) is used at the very top of the mold to carry the fumes originated from the anti-seize lubricant to the nearest hood. In the meantime, a prepared sample (described earlier) is sitting inside the vacuum furnace at 365°C, the same temperature that the ladle is held at in the other furnace. After all the fumes were gone, the vacuum furnace is then turned off and while its inside air pressure

reestablishes, the heated ladle is taken from the furnace, using a protective glove. With the aid of tongs, the molten metal is poured from the crucible into the ladle and carefully poured into the cylindrical mold from there. This two-step pouring process is mainly dictated by the difficulty in pouring directly into the small cylinder opening using the crucible. The ladle (with a pour spout) simplifies this greatly. In the case that the sample is already inside the mold, i.e., a reheating process, the fan is not needed because the fumes no longer exist.

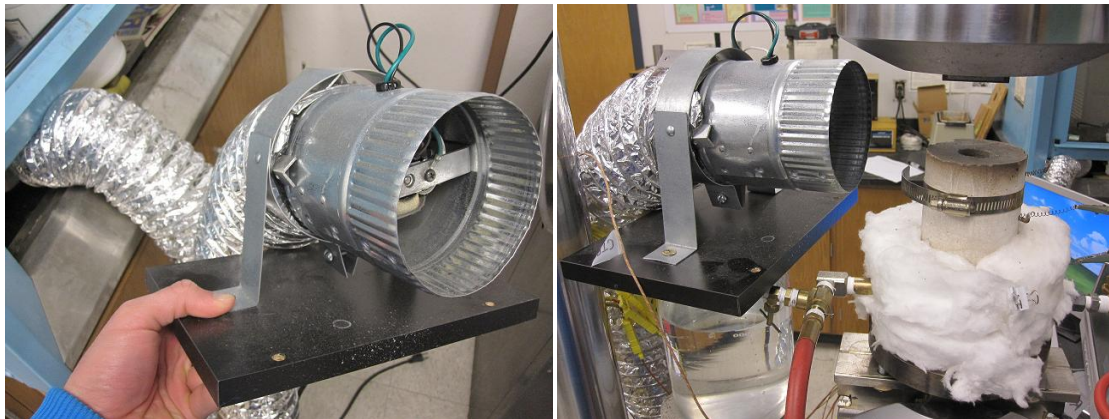


Figure 36 – Fan used as an exhaust system for the lubricant fumes.

### **3.6) Inside Mold Temperature Calibration Measurements**

To better quantify the liquidus solidification velocity, inside mold temperature measurements were carried out during a directional solidification process without the pressure piston in place. Temperature versus time data was used to determine when the advancing solidification front (as indicated by the liquidus temperature) reached each thermocouple's location. To make these measurements, a modified stainless steel piston, with 6 through-holes in it

(Figure 37), permitted 6 thermocouples (Figure 38) to extend to different positions within the cylindrical mold interior. This replicated as much as possible the nominal experimental conditions (minus the pressurization piston). After setting the positions of the thermocouples to fixed locations relative to the chill plate on the bottom, the heaters were turned off and the cooling system was turned on and a graph of how the temperature varied as a function of time, for each specific position, was acquired. This graph was then analyzed to characterize the solidification rate for a given set of cooling conditions (water temperature and flow rate). This set up allowed the measurement of six different positions at once, not only saving time but also giving more realistic and reliable data, as temperatures at all the positions were being measured during the same test. The positions where the temperature was recorded were: 0, 5, 15, 25, 45 and 60mm, with the 0mm one being exactly at the chill plate. Therefore, the thermocouples had a distance of 5, 10, 10, 15 and 15mm from each other (figure 38).



Figure 37 – Perforated stainless steel small piston.

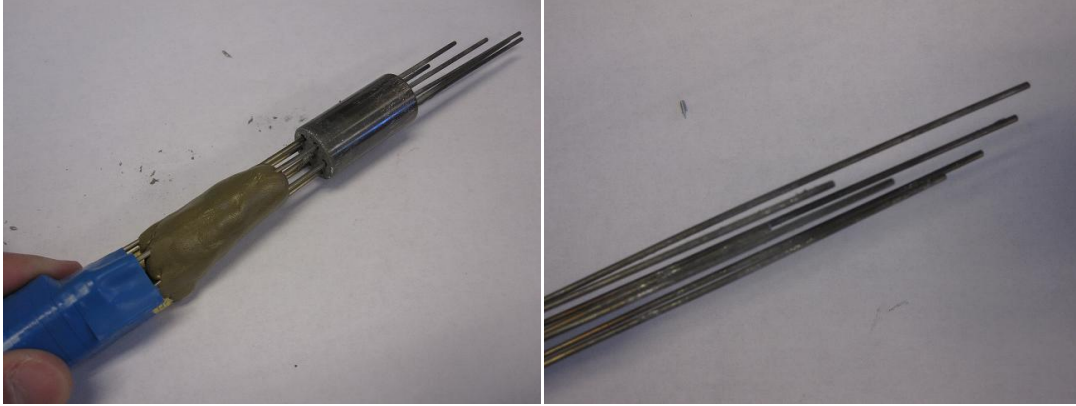


Figure 38 – Thermocouple bundle (six) used to measure the inside mold temperature profile.

### **3.7) Calculation of the Liquidus Velocity for each Position**

The time that the temperature of a certain position took to reach the alloy liquidus temperature (starting at the time where the chill plate – position 0mm – reached the liquidus temperature) can be determined by the procedure mentioned above. The results of such a solidification rate “calibration test” will be presented and discussed later.

### **3.8) Pressurization Using the MTS Machine**

Once the necessary information about the solidification velocity was obtained, experiments with pressure applied were performed. To do so, a hydraulic MTS machine, load frame model 312.31 was used together with a MTS Flex Test SE controller (Figure 39). A fixture was used to secure the piston in place (Figure 40). Again, McMASTER-CARR silicone o-rings were used on the piston grooves to minimize leakage from the mold (Figure 40). The MTS machine

was tuned according to the experimental needs (ex: force oscillation frequency) and the force applied during the experiments was controlled by the controller's software, MultiPurpose TestWare (MTP). During the experiment, a graph shows the force or displacement as a function of time (Figure 41) and these values are recorded by the MTP software for later analysis (refer to appendix B for more information regarding the MTS machine setup). After the experiment is over, the piston is removed from the mold to prevent it from getting stuck.

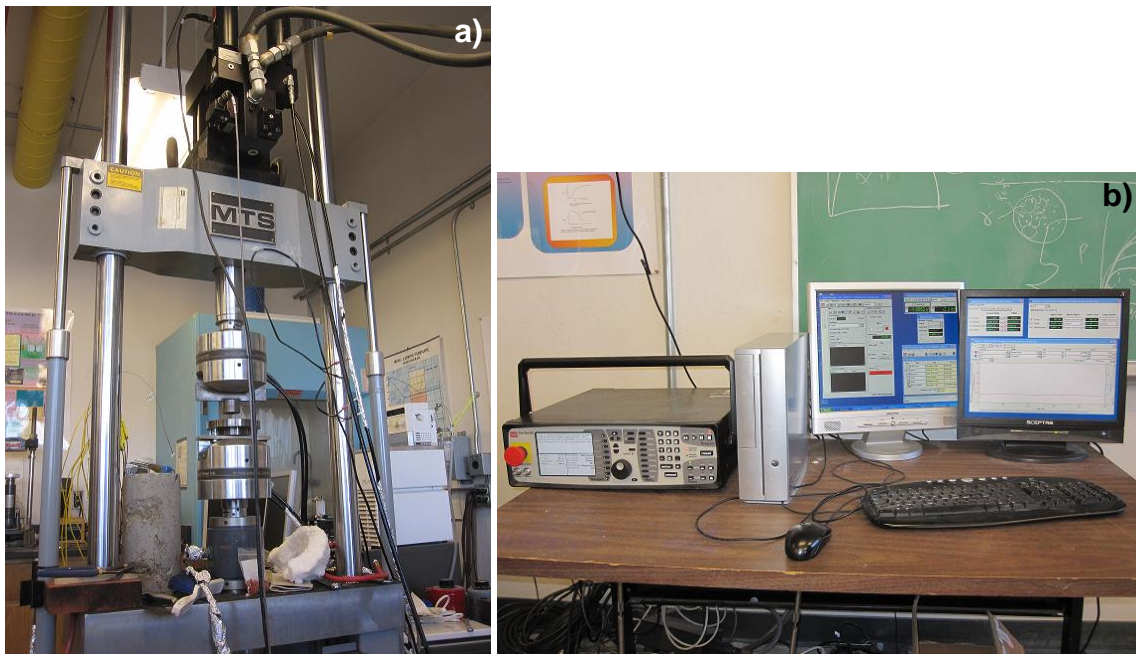


Figure 39 – a) MTS machine and b) MTS Flex Test SE controller used together with the monitor screens showing the computer interface.

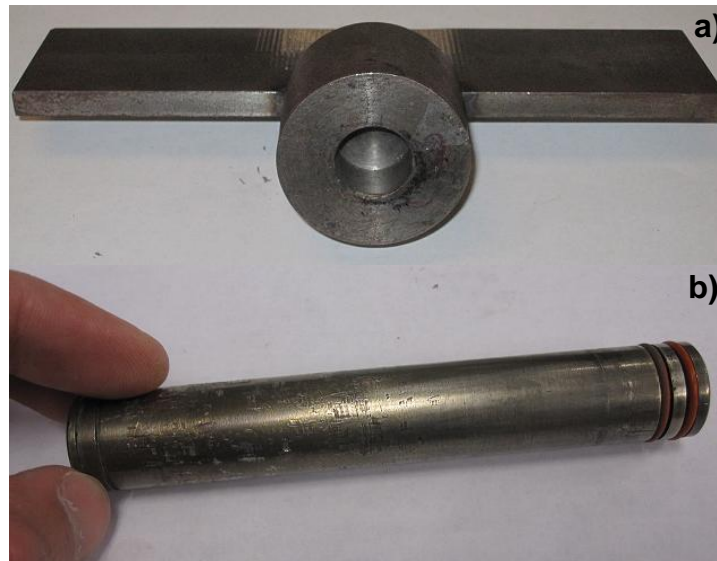


Figure 40 – a) Piston holder and; b) Piston with silicone O-rings.

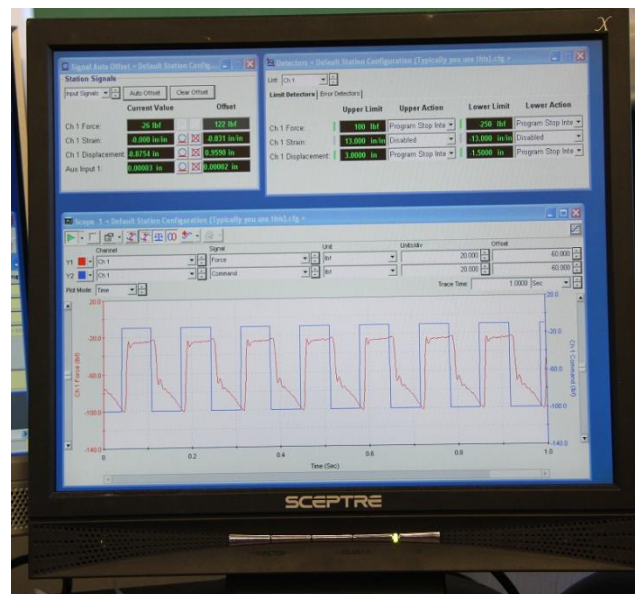


Figure 41 – Graph showing the force variation as a function of the time (controller screen).

### 3.9) Pressure Applied Experiments

Three types of experiments were conducted: those with cyclic pressure, with constant pressure, and without pressure. Figure 42 shows how the experimental

setup looked like when pressure assisted solidification processes were being performed.



Figure 42 – MTS machine applying pressure on the molten metal during a performance test.

The following table (Table 4) summarizes the parameters used for the cyclic and constant pressure experiments. The tabulated force values translate to mold internal pressures via the  $0.413 \text{ in}^2$  piston area.

Table 4 – Force and Frequency values used for the pressure-assisted solidification processes.

Frequency (Hz)	Maximum Force (lbs)		
	110	310	600
0 (Constant Force)	x	✓	✓
5.0	x	x	✓
6.0	✓	✓	✓
7.4	✓	✓	x

The choice of these parameters was based on both the predicted secondary arm formation frequency and the amount of change caused to the melting temperature due to the clapeyron effect. This will be explained in more depth in the next chapter.

When the experiment was conducted without pressure, it was ensured that the mold opening was still covered with the piston (with no pressure applied) in order to replicate the pressure-assisted experiment thermal boundary conditions.

### **3.10) Metallographic Steps**

This section will present all the preparation steps that the cast sample went through prior to the microscope analysis.

#### **3.10.1) Sectioning**

After casting the sample, the same is taken from the mold, the anti-seize lubricant is removed and it is then affixed on a Buehler Isomet 1000 Precision

Saw, equipped with a Buehler Isocut Wafering blade (cubic boron nitride – low concentration), to be sectioned (Figure 43). To prevent excessive heat and allow an easier cut, Buehler Isocut Plus cutting fluid (Figure 43) was used, diluted in 9 parts of water for 1 part of fluid. The sample was cut into 3 pieces (section 1, 2 and 3, numbered starting from the bottom to the top), making sure that the bottom part of the second and the third piece had a distance of 10 and 20mm from the bottom of the mold and the top part of the same third piece was at a distance of 30mm, again relative to the bottom of the casting (Figure 44). The blade kerf (thickness) of 0.4mm was accounted for during this. Each single piece was then sectioned along the longitudinal directional, and readied for mounting in epoxy (Figure 45).

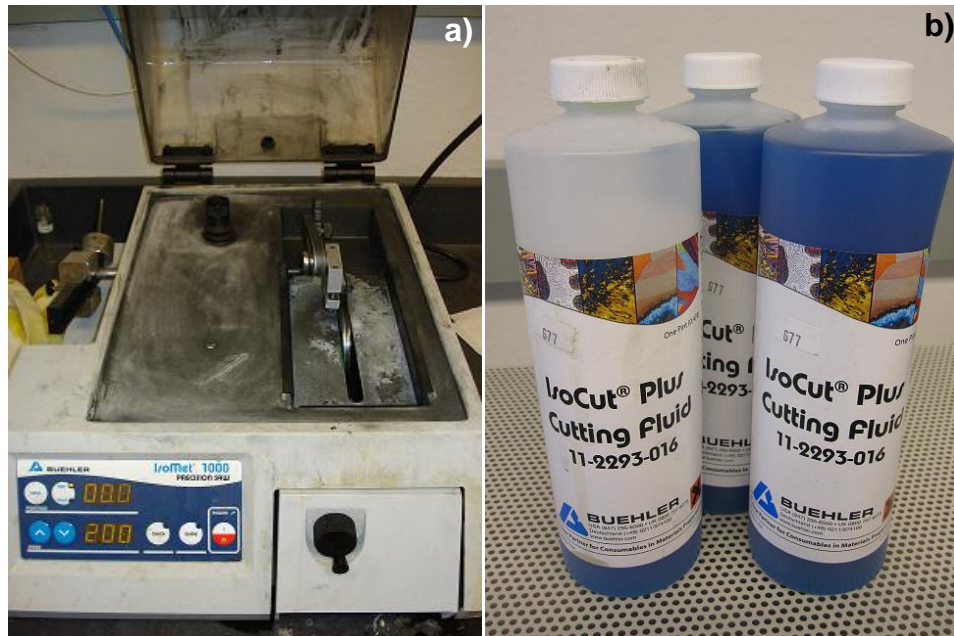


Figure 43 – a) Cutting machine used to section the samples and; b) Cutting fluid.

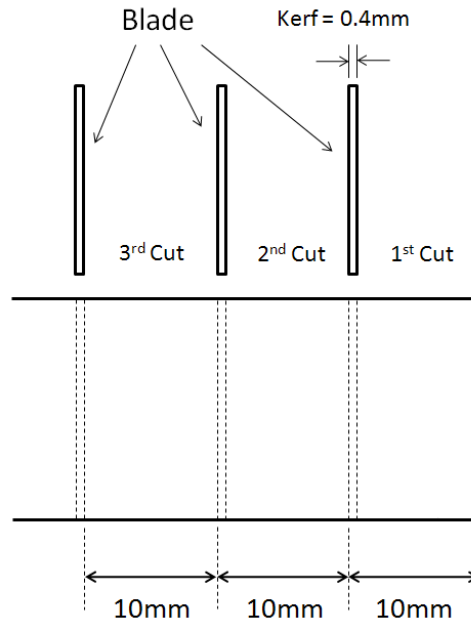


Figure 44 – Scheme of each section dimension within the sample. Notice that the 3<sup>rd</sup> piece is actually 10mm long.



Figure 45 – Sample ready to be mounted.

### 3.10.2) Mounting

The material used to mount the samples was Buehler Epoxicure resin, well-mixed with Buehler Epoxicure Hardener (Figure 46), using a ratio of five parts of resin for one part of hardener. This resin was chosen because of its low curing

process temperature (28°C), and the concern that high temperatures during the curing process could cause some change in the sample microstructure such as coarsening. To mount them, the sample pieces were put inside Buehler mount cups (1 ¼" diameter) facing down (longitudinal and cross section faces for each section). Before that, Buehler Silicon Mold Release was sprayed over the cups to ease the later detachment of the mounted sample (Figure 46). The resin-hardener mixture is poured into the cup in such way that the samples are completely covered by it (approximately 0.75" deep). The resin is left to cure for about 6 hours.



Figure 46 – a) Epoxy and Hardener used to produce the mounting mixture; b) Samples inside the mounting cups ready to be filled with the epoxy and; c) Mold releaser used to facilitate the sample removal from the cups.

### 3.10.3) Grinding and Polishing

After the epoxy is cured, the samples are ready for the grinding and polishing process. A Buehler Ecomet 3000 - Variable Speed Grinder-Polisher,

together with a Buehler Automet 2000 – Power Head was used in this task (Figure 47). The samples were placed in the sample holder and placed on the head of the grinding machine. The parameters and grinding paper grits (Figure 47) used for each step are shown in Table 5. Due to the sample's relative softness, all papers were first covered with regular candle wax to minimizing embedding of the grinding particles into the samples, especially the 600 and 800 grit papers, for which a wax coating step was included between each 3-minute run. A tap water stream was also used to cool the samples during the grinding process.

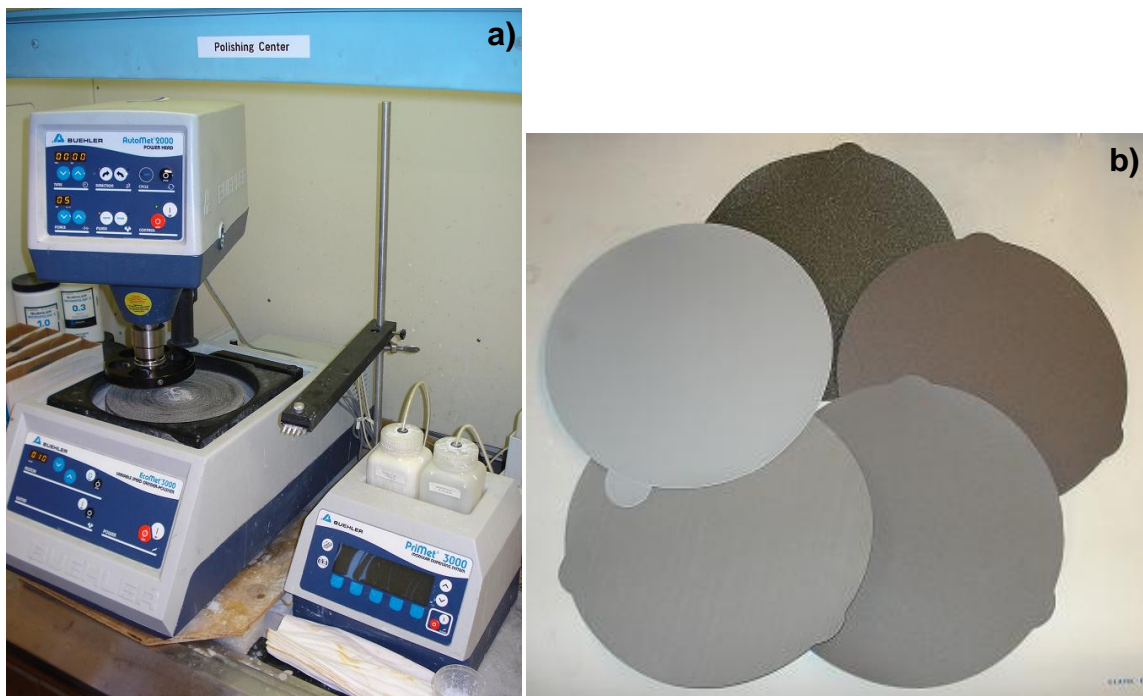


Figure 47 – a) Grinding and polishing machine apparatus and; b) Several grits used on the grinding process.

Table 5 – Grinding process parameters

Paper Grit	Speed (RPM)	Direction	Duration (min)	Load (lbs/specimen)
240	200	Complementary	5:00	2
320	200	Contra	5:00	2
600	200	Complementary	2 x 3:00	1
800	200	Complementary	2 x 3:00	1

For the polishing process, a Buehler Primet 3000 – Modular Dispensing System (figure 47) was used to automatically fill the cloth with the polishing fluid suspension. Buehler Micropolish II deagglomerated Alpha and Gamma Alumina powder were used diluted in deionized water as abrasive particles. Table 6 shows the parameters used for each polishing step.

Table 6 – Polishing process parameters

Particle size ( $\mu\text{m}$ )	Speed (RPM)	Direction	Duration (min)	Load (lbs/specimen)
0.3	140	Complementary	5:00	1
0.05	120	Contra	5:00	1

The samples were washed with high-flow tap water right after each step to prevent the alumina particles from getting stuck and dried to the sample surface. Deionized water was then splashed on the samples surface, followed by a final rinse with ethanol.

A regular hair dryer is used to dry the samples without any ethanol stain. After all these steps, the samples are ready for etching.

Initially, all the steps and process parameters for grinding and polishing were taken from Nibhanupudi<sup>[24]</sup>, but some of it was changed according to the results that were being obtained in order to proportionate the best suited surface for optical analysis.

#### 3.10.4) Etching

The etching solution used is composed of 75% (15ml) glacial acetic acid (99.97%) and 25% (5ml) hydrogen peroxide (30% Volume)<sup>[22]</sup> (Figure 48). The etching time duration is 2 seconds (very brief). The etching is stopped by washing the samples with tap water, then rinsed with deionized water and then rinsed using ethanol.

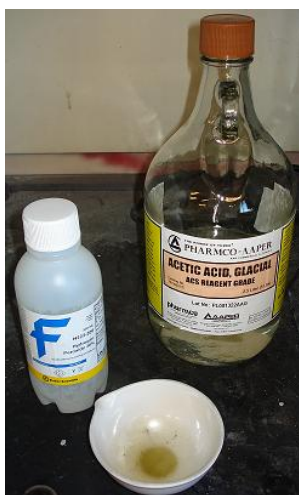


Figure 48 – Acetic Acid and Hydrogen Peroxide used for etching.

### 3.11) Microscope Analysis

Now the samples are ready to be seen in the optical microscope. The microscope used in this task was the Olympus PMG 3 – Inverted metallograph. The magnification was calibrated using a calibration standard, made by Geller MicroAnalytical Lab (Figure 49), before quantitatively analyzing any samples. The samples had their surfaces marked in the very middle (Figure 49) to allow measurements of the 05, 15 and 25mm positions.

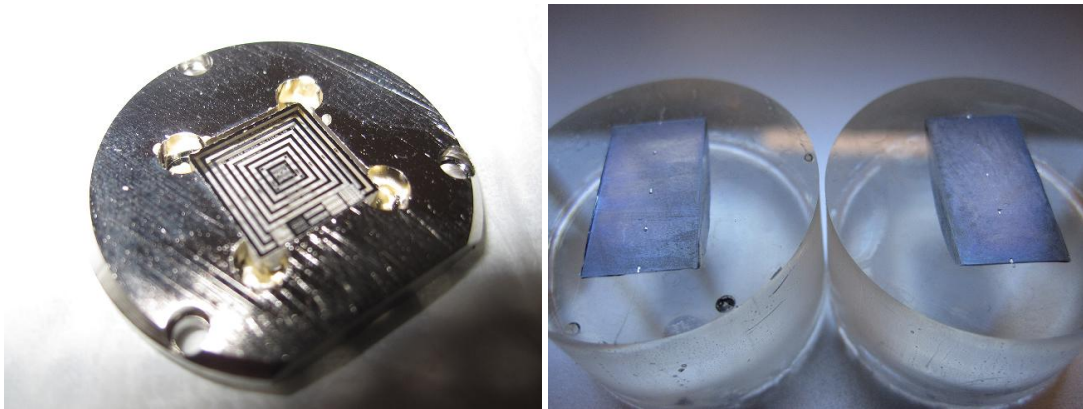


Figure 49 – Calibration Standard and the samples marked on the middle.

### 3.12) Secondary Arm Spacing Measurements

After the calibrated micrographs were obtained, they were analyzed using Scentis quantitative image analysis software. This software has a tool which recognizes and records the middle position of secondary dendrite arms, giving the secondary dendrite arm spacing. The human operator then performs a review of the automated procedure's results and corrects side branch identifications as

needed. The Scentis software procedure to obtain the arm spacing measurements includes the following steps:

- Image preparation – This is when the user changes the contrast, brightness and some other image characteristics in order to obtain a good contrast between the arms and the surrounding (in this case) eutectic matrix.
- Image calibration – This defines how many micrometers a pixel should be representing in the image.
- Arms recognition calibration – This step is to set where the starting and ending point of a certain arm should be, which will be used as a standard for the arms measurements. This is the most important step and will dictate whether the automated arm identification algorithm will be successful in measuring the locations of the arms.
- Line drawing – A line is then draw over the side arms branches (Figure 50) and marks are made wherever the software recognizes an arm based on the previous step calibration. This is also the step where the operator can manually flag the arms spots and correct any errors made by the automated identification of the software.

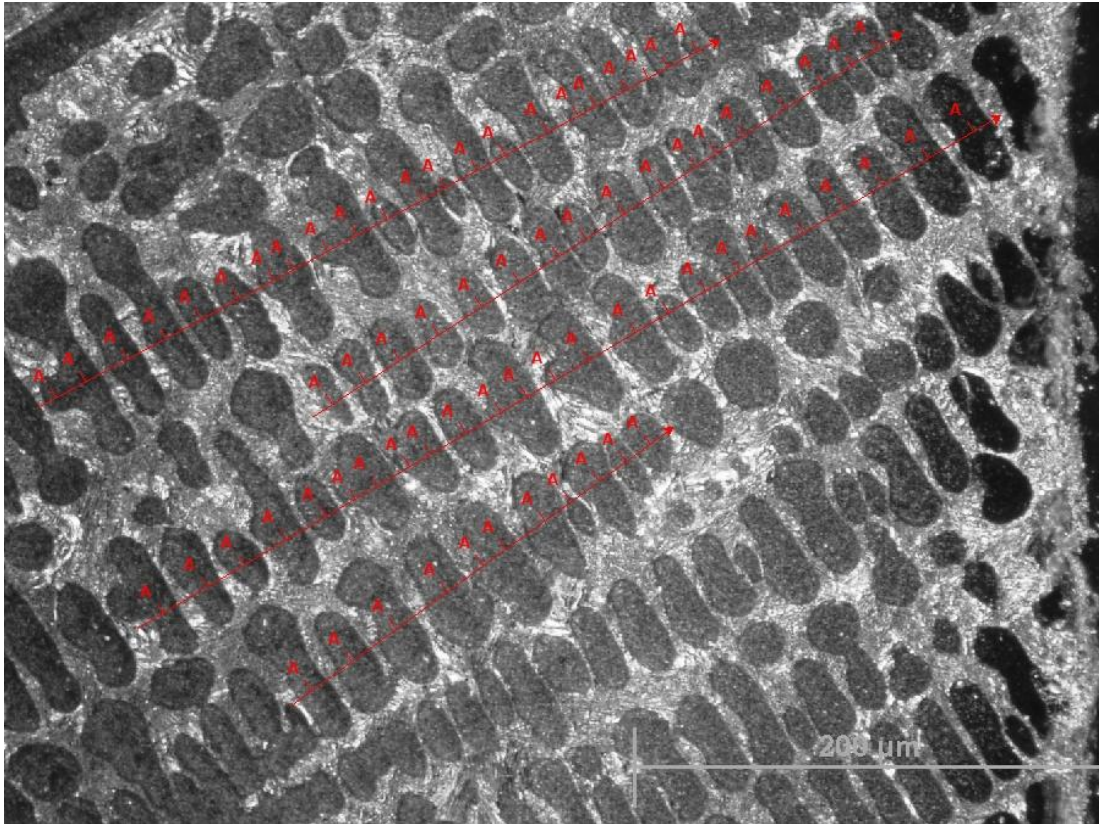


Figure 50 – DAS measurements lines draw using the Scenitis software showing the marked arms.

Measurement and Spreadsheet Generation – This is the final step. The software tabulates the data and computes the average space between the arms and, upon request, generates a spreadsheet containing all the meaningful information about the obtained results (refer to appendix C for a more in depth analysis of the software accuracy). Some of this information includes: measured arm spacing mean; standard deviation of the measurements; maximum and minimum values and the number of arms measured. Then, all these data are saved and used for

later graph construction and analysis. The next chapter will address these results in a more detailed manner.

## 4) RESULTS AND DISCUSSION

### 4.1) Local Solidification Time

The first measurements that were made were related to the local solidification time for each position, located, 5mm apart from each other, measured from the chill plate, extending out to the 35mm position. Later, the 6 thermocouples bundle (described earlier) was used for measurements extending to the 60mm position. Figure 51 shows a graph of the temperature as a function of time obtained for a certain position. To obtain the value that better describe the solidification time (when the temperature reaches 280°C), linear interpolation was used.

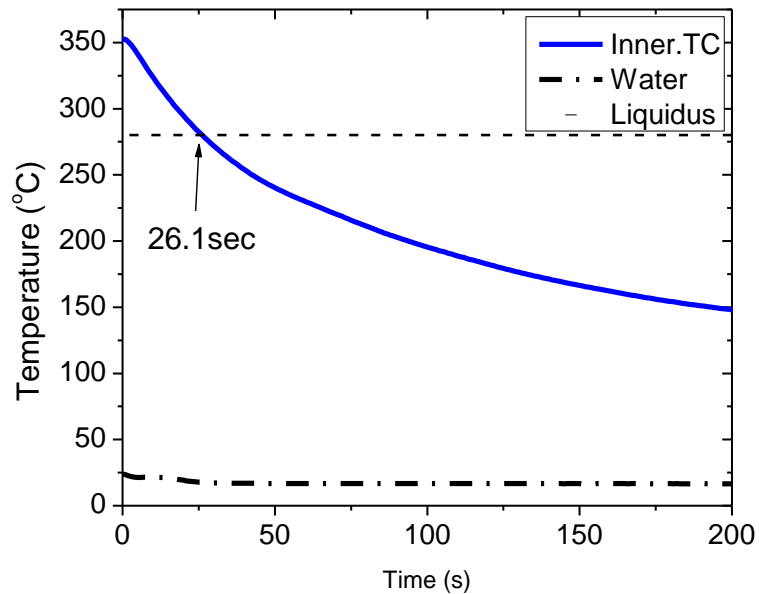


Figure 51 – Graph showing the solidification time (time for the temperature to cool to the liquidus temperature) for the 10mm position.

Different cooling water flow rates, cooling water temperature and the initial inside mold temperature gradients were used in this study. To explain the analysis behind the solidification time calculations, an example experimental setup will be considered here. This configuration comprises of a 1.3GPM water flow rate, at ambient temperature (15 - 20°C) and the bottom and top ceramic heater temperatures (thermocouple holes 01 and 10 – counting from bottom to top) were set to 327 and 290°C, respectively. Several measurements were made, for each position, in order to obtain an average temperature. These values are listed on table 7.

Table 7 – Solidification time (time to cool to liquidus temperature) for each inside mold position example setup.

Position (mm)	00	05	10	15	20	25	30	35
	1.8	5.5	21	39.2	73.8	96.4	151.6	174.6
	2.3	6.8	19.1	49.5	83.5	113.3	159.5	194.3
	1.2	7.1	20.6	49.1	86.4	112.9	160.1	208.3
Time (s)	1.6	7.5	21.6	53.4	84.8	123.3	167.7	208.1
	1.5	8.7	26.1	50.3	78.3			
	1.6		24.5	54.9	78.9			
	1.9				70.2			
	1.7							
Average (s)	1.7	7.12	22.15	49.40	79.41	111.48	159.73	196.33
Shifted Time =Zero (s)	0.0	5.42	20.45	47.7	77.71	109.78	158.03	194.63

For the data in the table, a mean time to reach the liquidus temperature at each position was obtained. In order to make the position 00mm the time zero

position, 1.70 seconds was subtracted from all average time values. After that, an inverted plot of the solid-liquid (S/L) interface position as a function of time was generated (Figure 52). The standard error of the mean (SEM), which definition will be given in section 4.3, was used for the time (horizontal axis) error bars. As can be seen, the graph shape is similar to a square root function, which will help on the next analysis.

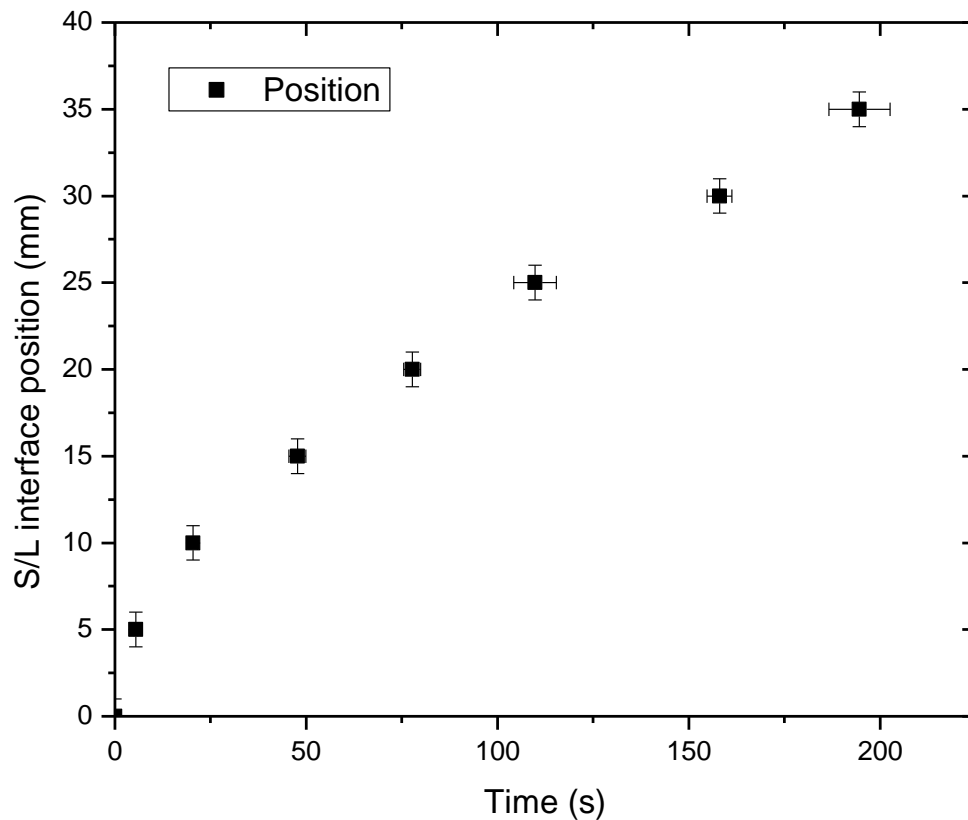


Figure 52 – Graph of the solid-liquid interface position as a function of time. The time values were shifted to the origin.

#### 4.2) Liquidus Velocity (Solid-Liquid Interface Velocity)

A plot of the liquidus position as a function of the square root of time (the expected scaling relationship) was then generated (Figure 53) with uncertainty bars included.

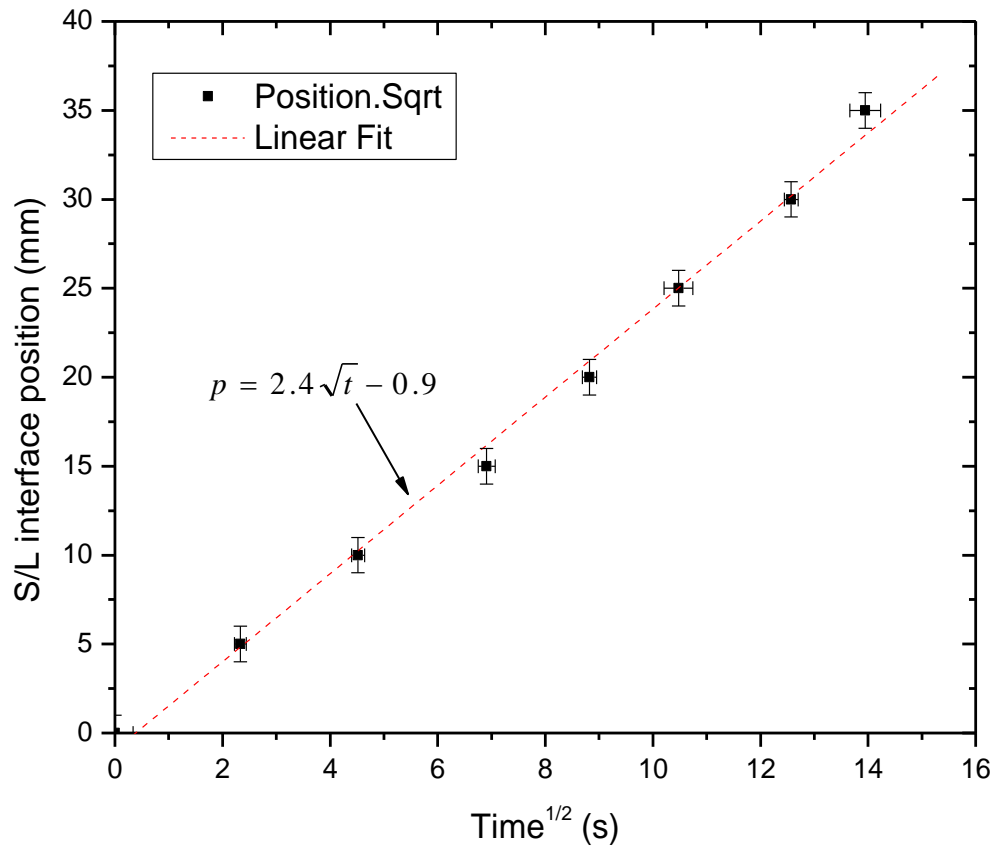


Figure 53 – Graph of the position as a function of the square root of time. The expected linear form was observed.

This graph can be described as a straight line, permitting regression to estimate the numerical coefficients. In this case, the obtained equation was:

$$p = 2.4\sqrt{t} - 0.9, \quad (7)$$

where  $p$  is the liquidus position (relative to the chill plate) and  $t$  is the time. The uncertainties result from the variations observed on replication of the solidification time measurements. The uncertainty (minimum and maximum) values were obtained as following: to find the minimum value for a certain position, its standard deviation value ( $\sigma$ ) obtained from the previous measurements was subtracted from that position mean value and the result had its square root taken. For example, for position 05 mm, the minimum value of the time axis for the position vs. square root of time graph was  $\sqrt{5.42 - 0.52} = 2.21$ .

When calculating the maximum value,  $\sigma$  was added to the mean, instead.

Now, minimum and maximum values for the position when the position is plotted as a function of  $t^{1/2}$  are known and were used as the minimum and maximum for the following analysis.

Taking the first derivative of equation (7), with respect to  $t$ , we are able to obtain an expression for the liquidus velocity

$$\frac{dp}{dt} = \frac{1.2}{\sqrt{t}} \quad (8)$$

Thus, by inserting the values of time obtained for each position into the liquidus velocity equation, we can obtain the liquidus velocity at each position,

which is used to plot a graph containing the  $\lambda_2$  obtained values (not shown yet) as a function of the liquidus velocity. This graph will be shown in the next topic.

#### **4.3) Secondary Dendritic Arm Spacing - SDAS ( $\lambda_2$ )**

Two samples were cast under the same conditions as the previous analysis. After the metallographic sample preparation was done, the samples were etched and taken to microscope analysis. Figure 54 shows micrographs taken from sample 01 (no pressure) for all positions.

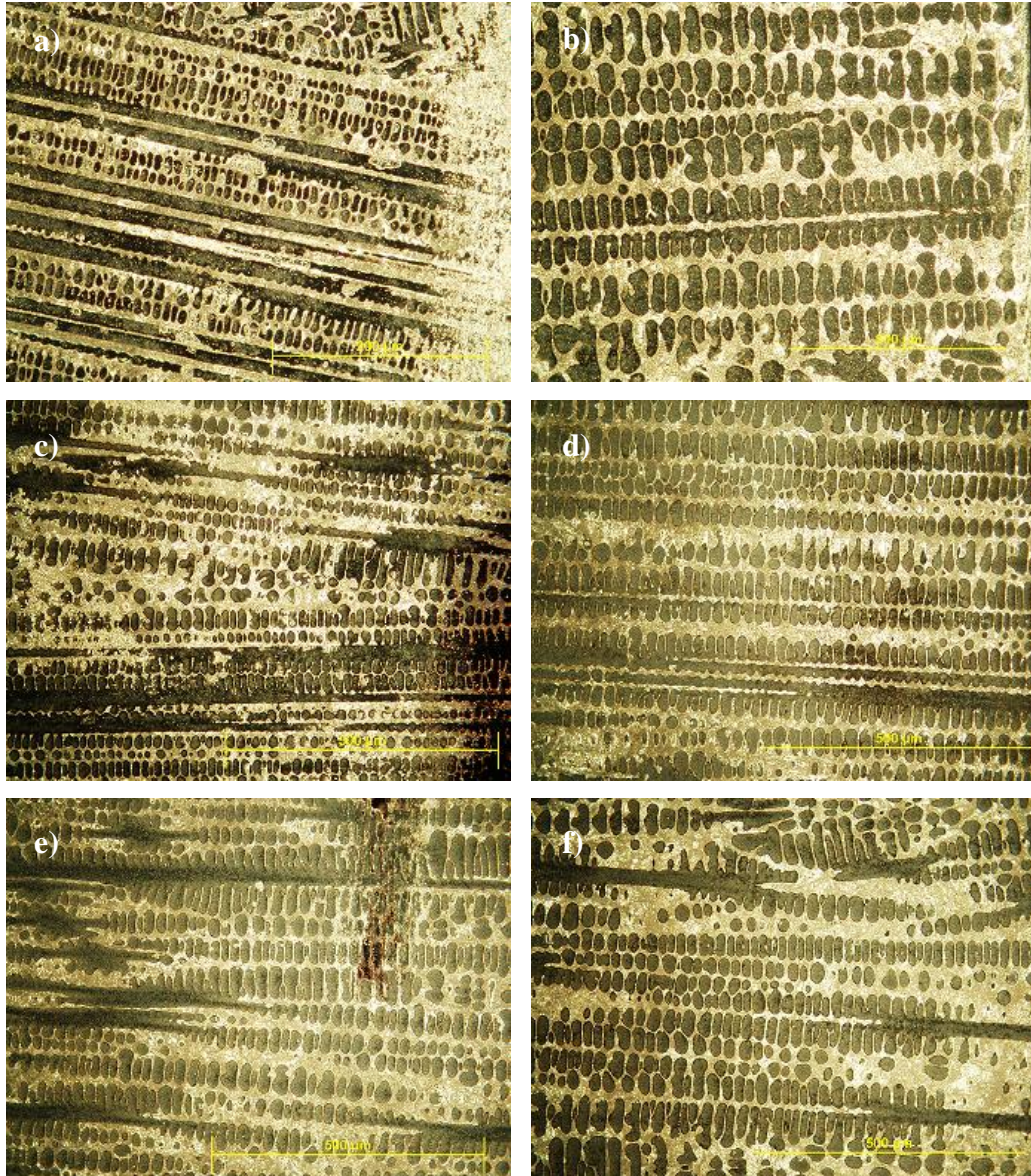


Figure 54 – Micrographs taken from sample 01 a) 05mm position at 40x magnification; b) 10mm position at 40x magnification; c) 15mm position at 20x magnification; d) 20mm position at 20x magnification; e) 25mm position at 20x magnification and; 30mm position at 20x magnification.

After obtaining all the necessary  $\lambda_2$  values, a table was generated (Table 8).

Table 8 – Measured values of  $\lambda_2$  (mean) and their standard deviation ( $\sigma$ ) for samples 01 and 02 (no pressure) for all positions.

Position (mm)	$\lambda_2$ Sample 01 ( $\mu\text{m}$ )		$\lambda_2$ Sample 02 ( $\mu\text{m}$ )	
	Mean	$\sigma$	Mean	$\sigma$
05	7.762	1.543	8.289	1.713
10	13.093	2.849	13.171	2.661
15	15.55	3.269	15.813	3.457
20	18.015	4.027	17.889	3.912
25	19.108	4.108	19.375	4.593
30	19.845	4.345	20.016	4.424

The mean (average), which is mathematically described in equation 9, is the sum of all measured values divided by the number of measurements realized.

$$\bar{x} = \frac{1}{n} * \sum_{i=1}^n x_i, \quad (9)$$

where  $\bar{x}$  is the arithmetic mean (mean) and  $n$  is the number of values obtained. The standard deviation  $\sigma$  (Equation 10) was used to represent the amount of spread contained in the measured values.

$$\sigma = \sqrt{\frac{1}{n} \sum_{i=1}^n (x_i - \bar{x})^2}, \quad (10)$$

Another statistical value used was the SEM (mentioned in section 4.1). Differently than the standard deviation, this value represents the uncertainty

contained on the value of the average of a group of measurements relative to the true mean (real average). The SEM formula is:

$$SEM = \frac{\sigma}{\sqrt{n}} \quad (11)$$

Once all the SEM values for the  $\lambda_2$  measurements had the same order of magnitude as the data symbols size, therefore being hidden by the later, the values used for the error bars of all  $\lambda_2$  graph representations were the standard deviation. A plot of the measured  $\lambda_2$ , showing variation as a function of position is presented in Figure 55 and Figure 56 shows how  $\sigma$  also varied as a function of position, for these two samples.

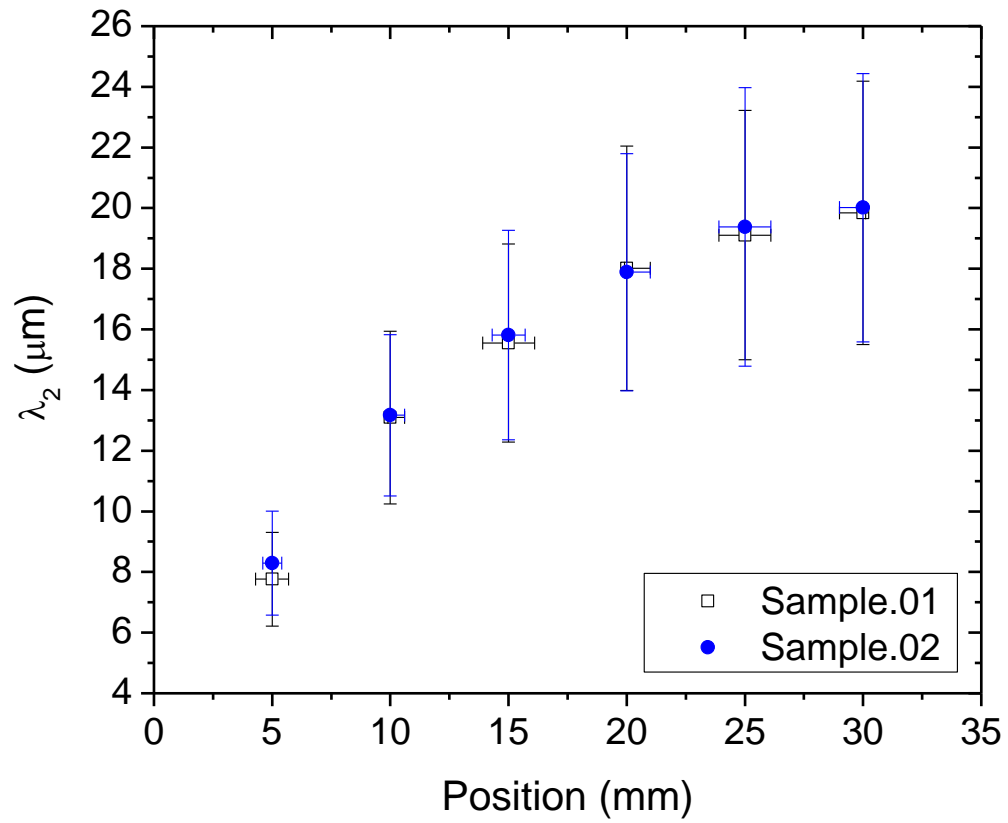


Figure 55 –  $\lambda_2$  as a function of position showing a small difference between the samples values.

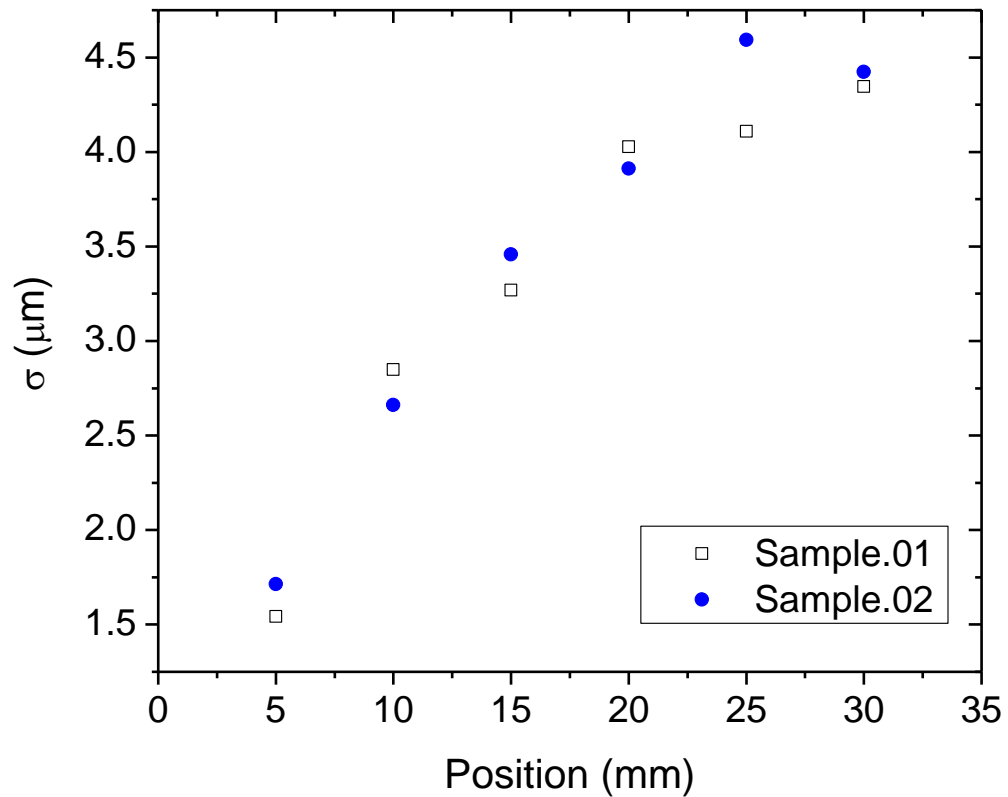


Figure 56 – Standard deviation ( $\sigma$ ) as a function of position. The values also agree with each other.

As can be seen from the graph on Figure 55, the  $\lambda_2$  values were almost identical for both samples, demonstrating the experiments are repeatable. Figure 56 shows that, besides the value for the 25mm position, all the  $\sigma$  values also were close to each other. Both curves have alike shapes. A graph of the dependency of the liquid velocity on  $\lambda_2$  values is presented in Figure 57.

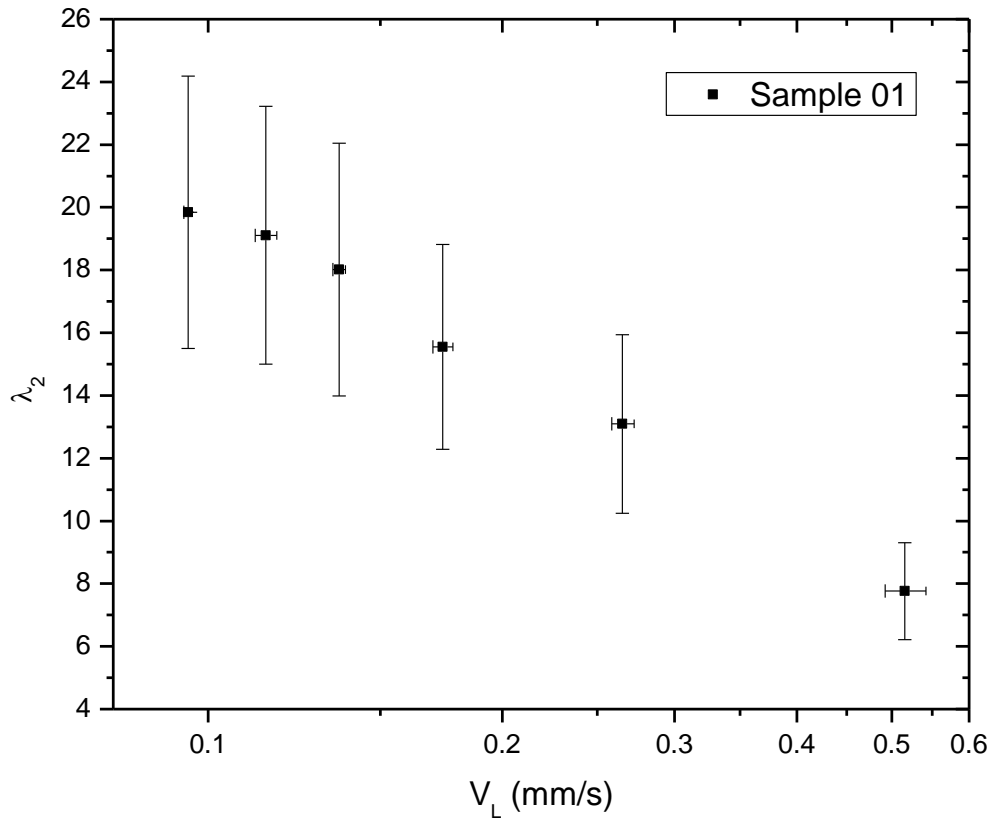


Figure 57 –  $\lambda_2$  as a function of the Liquidus velocity. As  $V_L$  values increase,  $\lambda_2$  values decrease.

We can see that as the liquidus velocity increases,  $\lambda_2$  values decrease. This behavior was also found by Rosa et al.<sup>[16]</sup> when realizing solidification experiments with Pb-Sb alloys with varied Sb concentrations (2.5, 3.0 and 6.6wt%Sb). Figure 58 shows that the behavior mentioned above happens independently from the solute (Sb) concentration.

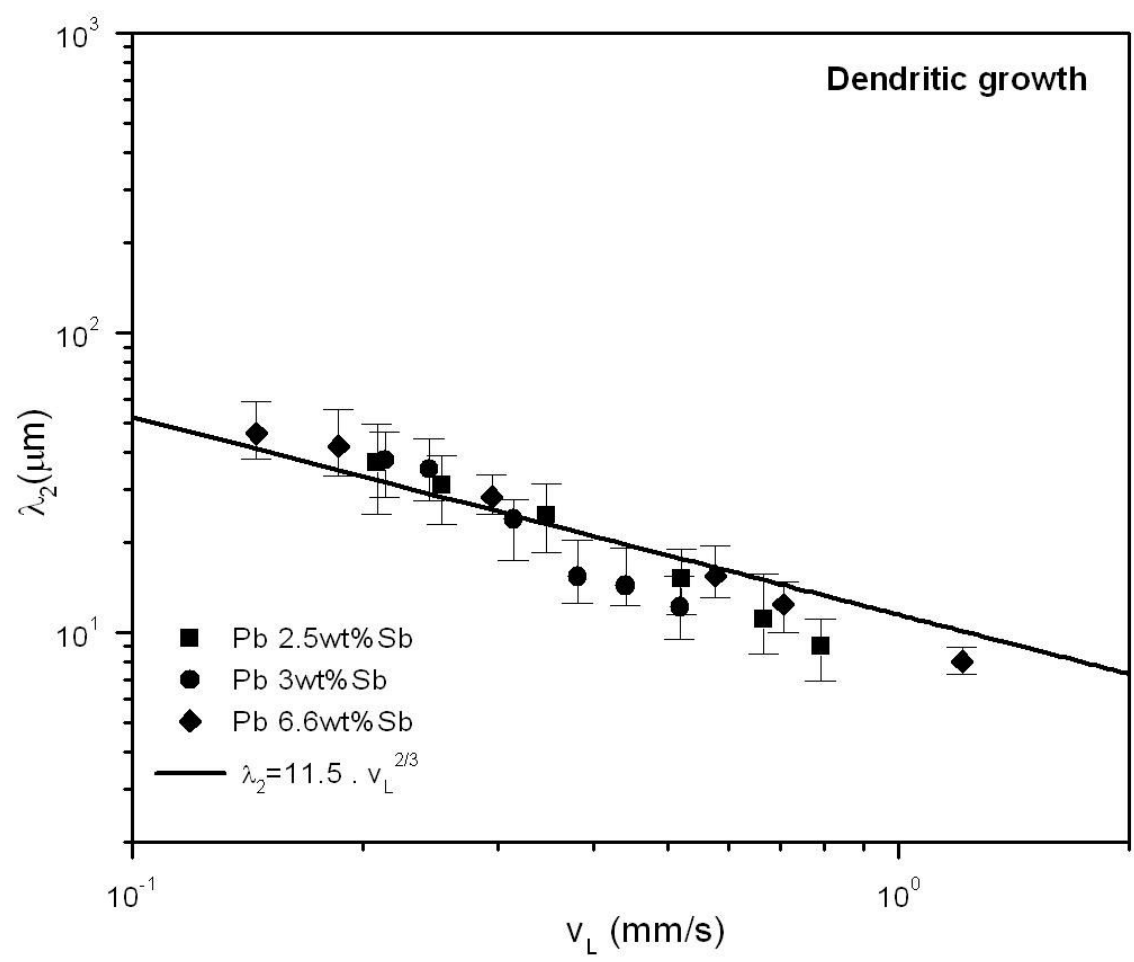


Figure 58 –  $\lambda_2$  values as a function of  $V_L$  for Pb-Sb alloys with varying concentrations. Notice how  $\lambda_2$  decreases as  $V_L$  increases for all curves despite the amount of Sb.<sup>[16]</sup>

From Figure 57 data, it was also possible to calculate the natural frequency of creation of the secondary arms, obtained by dividing the local solidification velocity ( $V_L$ ) by local  $\lambda_2$ . A graph of how this frequency varies with respect to position is shown on Figure 59. These formation frequencies (Table 9), which resulted from a conventional directional solidification process (no pressure)

served as our basis for selecting the forcing frequency of the pressure during subsequent applied pressure solidification experiments.

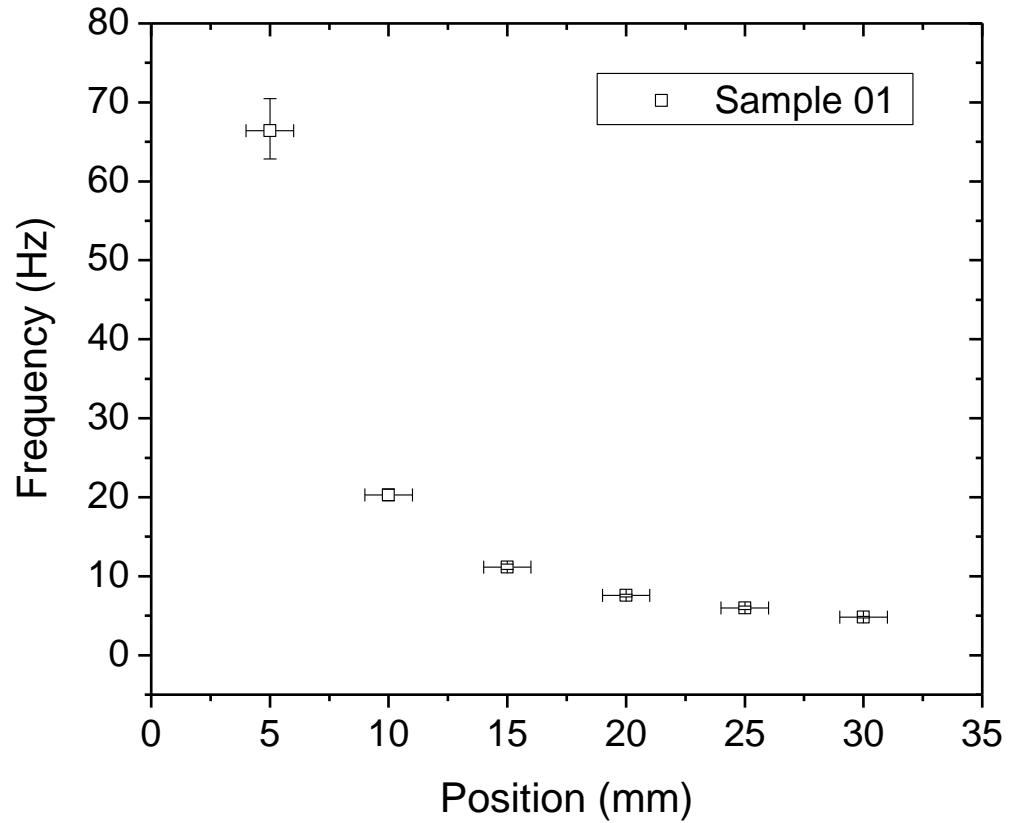


Figure 59 – Frequency of formation of  $\lambda_2$  as a function of position. Note how the natural formation frequency decreases as the position increases.

Table 9 –  $\lambda_2$  formation frequency values at different positions obtained for samples 01 and 02.

Position	Frequency of formation (Hz)	
	Sample 01	Sample 02
05	66.4	62.2
10	20.3	20.1
15	11.20	11.0
20	7.6	7.6
25	6.0	5.9
30	4.8	4.8

Examination of the data shows that when no pressure is applied to the melt during directional solidification of this alloy, the side arm formation frequency decreases with the distance from the chill plate. I.e., the formation frequency decreases as the liquidus velocity decreases.

#### 4.4) Pressure Applied Solidification Experiments

The next set of experiments performed were the solidification of the alloy while applying pulses of pressure. The first pulse frequency to be used was 7.4Hz (approximately the frequency of formation of the arms at the 20mm position – Table 9).

Figures 60 and 61 show graphs of the applied compressive force (on the piston) as a function of time (at two time scales). The programmed load was varied from -10 to -110lbf at a frequency of 7.4Hz - although it can be seen in Figure 60 and 61 that the upper limit was approximately -20lbf due to restrictions

imposed by the machine capabilities once the rapid cycling of the hydraulic system at 7.4Hz prevented the load from reaching the set point. The accuracy of this was found to be dependent on the configuration of the feedback-control system (PID control) used for the MTS. The most important parameter was the proportional one, which would start with a value around 9 (beginning of the experiment) and as the temperature dropped (as the solidification process developed), its value would fall to around 3.

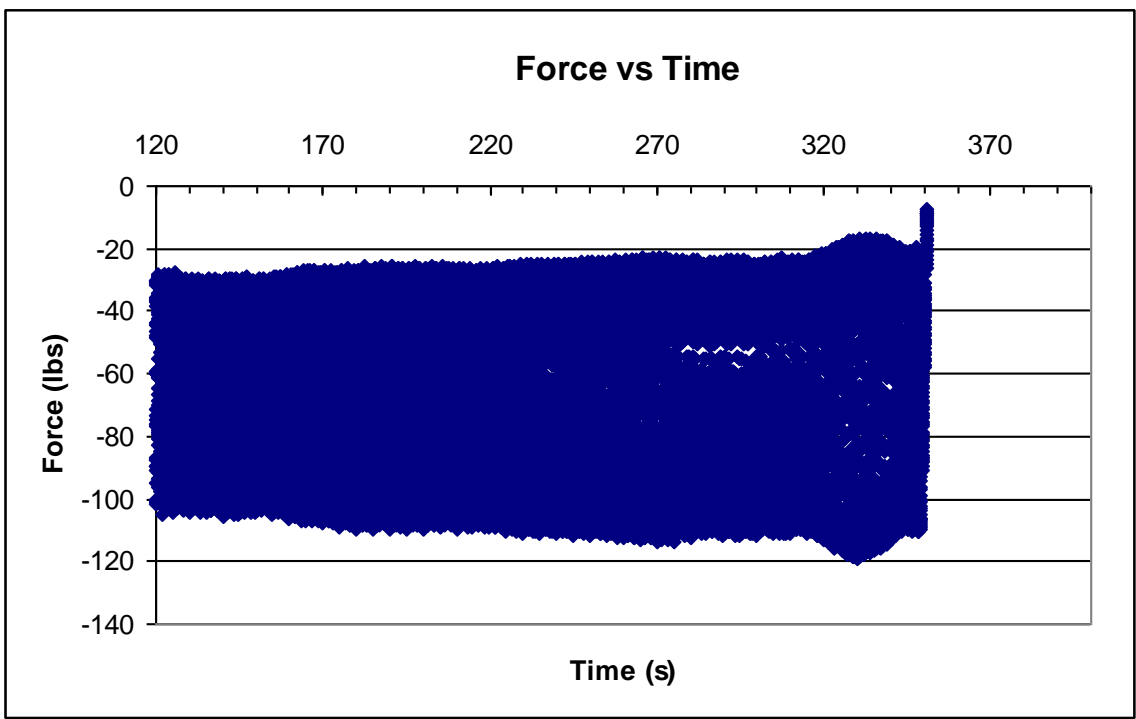


Figure 60 – Graph showing the applied force as a function of time for the whole experiment duration of the -110lbf maximum load.

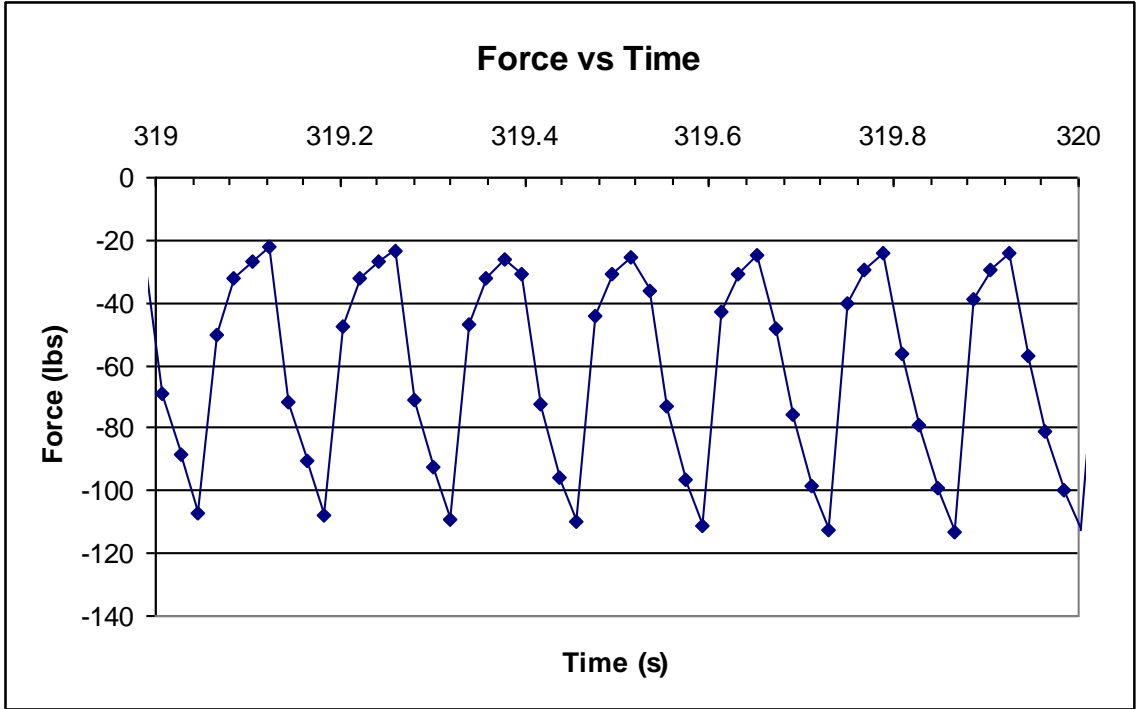


Figure 61 – Graph showing a section of the graph on Figure 60 correspondent to one second.

Similarly, Figures 62 and 63 show graphs of the applied compressive force for a load varied from -10 to -310lbf at a frequency of 7.4Hz – where again; the upper limit was approximately -50lbf.

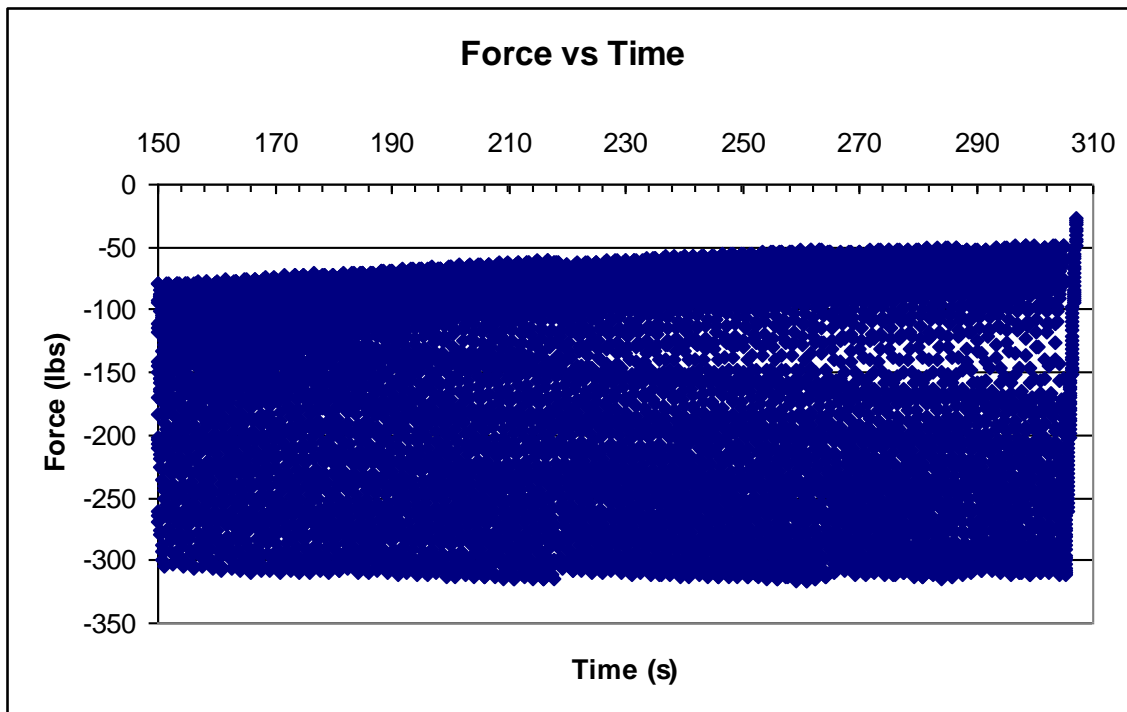


Figure 62 – Graph showing the applied force as a function of time for the whole experiment duration of the -310lbf maximum load.

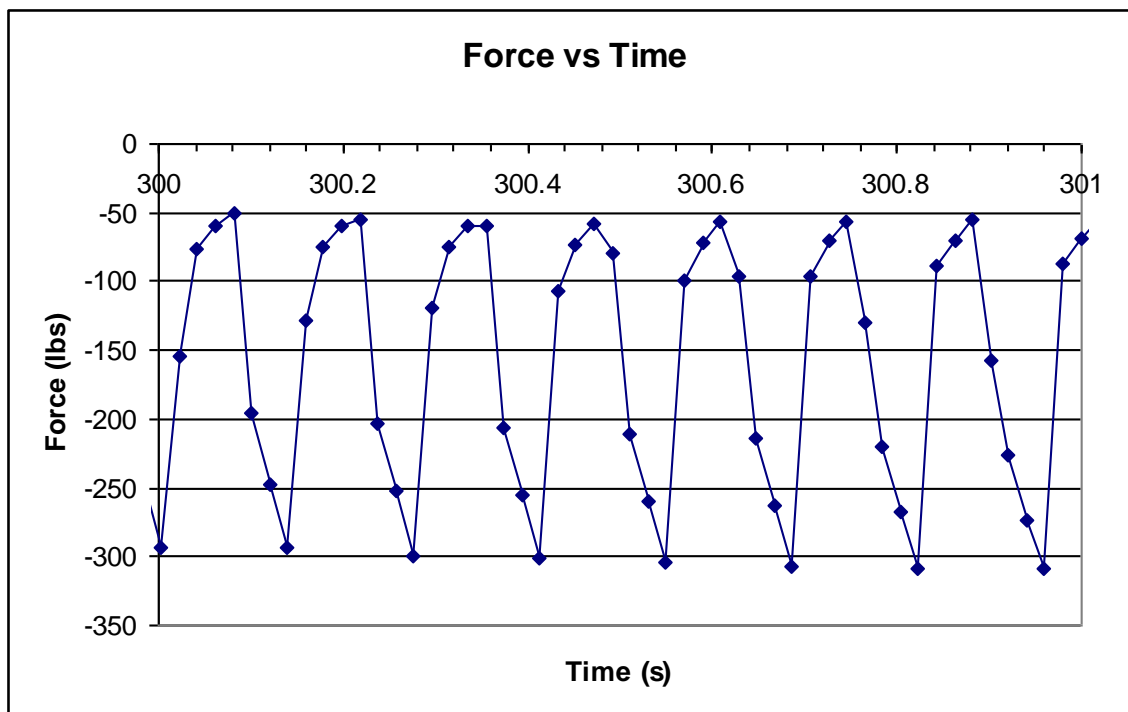


Figure 63 – Graph showing a section of the graph on Figure 62 correspondent to one second.

Using the piston cross-sectional area to convert the applied force to the melt, the pressure range obtained is -266.3 to -48.4psi for the data in Figures 60 & 61, and -750.6 to -121.1psi for the data of Figures 62 & 63. These give pressure ranges values ( $\Delta P$ ) of 217.9psi (1.5MPa) and 629.5psi (4.3MPa) for each of these respectively. When these pressure ranges (changes) are inserted into the Clapeyron equation, the estimate changes in the melting temperature for each of these experiments are found to be 0.12 and 0.35K respectively (for the -110 and -310lbf experiments).

Figure 64 shows how the displacement varies with respect to time for the 110lbf experiment. As can be seen, the piston starts out at a certain position and

stays at it until the solidification process is initiated. Once the water flow is open, the piston starts to drop. This is due to a combination of factors; the decrease of air pressure between the piston and the sample as the temperature inside the mold decreases, the change in volume during the solidification process and thermal contraction. This graph was mainly used to prove that the pressure was being applied on the sample (the piston was not stuck).

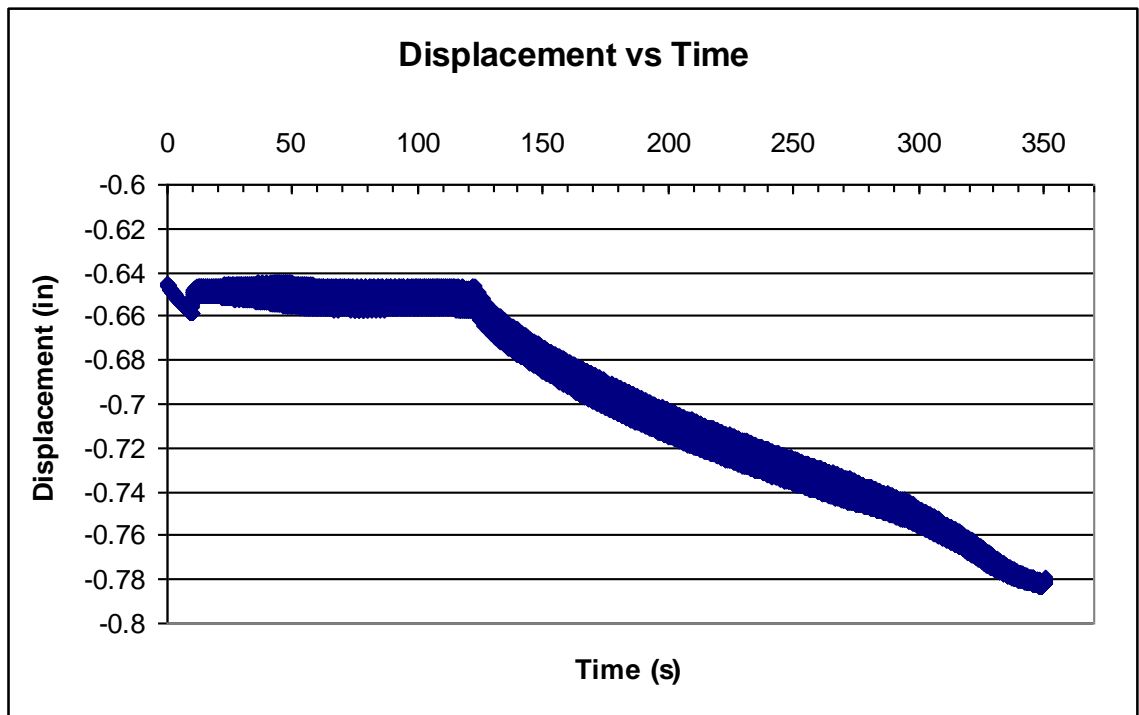


Figure 64 – Graph showing how the displacement varied as a function of the position.

#### 4.5) Secondary Dendrite Arm Spacing ( $\lambda_2$ ) Analysis

Figure 65 shows a plot of measured  $\lambda_2$  as a function of position for the two experiments conducted with applied pressure pulses (-110 and -310lbf) as well as experiments conducted without any pressure (the first two samples presented

at the beginning of this chapter). It is noted that the oscillating pressure had an impact on the  $\lambda_2$  values, decreasing them as expected. However, comparison of the -110 and -310 lbf data shows a much smaller difference than seen between the unpressurized and pressurized data (taken together). A noticeable difference between the two pressurized cases appears at positions around 20mm, which is in the approximate location at which the side arm formation frequency was matched by the pressure oscillation forcing frequency of 7.4Hz. This was the first evidence supporting the existence of a form of resonance between the natural side arm formation frequency and the applied forcing frequency of the pressure oscillations.

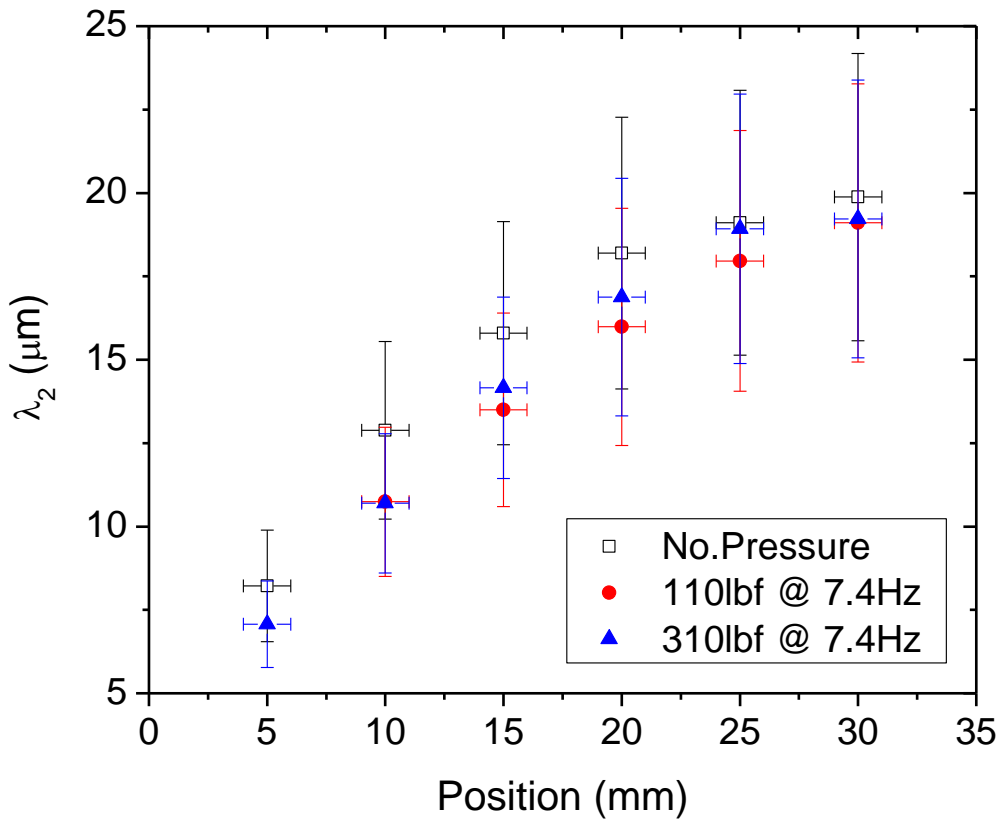


Figure 65 – Graph showing the variation of the secondary DAS as a function of position for the samples without pressure and 110 and 310lbs at 7.4Hz.  $\lambda_2$  values are smaller for the samples solidified under pressure influence.

Figure 66 shows how the  $\sigma$  values varied as a function of positions for the previous samples.

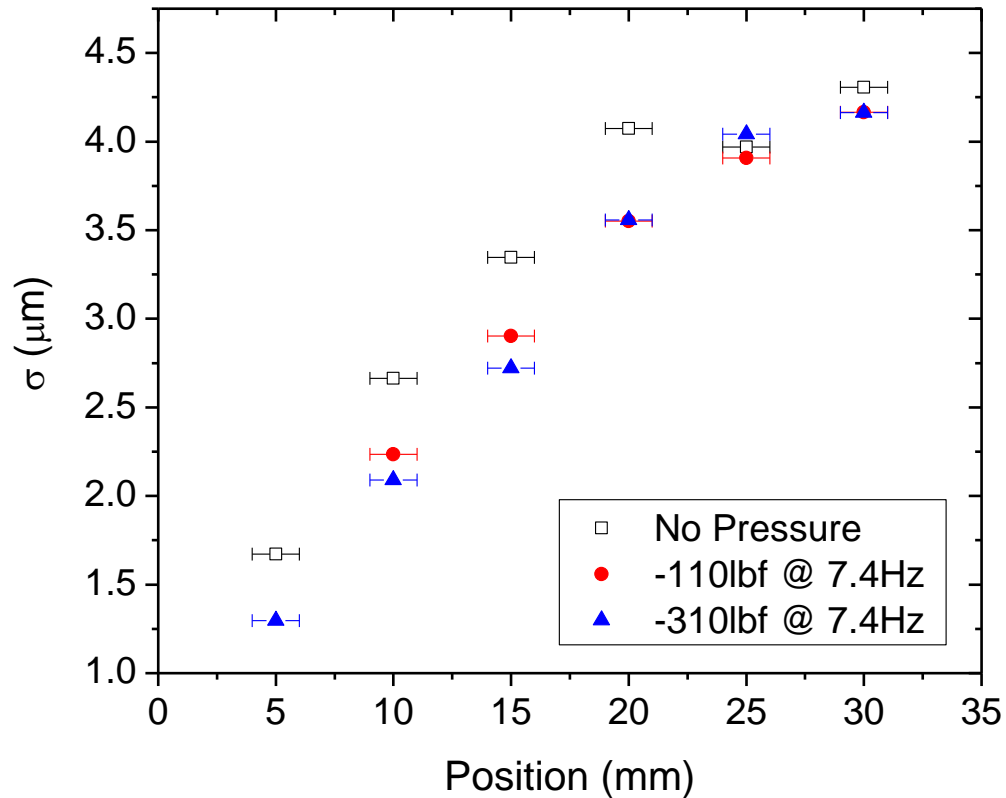


Figure 66 – Graph showing the variation of the  $\sigma$  values as a function of position for the samples without pressure and -110 and -310lbs at 7.4Hz. These values also decreased for the samples where pressure was applied.

In order to further investigate how the pressurization frequency influences the side arm generating process, a sample was tested using maximum applied load of -310lbf and a 5.9Hz pressurization frequency (contrasting with the 7.4Hz frequency used for the data presented in Figures 62 & 63). The 5.9Hz frequency is calculated (using the Figure 59) to match the side arm formation frequency at

the 25mm position. The data obtained from this new experiment, are compared with no pressure and the -310lbf at 7.4Hz experiments (Figure 67).

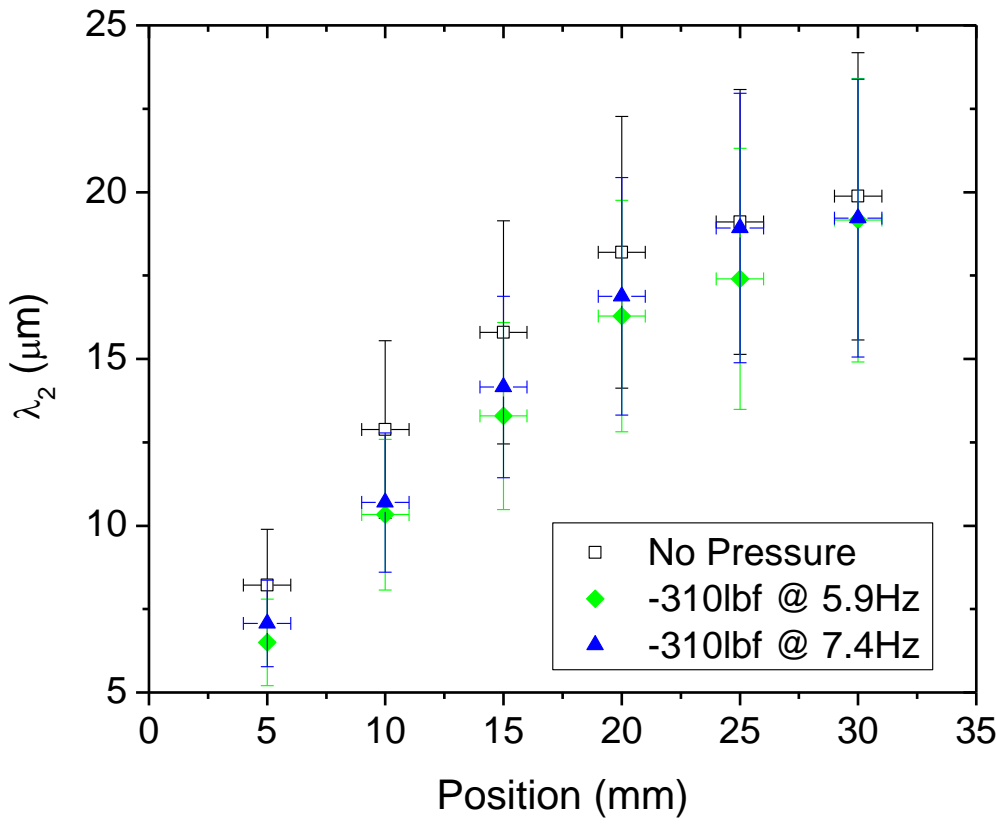


Figure 67 - Graph showing the variation of  $\lambda_2$  as a function of position for the samples without pressure; -310lbf at 5.9Hz and -310lbf at 7.4Hz.

Again, the oscillating pressure decreased the  $\lambda_2$  values of the pressure applied samples when compared to the no-pressure ones. Figure 67 also shows that, besides position 30mm, all the  $\lambda_2$  values for the samples solidified under the 5.9Hz frequency were smaller than the ones solidified under 7.4Hz, although that

difference was considered statistically negligible. Figure 68 shows the standard deviation calculated for these samples.

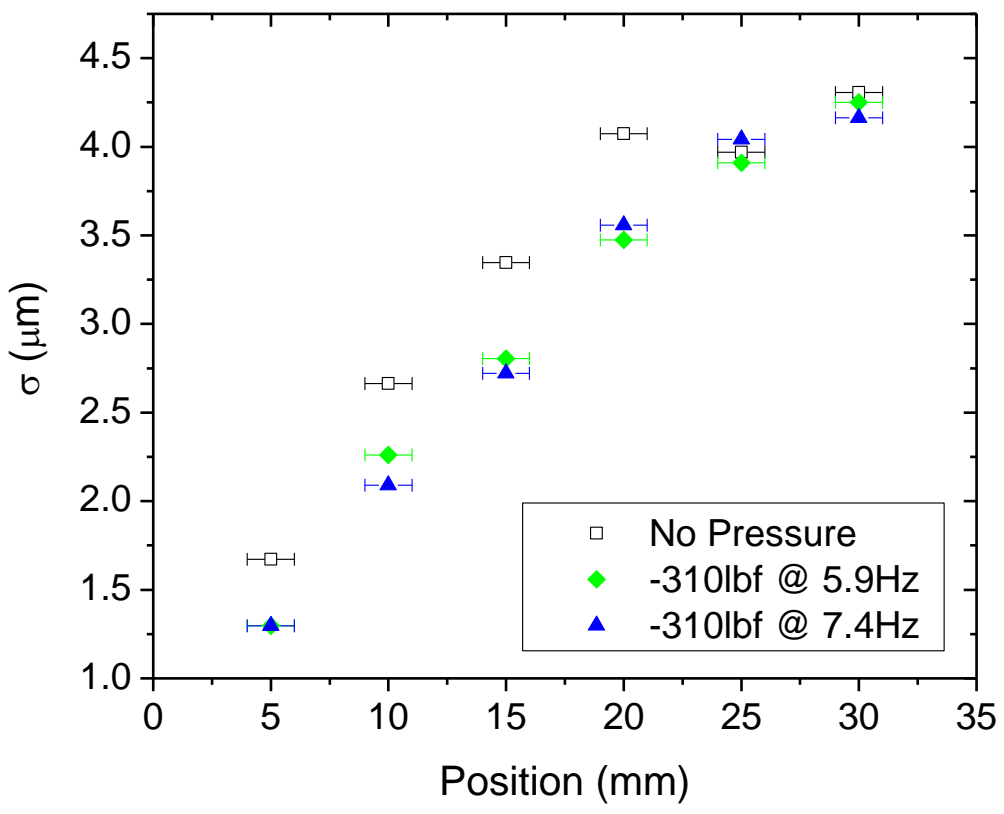


Figure 68 - Graph showing the variation of  $\sigma$  as a function of position for the samples without pressure; -310lbf at 5.9Hz and -310lbf at 7.4Hz. One more time the  $\sigma$  values decreased for the pressure applied samples.

To clarify whether the pressure pulses applied during the solidification process were responsible for the  $\lambda_2$  changes, a sample was cast under constant pressure, (no cyclic piston motion) to see if the change in  $\lambda_2$  could be explained through the conventional mechanism of altering the metal-mold interface thermal

conductivity. The load used in this case was -310lbf. The results for this experiment were compared with the other three cases: no pressure; -310lbf at 7.4Hz; and the -310lbf at 5.9Hz samples. The results are shown in the following graph (Figure 69).

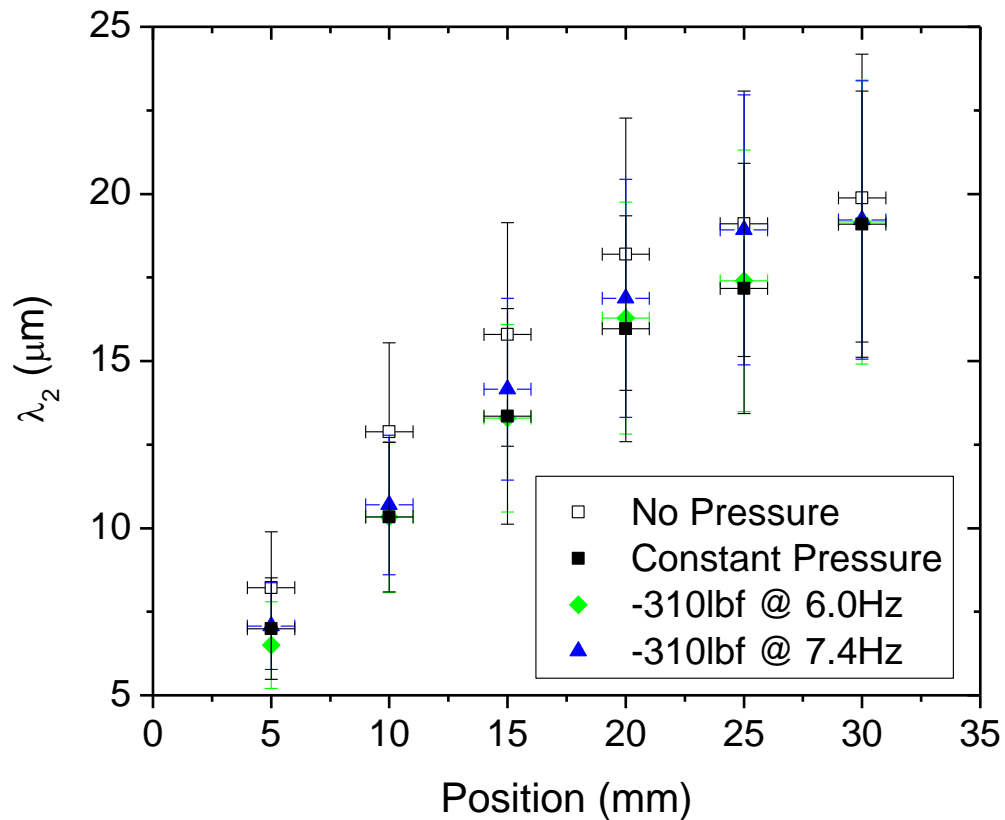


Figure 69 - Graph showing the variation of  $\lambda_2$  as a function of position for the samples without pressure; -310lbf at 5.9Hz; -310lbf at 7.4Hz and -310lbf at constant pressure.

Analysis of this plot strongly suggests that cyclic nature of the pressure was not responsible for the changes in the secondary DAS. I.e, in Figure 69, the three data sets obtained under varying pressurization conditions are nearly

indistinguishable from each other in comparison to the no-pressure case. This observation could have a couple of explanations. The first one being that the frequency that is being used may be insufficiently match to the natural frequency of the side branch formation. For example, if the frequencies were too high, it may be “seen” as if it was constant, leading to results similar to the ones obtained under constant pressure. A second potential cause could be that the amount (magnitude) of pressure being applied to the molten metal is not sufficient to increase the melting point enough to cause a system perturbation capable of stimulating a resonance in generating the secondary arms. Figure 70 shows standard deviation as a function of position graph, including the values for the constant pressure sample.

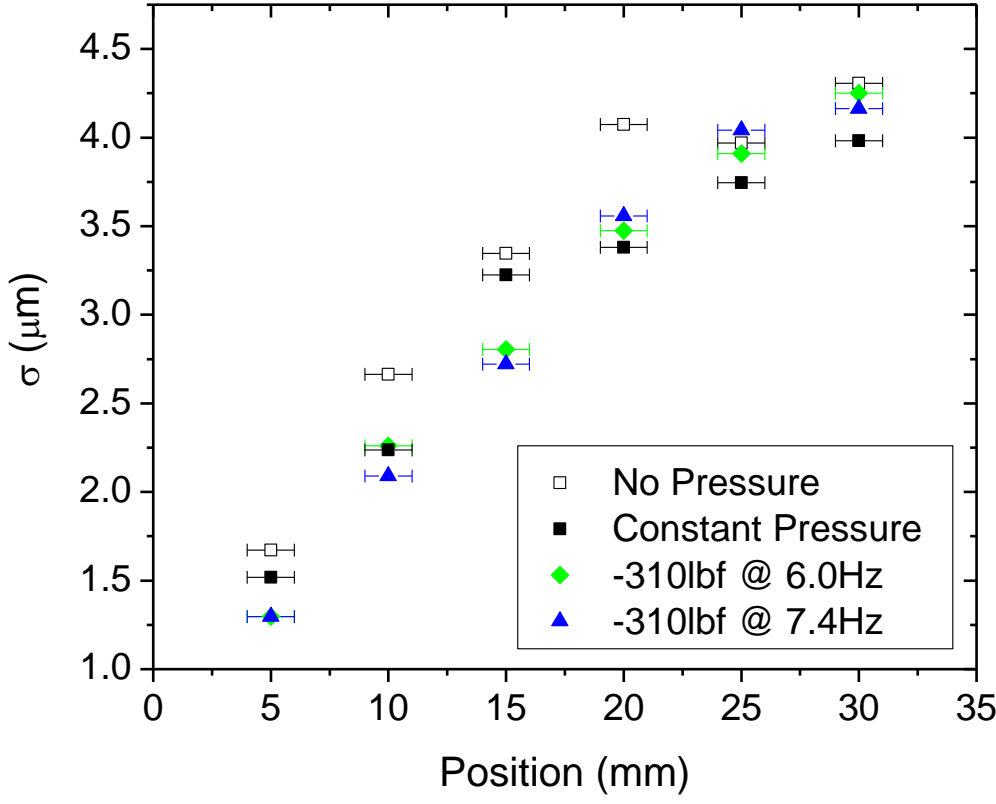


Figure 70 - Graph showing the variation of  $\sigma$  as a function of position for the samples without pressure; -310lbf at 5.9Hz; -310lbf at 7.4Hz and -310lbf at constant pressure.

A new set of experiments was then made to examine the second of these hypothesis. The idea was to increase the amount of applied pressure so the melting point would experience a greater change (increase). Equipment difficulties were unfortunately experienced when higher load levels were applied at high temperatures (testing the strength of our o-rings) and at high frequencies (a hardware limitation). After several unsuccessful attempts to reach higher pressures with the same temperature profile (the o-rings were melting and the

molten metal started to leak), it was decided that a change to the inside mold temperature profile was the best way to address this problem. I.e., the mold temperature profile was adjusted to decrease the temperature at the mold locations closest to the o-rings. This change to the temperature profile was achieved through a combination of changes to the experimental hardware. An initial attempt made was to reduce the inside mold temperature to a certain level where the top liquid surface temperature would be around 400°C (value found to be acceptable for the silicon o-rings). The downside of this configuration was that the bottom (chill plate) part of the mold needed to be at a temperature below the alloy's liquidus temperature. I.e., this configuration unfortunately left the bottom part of the mold with some solidified metal *before* the actual experiment had started. In this way, it was possible to apply up to -600lbf but not the whole sample was solidified under its influence. To counter this, a 10mm long piece was cut from the bottom of the sample and the remainder was then analyzed as usual, but with the 00mm position now being shifted 10mm above the chill plate. Another new solidification rate calibration plot had to be generated as a result of the changes to the temperature profile. The results from the analysis of this were not quite satisfactory, thus further development was necessary.

At this point, an important question to be answered was: how could the inside temperature profile, which so far had its highest temperature around the middle region of the mold, be decreased and made more uniform throughout the mold without causing any (other) major change to the experiment design? The answer for this question ended up being comprised of two main modifications to

the thermal properties of the heater: 1) the manner in which the heater coils were stretched, and 2) the addition of a fiber glass insulation layer surrounding the bottom part of the mold. So far, the heater coils had been stretched evenly throughout its extension. After figuring out how long the coil should be to fill the entire inside mold cavities (bottom) and that the middle region had the highest temperature, it was decided that a better approach would be to stretch the coil differently in different areas. The result was that the first (lower) region – from the bottom to the top was stretched 4 times its initial length, the second region 6 times and the third and last region 8 times. This helped decrease the amount of heat generated in the middle region of the mold and concentrated the heat generation more near the bottom. It was found that the top heater did not need to be turned on at all for the top metal surface to remain molten. This further reduced the amount of heat heading to the middle, and reduced the temperature gradient between the top and bottom parts of the mold. Furthermore, in order to minimize the heat dissipation from the bottom to the surroundings, a fiber glass insulation layer was added (Figure 36) yielding satisfactory performance of the system.

With the temperature gradient at acceptable levels (mostly due to the fact that the piston o-rings would melt at high temperatures and that the gradient needed to be altered considerably), the targeted conditions for experiments changed (due to the new, lower solidification rates). I.e., the new operating conditions necessitated emphasizing slower solidification and lower side arm formation frequencies. Earlier studies indicated that slower side arm formation

frequencies were primarily visible farther from the bottom chill plate, and required focusing analysis on that region. New calibration measurements of the temperature for positions extending up to 60mm, starting from the chill plate, were thus obtained - with the aid of the 6 thermocouples bundle.

After analyzing the results (Figure 71), it was noticed that beyond the ~30mm position, the solidification rate graph no longer had the square root of time scaling behavior. Actually, the top part of the mold had its solidification speed increase as the time went by, suggesting that additional extraction of heat occurs from the top of the mold, probably by the surroundings (rather than conducting through the mold chill plate). The limited insulation in that area of the design allows heat to dissipate, causing the position vs. time curve to have an inflection point appear at distances relatively far from the chill plate. It was thus decided that any results beyond the 30mm position could no longer be considered as under directional solidification. This was substantiated by visual inspection of the micrographs, where the alignment of the dendrite arms was seen to diminish beyond this distance.

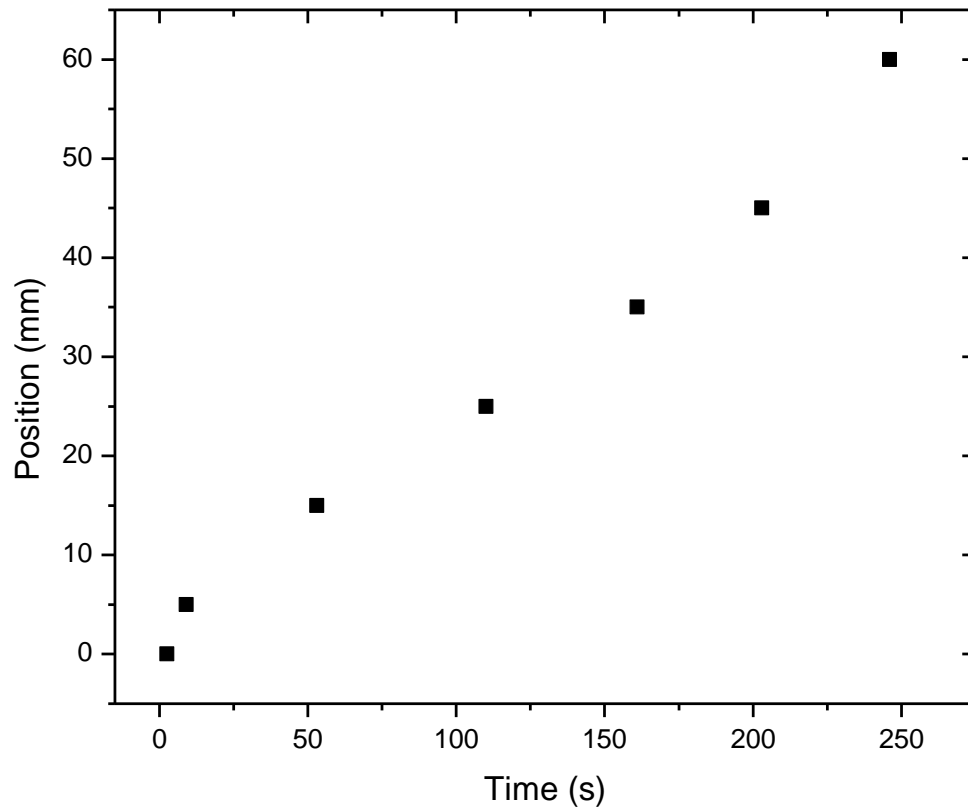


Figure 71 – Graph showing how the liquidus position varied as a function of time for positions between 0 and 60mm. An inflection point occurs at around 140s after the alloy started solidifying.

Because analysis of the top part of the sample (far from the chill plate) revealed itself to be outside the carefully-controlled conditions needed for this research, another approach was then attempted in order to bring the location region of interest (where the resonance was expected to occur) closer to the chill plate end of the system. This required a slower solidification rate, achieved by increasing the water temperature and decreasing its flow rate. The water

temperature was increased to 50°C and the flow reduced to 0.05gpm. As discussed earlier, this was achieved using a fluid circulator. This change yielded a frequency of arm formation of approximately 5.0Hz at the 25mm position. Now, the setup was ready for the experiments to be performed at higher pressures.

The new experiments were conducted at -600lbf with a frequency of 6.0Hz (close to 5.9Hz from the previous experiments). As is seen in Figure 72, the minimum force applied was around -100lbf giving an applied pressure range of 242.1 to 1452.8 psi, or a  $\Delta P$  of 1210.7psi (8.3MPa), which corresponds to a 0.67K increment on the melting temperature.

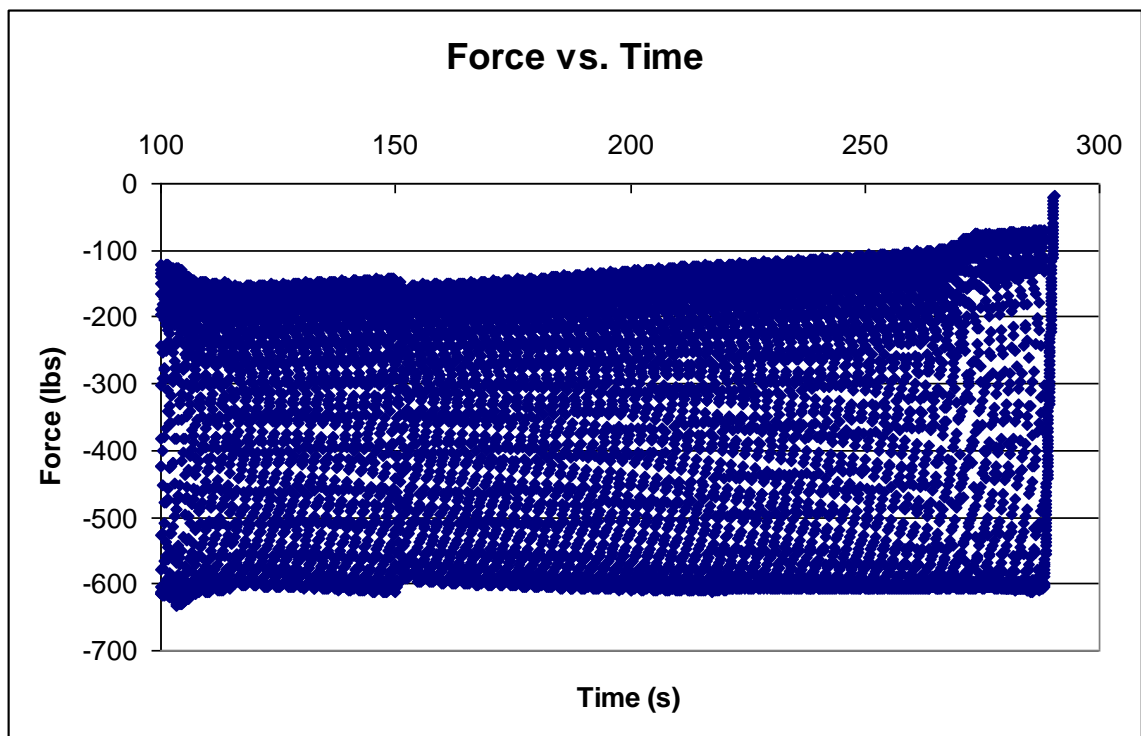


Figure 72 - Graph showing the applied force as a function of time for the whole experiment duration of the -600lbf maximum load at a 6.0Hz frequency.

Figure 73 shows the observed piston displacement as a function of time and from this, it is possible to confirm that the pressure was properly being applied on the metal (i.e., the piston was not stuck).

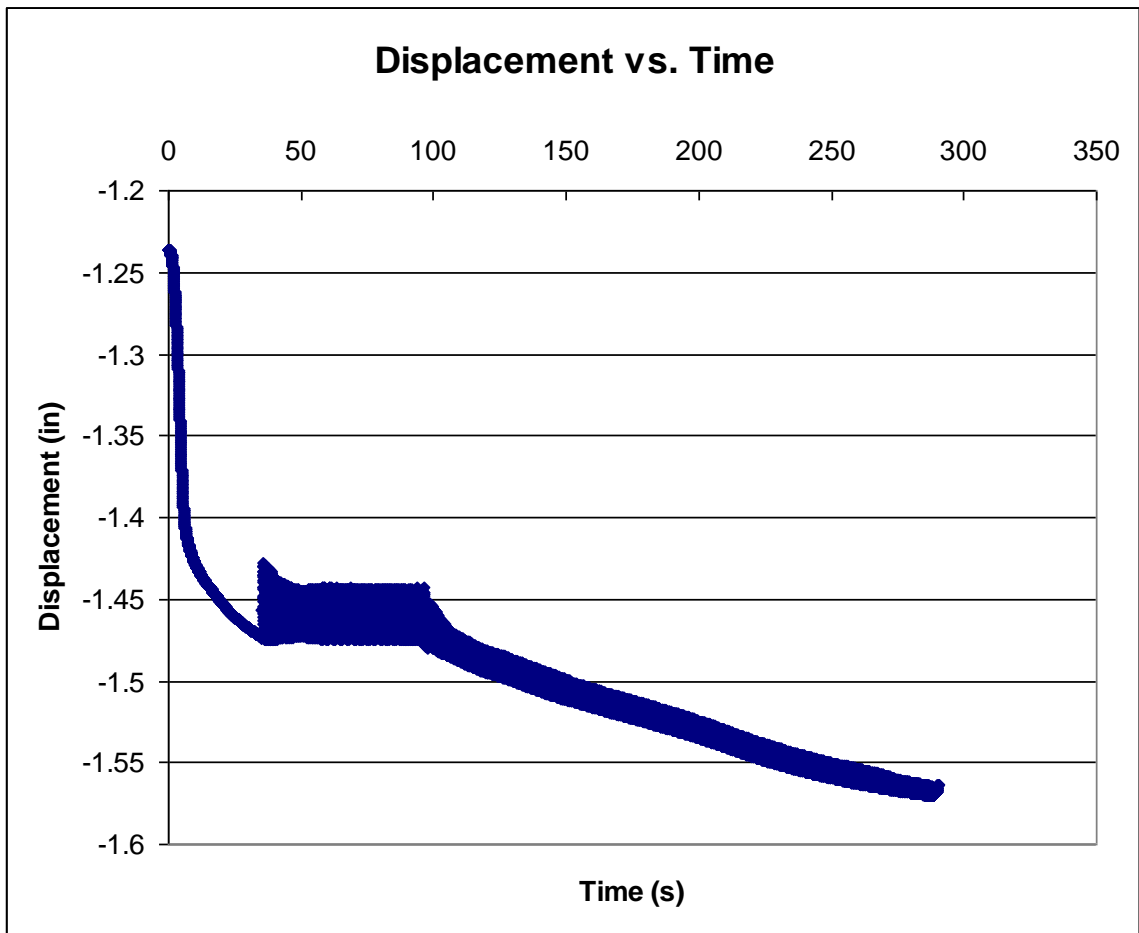


Figure 73 - Graph showing how the displacement varied as a function of time for the -600lbf at 6.0Hz experiment.

The results obtained for this experiment could not be quantitatively compared with any other result obtained so far because its temperature field had changed. Thus, to be able to quantify what these results represented, two more

samples were cast: the first one was solidified under a constant pressure of 600lbf and the second without any pressure. Figure 74 shows a graph where the samples -600lbf at 6.0Hz and -600lbf with constant pressure are compared, together with the no pressure case, Figure 75 shows how the standard deviation varied as a function of position and Figure 76 shows a graph of  $\lambda_2$  values as a function of  $V_L$  for this same set of experiments.

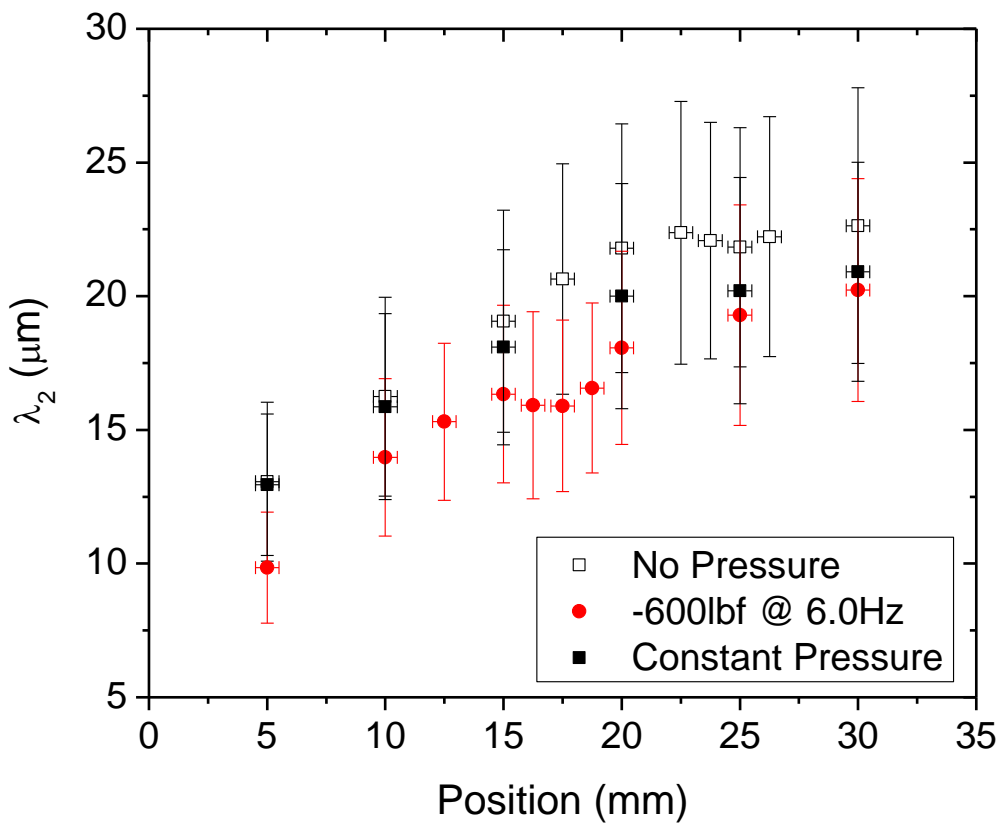


Figure 74 - Graph showing the variation of  $\lambda_2$  as a function of position for the samples without pressure; -600lbf at 6.0Hz and -600lbf at constant pressure. Notice the *dip* around the 17.5mm position for the cyclic pressure curve.

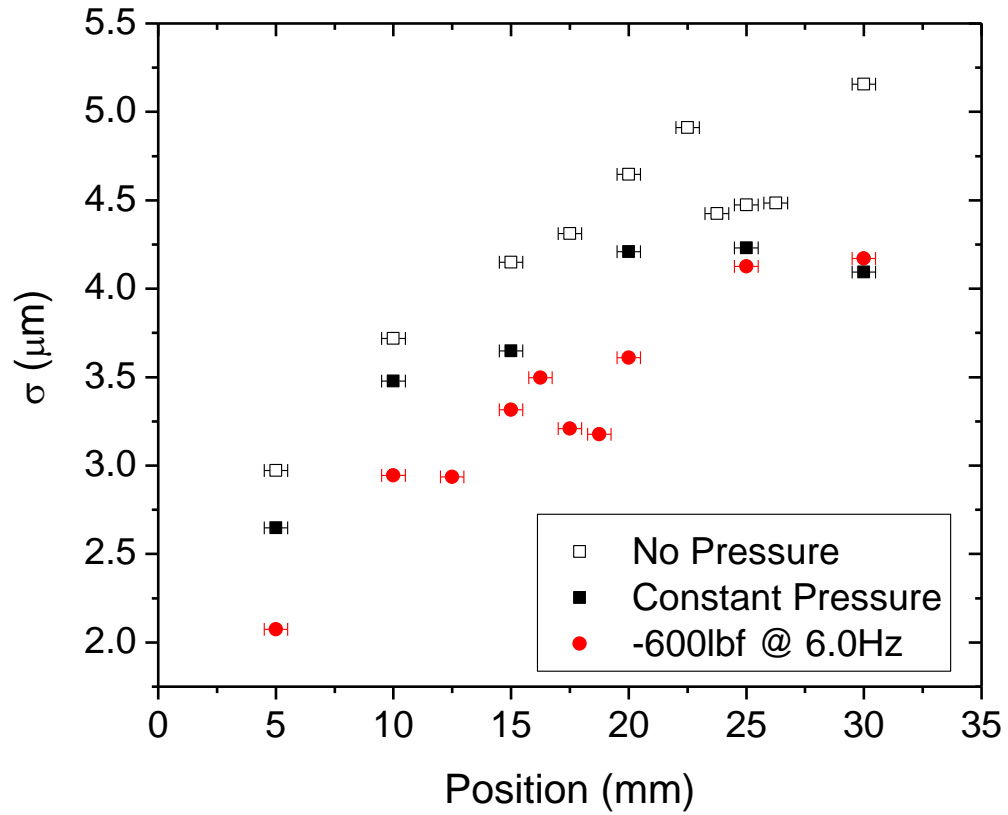


Figure 75 - Graph showing the variation of  $\sigma$  as a function of position for the samples without pressure; -600lbf at 6.0Hz and -600lbf at constant pressure. The same *dip* around the 17.5mm position appears again for the cyclic pressure curve.

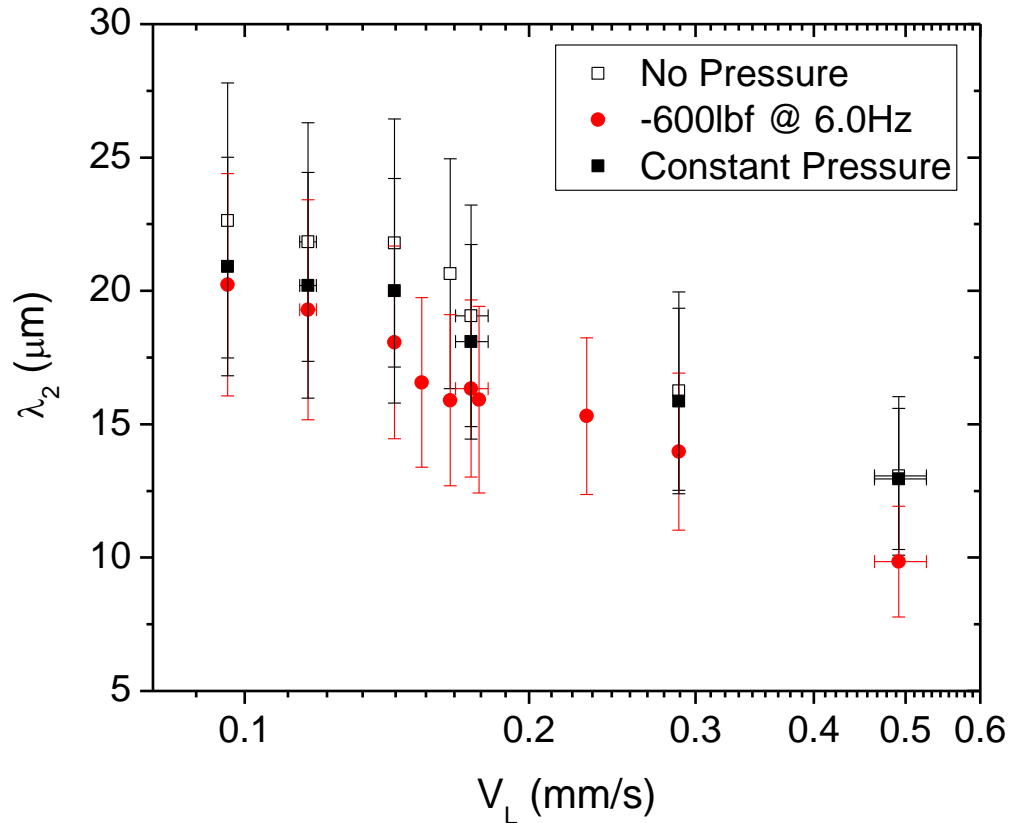


Figure 76 - Graph showing the variation of  $\lambda_2$  as a function of  $V_L$  for the samples without pressure; -600lbf at 6.0Hz and -600lbf at constant pressure. The values for  $V_L$  were extrapolated for the positions 10, 12.5, 16.25, 17.5, 18.75, 20 and 30mm position, since there was no time data for those positions (notice that no horizontal error bars are plotted for these).

As seen in Figure 74, again, the application of pressure did generally decrease  $\lambda_2$  values when comparing the same positions for the samples with and without cyclic pressure. Also, excepting the 05 and 10mm positions, the constant pressure sample had  $\lambda_2$  values located between the no pressure and cyclic

pressure ones. Figure 76 shows that the values of  $\lambda_2$  also decreased as  $V_L$  values increased for this set of experiments.

The most interesting result obtained from this analysis occurred near the 17.5mm position of the sample with cyclic pressurization. In this case, the higher pressures appear to have produced a clearer, localized drop in  $\lambda_2$  between the 15 and 20mm positions. This localized effect is consistent with the predicted resonance behavior, and was the first evidence that the cyclic pressure did finally cause an impact on the material's microstructure. The interpretation of the data is that at early stages of the solidification (positions closer to zero), the side arm frequency formation is very high; therefore the applied forcing (pressure) frequency is not fast enough to cause an impact. As the solidification front approaches the 15-20mm region, the frequency of formation of the side arms starts to get close to the value of the applied pressurization frequency (6.0Hz), which, due to the Clapeyron effect, causes a resonance to the system yielding to the change in arm spacing relative to the case(s) with no oscillating pressure. After the solidification front passes this region where the natural formation frequency matches the experiment frequency, the system goes back to its natural behavior. The standard deviation values also seem to be affected by the pressure pulses (Figure 75). At the same range of positions just mentioned above,  $\sigma$  values decrease when compared to the no pressure and constant pressure samples.

Although this data is very promising, more experiments would need to be done in order to verify its reliability. This is also mentioned at the future work section of this thesis.

The resonance behavior mentioned above, in fact, was the driving force of this research and ultimate goal. Figure 77 shows a graph of how  $\lambda_2$  values were expected to vary, as a function of position, when pressure pulses were to be applied during the solidification process.

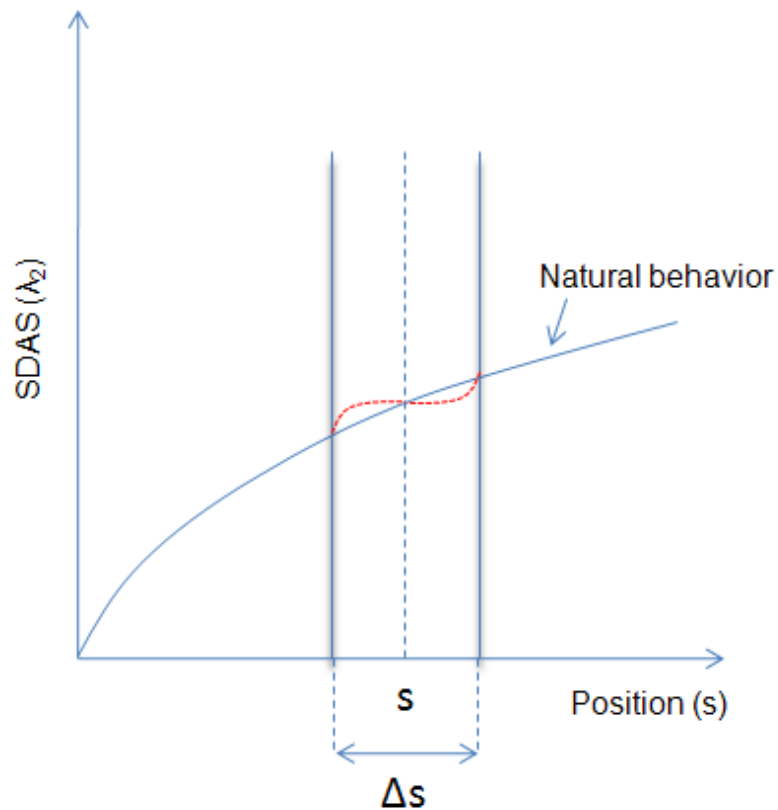


Figure 77 – Graph of  $\lambda_2$  as a function of position showing the expected changes on the values when cyclic pressure is applied during the solidification process. The red curve represents the expected values.

For positions where the applied frequency does not match the formation frequency, i.e. positions close to the chill plate (0mm) and to the top of the liquid/piston surface (30 – 60mm), no change on the natural  $\lambda_2$  values is expected. It is believed though that there is a resonance band ( $\Delta s$ ) - which length is also believed to vary as a function of the amount of applied pressure - around the experiment frequency (position  $s$ ) where the natural frequency of formation of the dendrites should be affected. This band is expected to be around the position ( $s$ ) where the experiment frequency matches the arms natural formation frequency. At that point, there should be no change in the  $\lambda_2$  values, i.e., its value should fall exactly at the natural curve. When looking at values of positions smaller than  $s$  but still inside  $\Delta s$ , the natural frequency of formation of the dendrites is higher than the applied frequency, therefore the applied pressure pulses force the  $\lambda_2$  values to be greater than the natural values (once they are now being formed at a lower frequency, thus slower rate, as a result greater arms). In the other hand, the arms that are at the other side of  $s$  are being naturally formed at a lower frequency than the applied one. Thus when under the influence of pressure pulses, that region will have  $\lambda_2$  values smaller than the ones that would have been formed at a natural pace. The standard deviation ( $\text{stdv} - \sigma$ ) is also expected to decrease for those positions within the  $\Delta s$  band and the amount of decrement should vary as the graph on Figure 78 shows. As the formation frequency gets close to the experiment frequency, the resonance effect becomes greater; therefore, the variation or spread on  $\lambda_2$  values should reach a minimum.

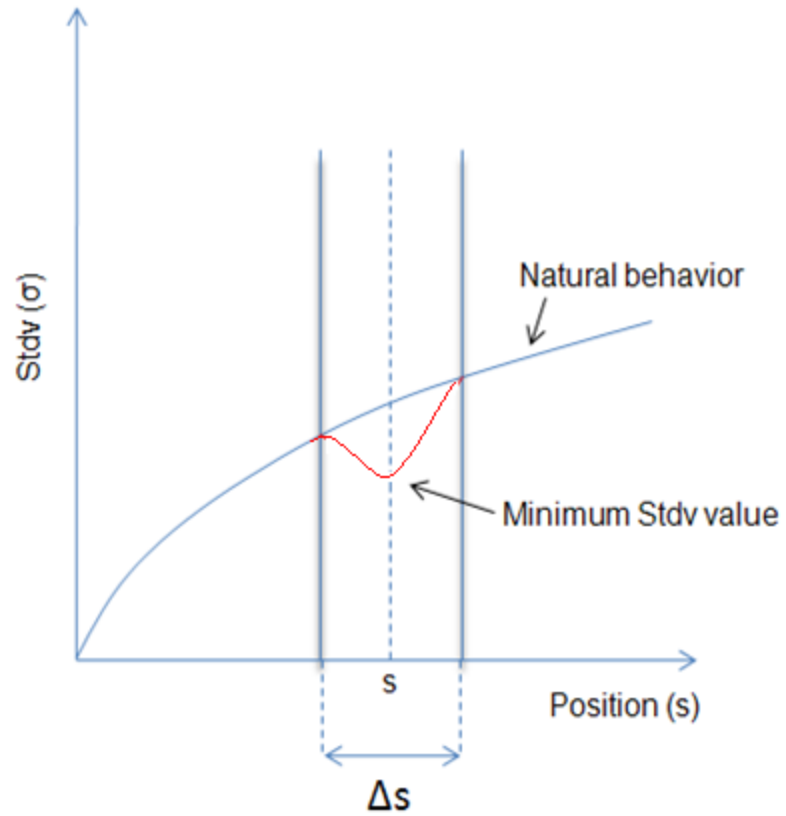


Figure 78 - Graph of standard deviation values ( $\sigma$ ) as a function of position showing the expected changes on the values when cyclic pressure is applied during the solidification process. The red curve represents the expected values.

## 5) CONCLUSIONS

In summary, we draw the following conclusions from the presented work.

- As the liquidus velocity decreases (solidification rate of the liquid/solid interface), the secondary dendrite arms spacing ( $\lambda_2$ ) values increase and their natural frequency of formation increase.
- During a solidification process, a decrease in the  $\lambda_2$  values can be achieved when pressure is applied to the melt (either cyclic or constant).
- Application of cyclic pressure pulses during the solidification process can decrease the  $\lambda_2$  mean and the standard deviation values of the dendrites that form with a natural frequency close to the frequency that the pressure is being applied.
- It is believed that there is resonance band around the applied experiment frequency that causes values of  $\lambda_2$  to increase, when the arms natural formation frequency is smaller than the applied frequency. When the formation frequency is higher than the applied frequency, values of  $\lambda_2$  are expected to decrease.

## 6) FUTURE WORK

This section contains some suggestions on how to further address various aspects of this project including some of its shortcomings. Some suggestions will require changes to the experimental setup. It also includes some approaches to how to continue the investigation into the influence of the pressure pulses on the  $\lambda_2$  values, together with ideas on how to expand the project's scope, adding new tests and experiments that could not be realized during this research period.

In order to improve the apparatus used in the experiments and possibly improve the repeatability and precision of the results, here are some suggestions for future research. It is noted that any improvement in the ease and speed of performing the experiments is greatly needed. At present it takes approximately 1-2 months to prepare and analyze each directional solidification sample. Much of the time is spent in the later metallography steps, but improvements to the consistency of the solidification process would also eliminate the need to repeat the complex experiments in which procedural errors occurred.

- Fabricate a new heater/mold setup where the internal temperature gradient is tunable to be as uniform as possible. This would change the liquidus velocity as a function of position, bringing it closer to theoretical models that assume the whole liquid is at a uniform temperature.

- Better insulate the top part of the mold to minimize the heat extraction that occurs in that direction during the solidification process. This, if correctly done, would allow further analysis of data obtained at positions farther from the chill

plate, which are formed at lower natural frequency, broadening the range of achievable frequencies in the experiments.

- Increase the coolant flow rate. This is expected to increase the experiments' repeatability due to the fact that at low flow rates, the flow is hard to control and not as effective during the initial stages of the solidification process. This change would have to be implemented together with one of the previously mentioned ideas because an increase in the flow rate would increase the liquidus velocity at a given position, increasing its natural formation frequency. This is not generally desired as our mechanical testing system cannot operate at much higher frequencies than are presently being investigated.

- Implement/apply a PID control on the temperature controllers so they can better remain at a constant temperature instead of oscillating. This behavior makes the initial set up of the temperature field a difficult task.

More experiments should be performed in order to verify the influence of the pressure pulses on the  $\lambda_2$  values. Initially, the same parameters and conditions should be used to further verify the reliability of the obtained results. After confirmation, some interesting parameters to be changed would be:

- The applied frequency values. This would, if the hypothesis is correct, shift the position where the  $\lambda_2$  values experience the change in its values. Further setup modifications are required to perform such analysis, as the current design of the experiments is not capable of permitting such drastic changes to the applied frequency.

- Change the magnitude of the pressure applied. Although this would allow the researcher to verify if the resonance band around the natural frequency of side branch formation would, increase as hypothesized. A study of this would require significant changes to the experiment setup, such as redesign of the mold, piston, insulation apparatus and, ultimately, the hydraulic equipment used to pressurize the system.

In case these hypotheses are confirmed, the next step would be to apply this processing technique to other industrial materials such as aluminum alloys, and fully test the final product's mechanical properties. If the results are satisfactory (example: measurable increases in the ultimate tensile strength, etc.) further steps would include the attempt to make the whole process industry-friendly (cost effective), although the pathway to this goal presently appears to be quite challenging and lengthy.

## 7) REFERENCES

- 1) J. Campbell, "Castings". Elsevier Science, Woburn, MA, 1991.
- 2) R. T. DeHoff, "Thermodynamics in Materials Science", McGraw-Hill, New York, NY, 1993.
- 3) W. Kurz, D. J. Fisher, "Fundamentals of Solidification", Brookfield, Aedermannsdorf, Switzerland, 1989.
- 4) W. D. Callister, "Materials Science and Engineering: an Introduction", Wiley, New York, NY, 2000.
- 5) J. W. Rutter, B. Chalmers, "A Prismatic Substructure Formed During Solidification of Metals", Canadian Journal of Physics, 31 (1952) 15-39.
- 6) W. W. Mullins, R. F. Sekerka, "Stability of a Planar Interface During Solidification of a Dilute Binary Alloy", Journal of Applied Physics, 35 (2) (1964) 444-451.
- 7) C. S. Lim, A. J. Clegg, N.L. Loh, "The Reduction of Dendrite Arm Spacing Using a Novel Pressure-Assisted Investment Casting Approach", Journal of Materials Processing Technology 70 (1997) 99-102
- 8) P. R. Goulart, J. E. Spinelli, W. R. Osorio, A. Garcia, "Mechanical Properties as a Function of Microstructure and Solidification Thermal Variables of Al-Si Castings", Materials Science and Engineering A, 421 (2006) 245-253.
- 9) G. A. Santos, C. M. Neto, W. R. Osorio, A. Garcia, "Design of Mechanical Properties of a Zn27Al alloy Based on Microstructure Dendritic Array Spacing", Materials and Design, 28 (2007) 2425-2430.

- 10) Y. S. Han, D. H. Kim, H. I. Lee, Y. G. Kim, "Effect of Applied Pressure During Solidification on The Microstructure Refinement in an Al-Cu Alloy", *Scripta Metallurgica et Materialia*, 31 (12) (1994) 1623-1628.
- 11) A. Yu, S. Wang, N. Li, H. Hu, "Pressurized Solidification of Magnesium Alloy AM50A", *Journal of Materials Processing Technology* 191 (2007) 247-250.
- 12) Ph. Bouissou, B. Perrin, P. Tabeling, "Influence of an External Flow on Dendritic Crystal Growth", *Physical Review A*, 40 (1) (1989) 509-512.
- 13) Ph. Bouissou, A. Chiffaudel, B. Perrin, P. Tabeling, "Dendritic Side-Branching Forced by an External Flow", *Europhysics Letters*, 13 (1) (1990) 89-94.
- 14) X. W. Qian, H. Z. Cummins, "Dendritic Sidebranching Initiation by a Localized Heat Pulse", *Physical Review Letters*, 64 (25) (1990) 3038-3041.
- 15) R. Mahmudi, A. R. Geranmayeh, A. Rezaee-Bazzaz, "Impression creep behavior of cast Pb-Sb alloys", *Journal of Alloys and Compounds*, 427 (2007) 124-129
- 16) D. M. Rosa, J. E. Spinelli, I. L. Ferreira, A. Garcia, "Cellular/Dendritic Transition and Microstructure Evolution During Transient Directional Solidification of Pb-Sb Alloys", *Metallurgical and Materials Transactions A*, 39 (9) (2008) 2161-2174.
- 17) [www.nasa.gov](http://www.nasa.gov)
- 18) ASM Handbook, "Alloy Phase Diagrams", Volume 3, ASM International (1992)

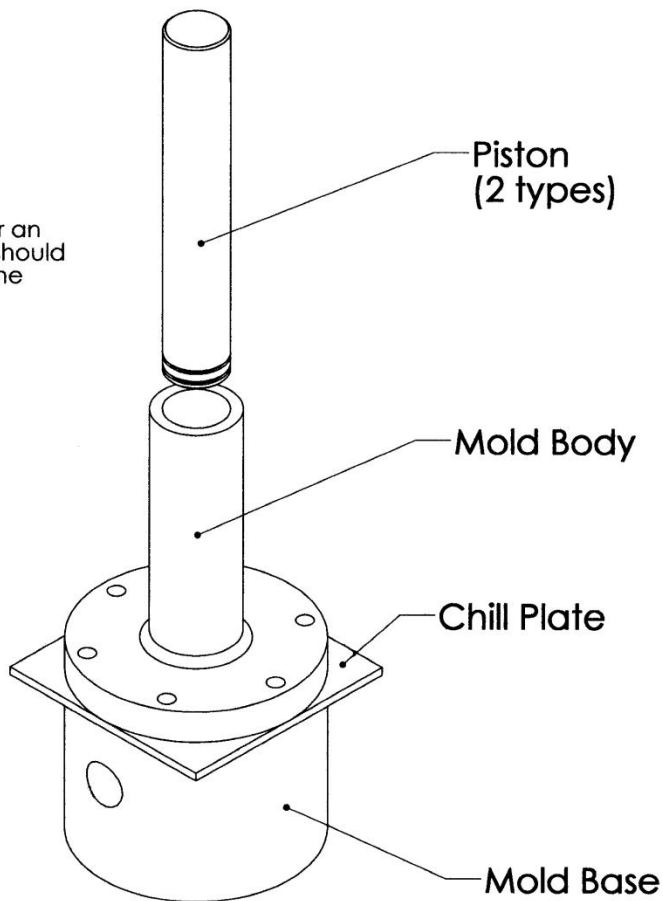
- 19) J. C. LaCombe, "Solidification and Crystal Growth Class", 2009. Lecture 08.
- 20) ASM Handbook, "Casting", Volume 15, ASM International (1998)
- 21) N. H. March, M. P. Tosi, "Introduction to liquid state physics", World Scientific, River Edge, NJ (2002)
- 22) D. R. Lide, "Handbook of Chemistry and Physics", 72<sup>nd</sup> Edition, CRC Press, Boston, MA (1992)
- 23) [www.webelements.com](http://www.webelements.com)
- 24) S. S. Nibhanupudi, "Affect of Pressurized Solidification on The Secondary Dendritic Arm Spacing in Lead-Tin Alloy", Master of Science Thesis, University of Reno, NV (2008).

### 8) APPENDIX

#### Appendix A

Please see the provided piston/cylinder (with ring) for an example of how the piston should fit into the mold body with the piston rings in place.

Material: Stainless Steel throughout



**SolidWorks Student License**  
**Academic Use Only**

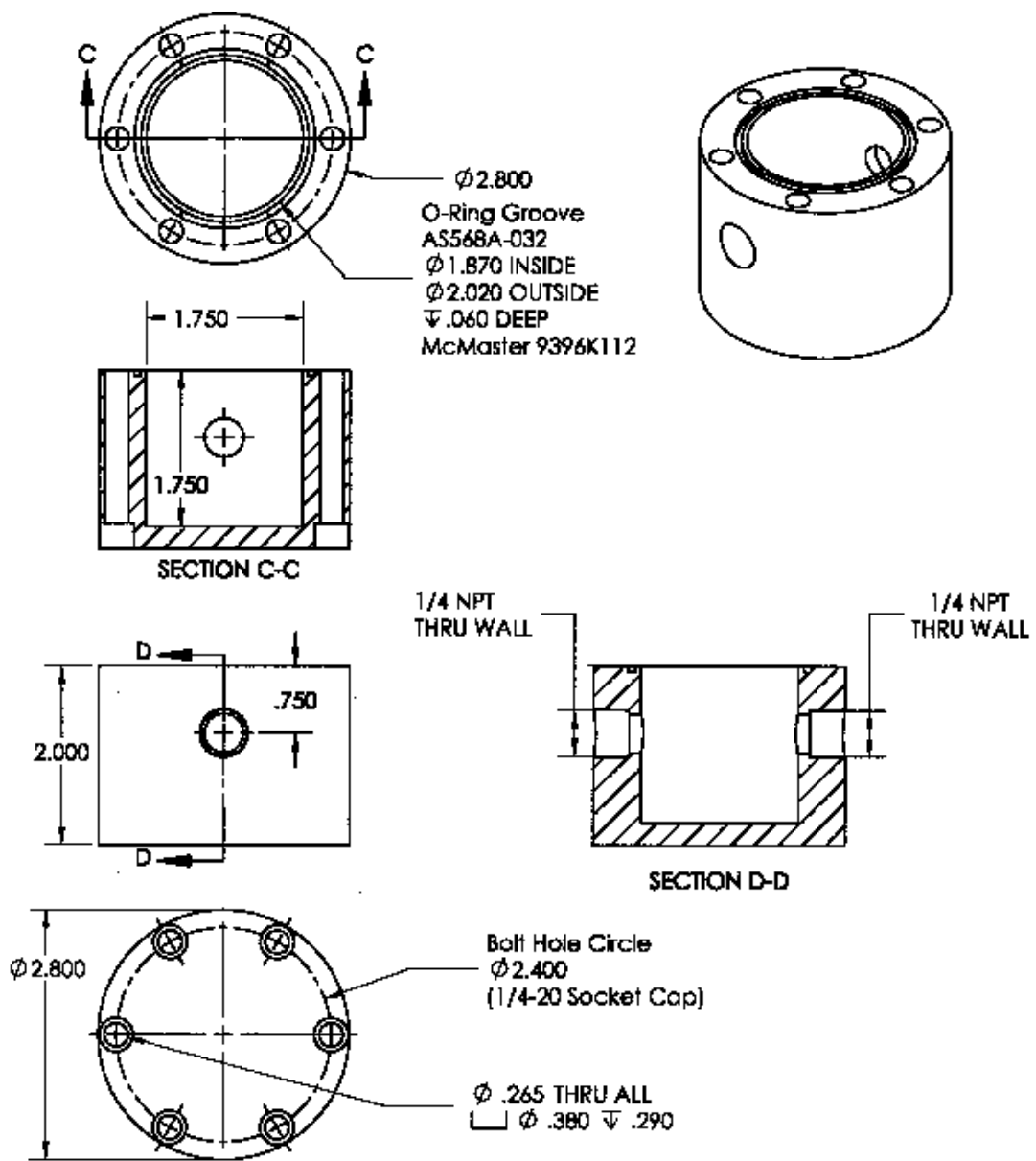
DIMENSIONS ARE IN INCHES  
 TOLERANCES:  
 FRACTIONAL ±  
 ANGULAR: MACH ± BEND ±  
 TWO PLACE DECIMAL ±  
 THREE PLACE DECIMAL ±

DRAWN	NAME	DATE
CHECKED		
ENG APPR.		
MFG APPR.		
G.A.		
COMMENTS:		

REPRODUCTION BY ANY MEANS OR FOR ANY PURPOSE WITHOUT THE WRITTEN PERMISSION OF THE AUTHOR IS PROHIBITED.  
 NEXT ASSY USED ON FINISH APPLICATION DO NOT SCALE DRAWING

SIZE DWG. NO. REV  
 Piston Mold Assembly (Rev 5).SLDPR





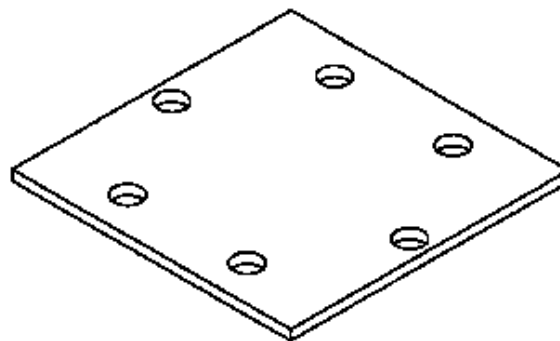
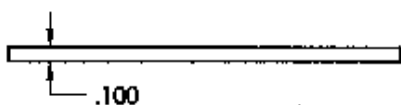
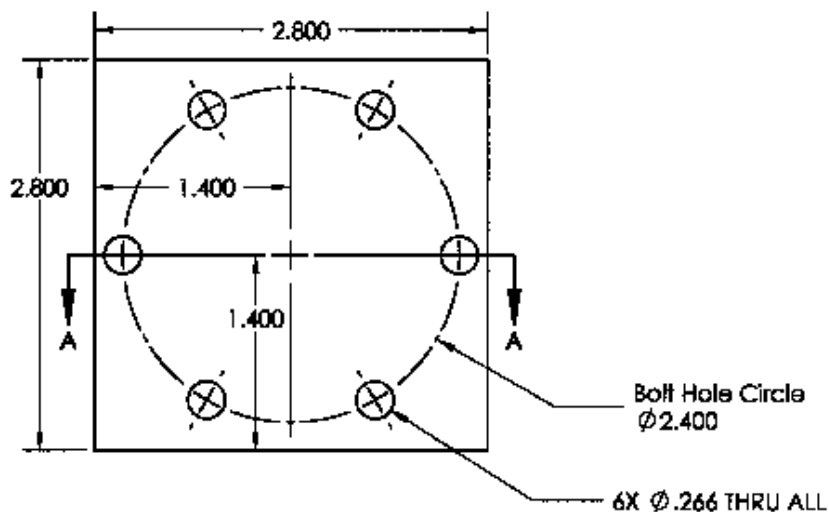
DIMENSIONS ARE IN INCHES  
 TOLERANCES  
 FRACTIONAL ± .005  
 ANGULAR IN/100 ± .010  
 THREE PLACE DECIMAL ± .001  
 THREE PLACE DECIMAL ± .001

DRAWN  
 CHECKED  
 ENG APPR.  
 MFG APPR.  
 QA  
 EXAMINED

**SolidWorks Student License**  
**Academic Use Only**  
 NOT BE LOANED, REPRODUCED, COPIED, OR REPRODUCED  
 WITHOUT THE WRITTEN PERMISSION OF  
 DASSAULT SYSTEMES CORPORATION

PISTON MOLD BASE (REV 5)  
 9396K112

APPLICATIONS DO NOT SCALE DRAWING



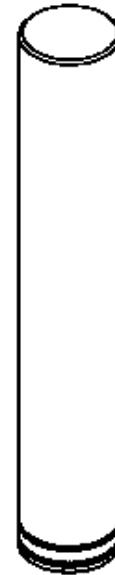
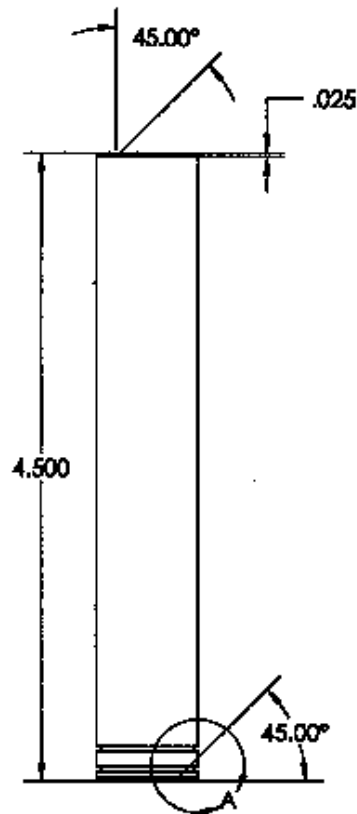
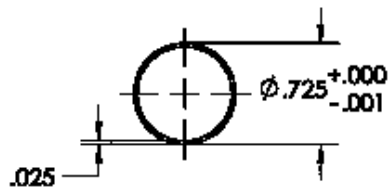
DIMENSIONS ARE IN INCHES  
 TOLERANCES:  
 FRACTIONALS: ± .005  
 ANGULAR: MINUS .005  
 TWO PLACE DECIMAL: ± .005  
 THREE PLACE DECIMAL: ± .001

NAME	DATE
DRAWN	
CHECKED	
ENG APPR.	
MFG APPR.	
QA	
COMMENTS	

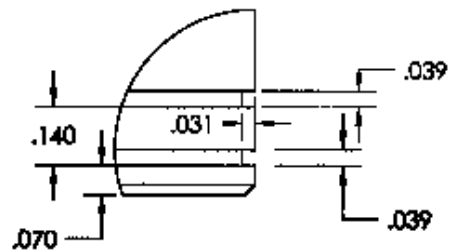
**SolidWorks Student License**  
**Academic Use Only**  
 NOT FOR SALE OR DISTRIBUTION  
 WITHOUT THE WRITTEN PERMISSION OF  
 DASSAULT SYSTEMES  
 PROHIBITED.

APPLICATION DO NOT SCALE DRAWING

Parton Mold Chill Plate (Rev 5)  
 10/11/11 10/11/11 10/11/11



DETAIL A  
PISTON RING GROOVES  
SCALE 3 : 1



**SolidWorks Student License**  
**Academic Use Only**

NO RESALE, RENTAL, REPRODUCTION, OR DISTRIBUTION WITHOUT THE WRITTEN PERMISSION OF  
©2007 DASSAULT SYSTEMES  
PROHIBITED.

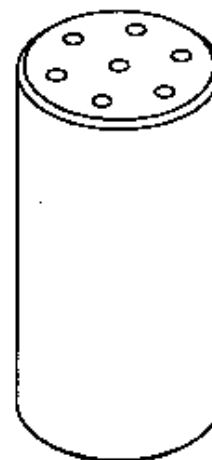
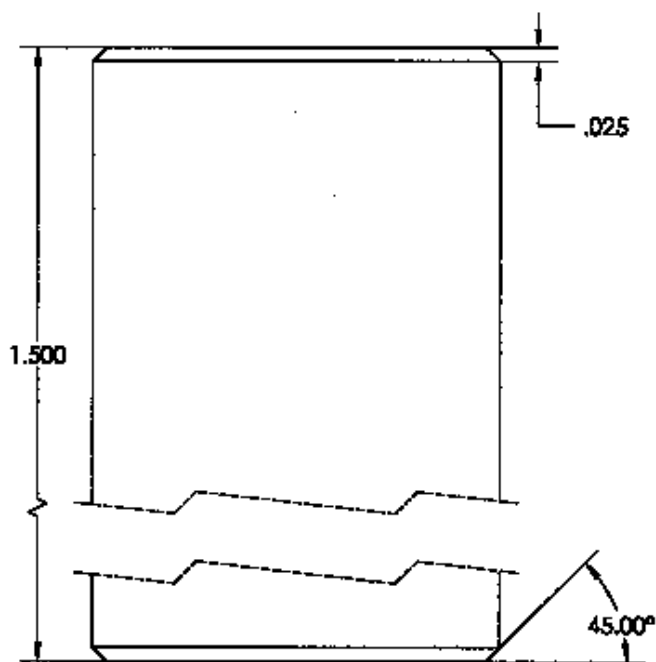
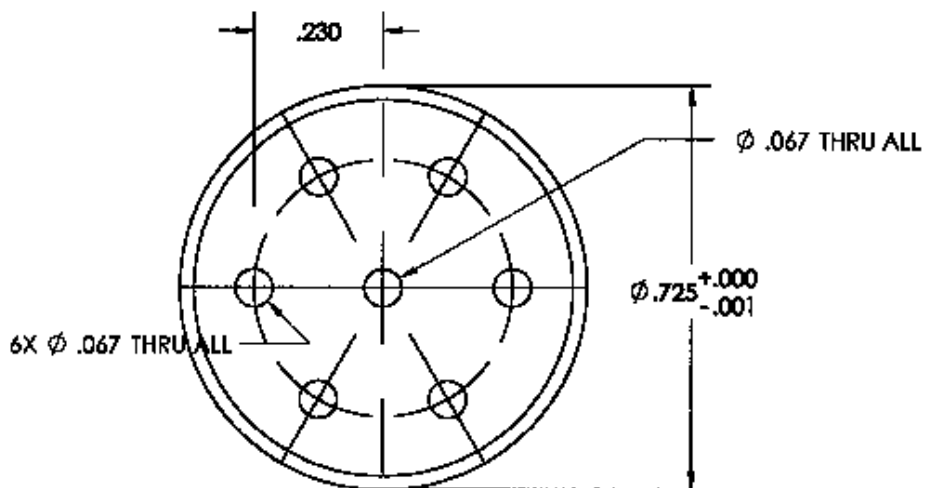
DIMENSIONS ARE IN INCHES  
TOLERANCES:  
FRACTIONAL 1/16  
ANGULAR DIMENSIONS MINUS 1  
TWO PLACE DECIMAL .02  
THREE PLACE DECIMAL .003

DATE DATE

DESIGNER  
CHECKED  
MANUFACTURER  
MFG APPROV.  
D.A.  
EXAMINER

NO COPY USED ON PART  
APPLICATION DO NOT SCALE DRAWING

NO DWG. NO. A Piston (Rev 5) REV.  
SCALE:1 PAGES: 1 SHEET 1 OF 1



DIMENSIONS ARE IN INCHES  
 TOLERANCES:  
 FRACTIONALS  
 ANGULAR INCHES BOND #  
 THIRD PLACE DECIMAL 2  
 SECOND PLACE DECIMAL 2

DRAWN  
 CHECKED  
 ENG APPR.  
 MFG APPR.  
 C.A.  
 COMMENTS

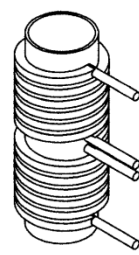
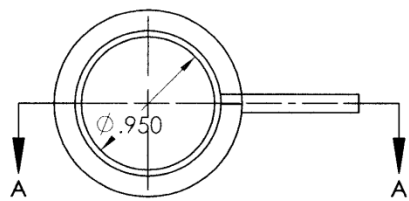
NAME  
 DATE

**SolidWorks Student License**  
**Academic Use Only**

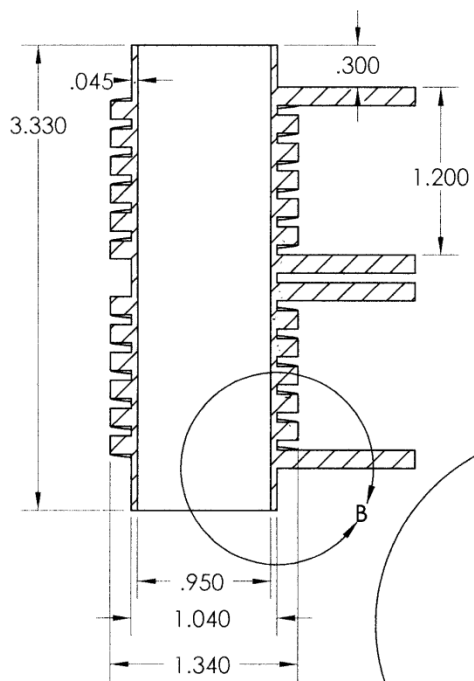
NOT TO BE USED ON  
 APPLICATION

DO NOT SCALE DRAWING

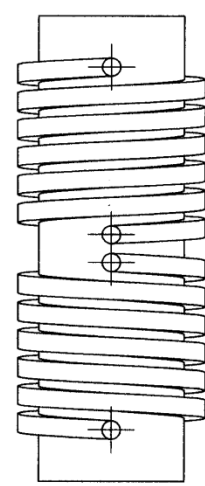
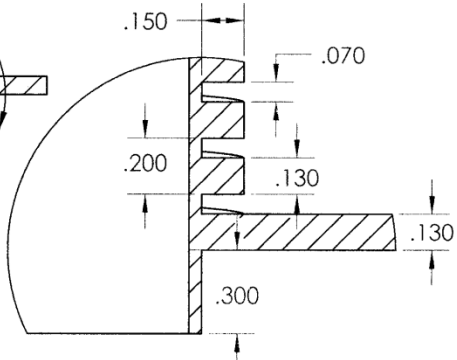
Parton (zero pressure) (Rev 5)  
 SCALE: 1:1



SECTION A-A



DETAIL B  
SCALE 2 : 1



DIMENSIONS ARE IN INCHES  
 TOLERANCES:  
 FRACTIONAL ±  
 ANGULAR: MACH ± BEND ±  
 TWO PLACE DECIMAL ±  
 THREE PLACE DECIMAL ±

NAME DATE

DRAWN  
 CHECKED  
 ENG APPR.  
 MFG APPR.  
 Q.A.  
 COMMENTS:

**SolidWorks Student License**  
**Academic Use Only**

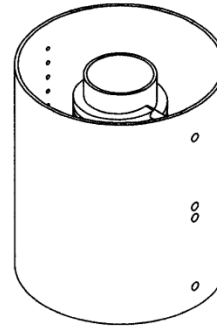
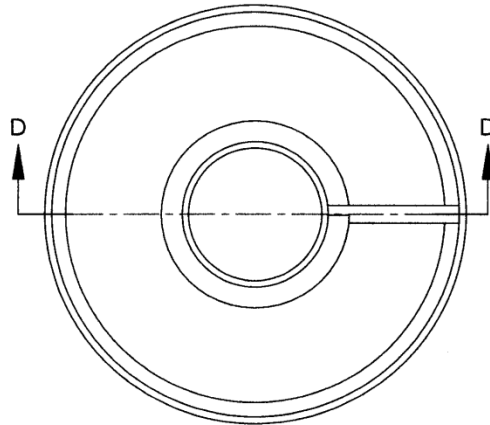
REPRODUCTION OF THIS DRAWING FOR ANY PURPOSE WITHOUT THE WRITTEN PERMISSION OF CADSWORKS CORPORATION IS PROHIBITED.

NEXT ASSY. USED ON FINISH MATERIAL

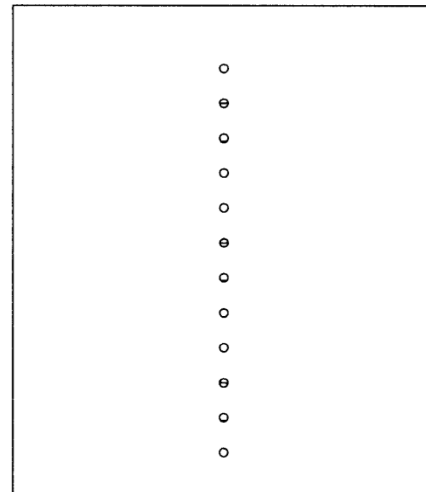
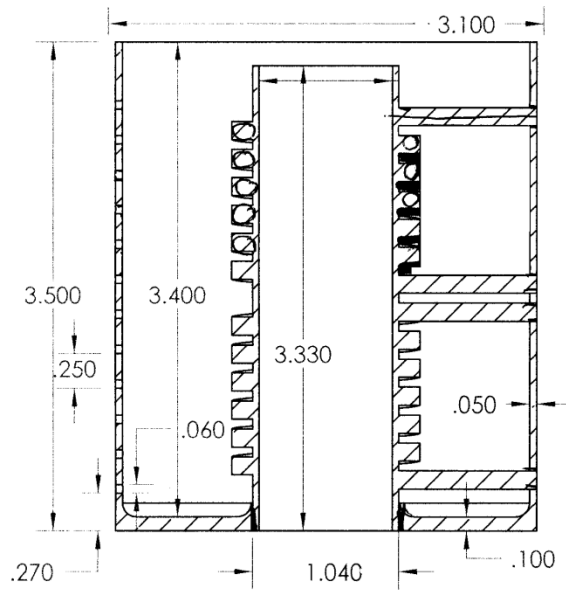
APPLICATION DO NOT SCALE DRAWING

SIZE DWG. NO. REV.  
**Piston Mold Heater Plug (Rev 5b)**

SCALE:1:1 WEIGHT: SHEET 1 OF 1



SECTION D-D  
SCALE 1 : 1



DIMENSIONS ARE IN INCHES  
TOLERANCES:  
FRACTIONAL ±  
ANGULAR: MACH ± BEND ±  
TWO PLACE DECIMAL ±  
THREE PLACE DECIMAL ±

NAME DATE

DRAWN  
CHECKED  
ENG APPR.  
MFG APPR.  
Q.A.  
COMMENTS:

**SolidWorks Student License**  
**Academic Use Only**

REPRODUCTION OF THIS DOCUMENT IS PROHIBITED WITHOUT THE WRITTEN PERMISSION OF  
<INSERT COMPANY NAME HERE> IS PROHIBITED.

APPLICATION

FINISH  
DO NOT SCALE DRAWING

SIZE DWG. NO. REV.  
**AHeater Assembly (Rev 5)**  
SCALE:1:2 WEIGHT: SHEET 1 OF 1

## Appendix B

As already mentioned, a MTS machine was used in order to apply pressure on the molten metal during the solidification process. Two different types of pressure assisted experiments were realized: with cyclic pressure and with constant pressure. The signal controlling was performed using a program contained in the MTS machine software package called Multi Purpose Testware (MPT). The basic command structure for either test was the same, since the software allows the user to disable an undesired command at any time before the program execution. The commands used inside the MTP software for the constant pressure experiments were the followings:

- Ramp up – This command tells the hydraulic system to increase the load up to a certain point at a certain rate;
- Stay – After reaching the desired force (or displacement), this command would keep the machine head at that position for a certain period of time.

The commands used for the cyclic experiments were:

- Ramp up – The same as for the constant pressure;
- Cyclic – Applies a cyclic motion to the hydraulic system. A variety of motions could be applied although, for this research, only the square one was used. It allows the operator to set the range of motion of the head either by displacement or by load as well as the frequency desired. The load control was the one used.

Both programs had a “limits” feature that would stop the experiment in case any of the previously set limits was reached. The MPT software also allows the

user to acquire data for both displacement and load at a certain frequency and this was also used during the experiments. But before any experiment could be realized, the machine had to be tuned accordingly to the material to be used as sample. This was achieved by changing the Proportional-Integral-Derivative (PID) controller values, which could be found inside the tuning sub-menu. For example, for a piece of foam, which has extremely high pressure-deformation ratio, the PID values were completely different than the ones used for the molten metal, which is *incompressible*.

### **Appendix C**

In order to verify the accuracy and reliability of the Scentis software dendrite arms spacing measurement feature, a manual measurement of the secondary arm spaces was realized in one of the micrographs.

The manual measurement process was executed as following.

First, a microscope image of the area of interest, together with a previously calibrated scale bar, was taken. The scale bar calibration was realized according to the lens magnification and using the aid of a calibration standard (Figure 1). After printing out the image, its scale bar was measured using a simple rule in order to convert the micrometer scale to a centimeter one, useful on the printed picture. That step led to an equivalent value of approximately 34.2 $\mu\text{m}$  for each centimeter on the image.

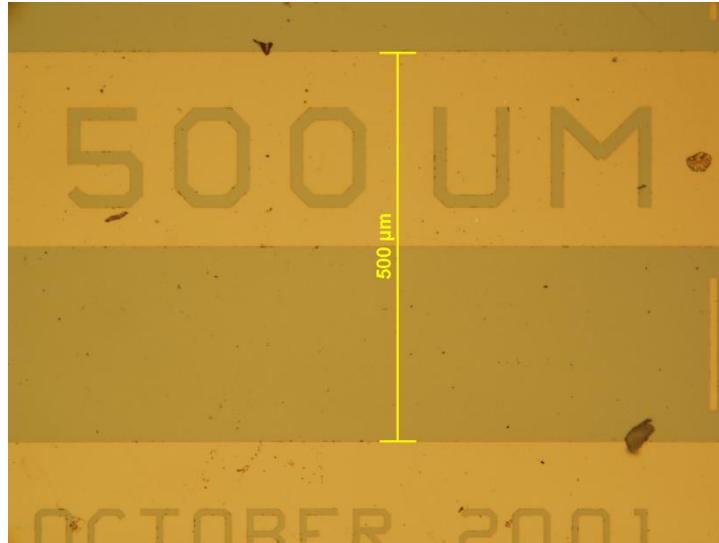


Figure 1 – Calibration standard at a magnification of 20x.

The next step was to manually draw a straight line over the dendrite secondary arms and measure each single distance between each arms couple (Figure 2). These values were reported on a Microsoft Excel spreadsheet. The values in centimeter were converted to micrometer and, still with the aid of the Excel, the average of those values were obtained as were their standard deviation as well. This whole process was repeated for a second line. Now, once all the needed values were obtained, a comparison of them using the Scentis software can be realized.

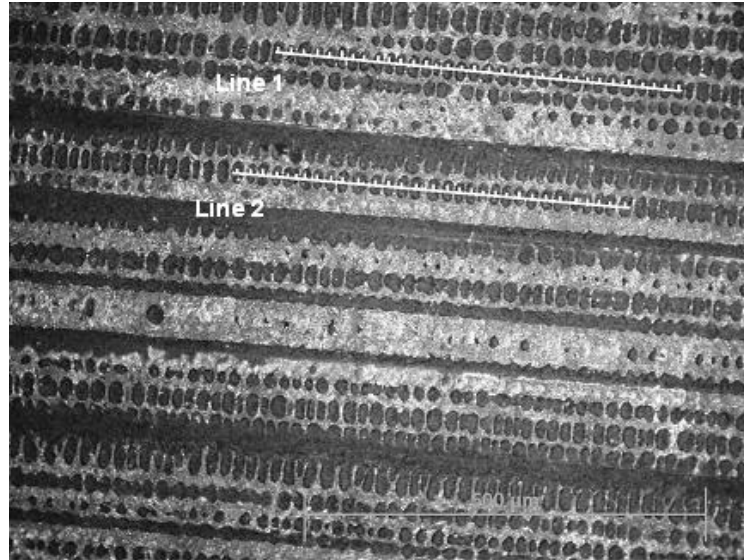


Figure 2 – Image of the drawn lines, including the arms centers marks, used to obtain the secondary arm spacing measurements manually.

In order to obtain a reliable and trustable comparison, was made sure that the spaces measurements were obtained as usual, meaning by that, all the lines and reference marks were still obtained and edited as if a regular measurement proceeding was being conducted. The same exact dendrites that were measured on the printed image were then measured with the Scentis software and those values were exported to the same previously mentioned Excel spreadsheet. As can be seen on the Table 1, the values obtained manually agreed reasonably well with the values obtained using the Scentis Software, having an average difference of  $0.9 - 1.2\mu\text{m}$ , which is extremely acceptable once possible errors and approximations caused by the human eye and judgment can easily happen when measuring the dendrites spaces manually. Also, some of those minor variations could be related with some small dislocations on the dendrites arms

central line caused by the software when assigning those spots (A spots), which are the reference for these measurements.

Thus, after realizing this analysis, it could be concluded that the software Scentis is a reasonable, accurate and useful tool for secondary arms spacing measurements.

Table 1 – DAS measurements, both manually and with Scentis, together with theirs mean and standard deviation.

Line 1				Line 2				
Dendrite arms space				Dendrite arms space				
cm	um	um (Scentis)	Difference	cm	um	um (Scentis)	Difference	
0.45	15.39	14.62	0.77		0.5	17.1	15.63	1.47
0.5	17.1	18	0.9		0.39	13.34	14.27	0.93
0.5	17.1	14.95	2.15		0.54	18.47	16.99	1.48
0.48	16.42	15.63	0.79		0.39	13.34	14.95	1.61
0.4	13.68	12.91	0.77		0.22	7.52	8.35	0.83
0.42	14.36	15.63	1.27		0.41	14.02	12.71	1.31
0.4	13.68	14.72	1.04		0.43	14.71	15.63	0.92
0.5	17.1	16.72	0.39		0.47	16.07	14.95	1.12
0.41	14.02	14.09	0.07		0.49	16.76	16.31	0.45
0.4	13.68	14.95	1.27		0.56	19.15	20.34	1.19
0.45	15.39	16.31	0.92		0.65	22.23	21.12	1.12
0.45	15.39	14.95	0.44		0.5	17.1	15.63	1.47
0.35	11.97	13.7	1.73		0.49	16.76	16.99	0.23
0.38	13	13.48	0.49		0.45	15.39	16.31	0.92
0.52	17.78	15.63	2.15		0.65	22.23	23.11	0.88
0.5	17.1	16.99	0.11		0.5	17.1	16.99	0.11
0.5	17.1	17.67	0.57		0.45	15.39	14.95	0.44
0.53	18.13	18.35	0.22		0.4	13.68	14.27	0.59
0.5	17.1	14.95	2.15		0.45	15.39	14.95	0.44
0.48	16.42	16.99	0.57		0.45	15.39	14.95	0.44
0.53	18.13	16.99	1.14		0.45	15.39	14.27	1.12
0.6	20.52	22.25	1.73		0.46	15.73	16.31	0.58
0.69	23.6	20.57	3.03		0.48	16.42	16.31	0.11
0.4	13.68	15.63	1.95		0.5	17.1	17.67	0.57
0.45	15.39	12.91	2.48		0.48	16.42	18.79	2.37
0.49	16.76	16.92	0.17		0.63	21.55	18.59	2.95
0.57	19.49	21.13	1.64		0.4	13.68	12.91	0.77
0.5	17.1	14.95	2.15		0.46	15.73	14.95	0.78
0.43	14.71	14.27	0.43		0.4	13.68	14.27	0.59
0.4	13.68	15.63	1.95		0.55	18.81	19.26	0.45
0.48	16.42	16.31	0.11					

Line 1		
Manually	Scentis	Difference
16.174	16.090	1.147
Standard Deviation		
Manually	Scentis	Difference
2.403	2.236	0.815

Line 2		
Manually	Scentis	Difference
16.188	16.091	0.941
Standard Deviation		
Manually	Scentis	Difference
2.921	2.782	0.626

All measurements		
Manually	Scentis	Difference
16.181	16.091	1.046
Standard Deviation		
Manually	Scentis	Difference
2.647663	2.498054	0.729796